HIGH-PRECISION MEASUREMENTS IN ATOMIC CESIUM SUPPORTING A LOW-ENERGY TEST OF THE STANDARD MODEL

by

STEPHEN CARROLL BENNETT

B. A., Middlebury College, 1992

M. S., University of Colorado, 1995

A thesis submitted to the

Faculty of the Graduate School of the

University of Colorado in partial fulfillment

of the requirements for the degree of

Doctor of Philosophy

Department of Physics

1998

This thesis entitled:
High-Precision Measurements in Atomic Cesium Supporting a Low-Energy Test of the Standard Model
written by Stephen Carroll Bennett
has been approved for the Department of Physics
by

Carl E. Wieman

Eric A. Cornell

Date

The final copy of this thesis has been examined by the signatories, and we find that both the content and the form meet acceptable presentation standards of scholarly work in the above mentioned discipline.

Bennett, Stephen Carroll (Ph. D., Physics)

High-Precision Measurements in Atomic Cesium Supporting a Low-Energy Test of the Standard Model

Thesis directed by Professor Carl E. Wieman

The measurement of parity nonconservation (PNC) in atomic cesium provides the most precise low-energy test of the standard model of electroweak interactions. However, the test is limited by the uncertainty in the *ab initio* calculations that are required to interpret the measurement. This thesis describes one measurement that suggests that the accuracy of the theory may be better than its authors claim, and a second measurement that may be used in place of a less accurate calculation.

A 0.11% measurement of the dc Stark shift of the $6S \rightarrow 7S$ transition in cesium using high-precision laser spectroscopy removes the largest discrepancy between experiment and theory. With this new measurement, and several recently improved measurements by other groups, the uncertainty of the theory is re-evaluated. We find that the standard deviation of the differences between experiment and theory is 0.40%. This standard deviation suggests that the quoted uncertainty of the theory can be reduced from 1% to 0.40%.

A 0.16% measurement of $M_{\rm hf}/\beta$ using similar methods is also presented. The quantity $M_{\rm hf}$ is the off-diagonal hyperfine-interaction-induced magnetic dipole amplitude, and β is the tensor transition polarizability; both are for the $6S \rightarrow 7S$ transition in cesium. This ratio is combined with a 0.25% semi-empirical determination of $M_{\rm hf}$ from another group to determine the value of β with a precision of 0.30%. Previously, the value of β used in the test of the standard model was calculated using the *ab initio* theory, thus increasing the uncertainty due to theory in the final test. Using the new measured value of β, the current values of the theory with improved precision, and the previous measurement of PNC in cesium we make a 0.61% test of the standard model.

The precision of this test is likely to motivate further work in this field. Therefore, two experiments are discussed that may be useful in improving the signal-to-noise ratio on a future PNC measurement: an experiment that phase modulates the dye laser used to drive the $6S \rightarrow 7S$ transition to eliminate the spatial intensity variation inside a Fabry-Perot etalon, and an experiment that transversely cools the atomic cesium beam. Finally, a different–but related–PNC measurement is discussed.

For Rebecca.

ACKNOWLEDGEMENTS

This document has but a single author; every other document upon which my name has been placed has at least two, and usually more. The simple fact of the matter is that in all of these works, the number of people who contributed is far larger than the author list would suggest. I could not have produced this thesis without the help of a very long list of people both inside JILA and out, where they helped me along my professional and personal journeys. The list is, of course, too long to remember to thank everyone, but here is where I shall try.

First and foremost I must thank my advisor Dr. Carl Wieman. Somehow Carl saw something in me worth growing when I was a first-year graduate student. Although he was uncertain, at times, whether I **would** finish graduate school with a Ph. D., he never doubted that I **could**. He has taught me a great deal about high-precision experiments and how to do them right. I probably taught him a thousand ways he never dreamed about to do them wrong. I am a much better scientist because of his tutelage, and for that he has my gratitude.

There are two colleagues who worked with me daily until they went their separate ways: Jake Roberts and Chris Wood. Chris, being the senior graduate student, taught me lots about the ins and outs of the experimental details. Jake, despite being the "junior" graduate student, was an excellent source of ideas, and was always a valuable resource for when I did not completely understand the theory, or when I needed someone to figure out how to analyze the data I just took while I slaved away taking more. Thanks to you both.

I am convinced that JILA is a such a great place to work because of the support staff.

In no particular order, Hans Greene, Hans Rohner, Blaine Horner, Dave Alchenberger, and Seth Wieman, were always around in the shop to help me build that part I needed yesterday, or to solve what I usually thought was an unsolvable problem. Terry Brown, Paul Buckingham, James Fung-A-Fat, and Mike Whitmore were invaluable for their help with electronics. Whether it was trying to figure out what was wrong with my high-voltage amplifier, or trying to get my favorite oscilloscope fixed, they were always willing to help.

There is a group of people in JILA who some would call "secretaries" or "assistants." I call them saviors. Many, many thanks to Karen Melcher, Fran Haas, Leslie Haas, Lisa Perry, LaReina Romero, Agnes Polanowski, and Susannah Jarvis, who take care of all the details, make the coffee, and make JILA a more pleasant place to live... um, I mean work.

The first time I ordered something from the Supply Office, I think I got on Ed's bad side. I quickly corrected that mistake and stayed on his good side ever since (I think). Everyone should give Ed Holliness a big thanks, because his office makes buying equipment painless, and without him we'd have to buy our own stuff!

I did not find out how valuable the Scientific Reports Office is until I started writing real papers. Many thanks must go to Marilee DeGoede and Laurie Kovalenko for taking care of a lot of the little details I never realized existed.

On a more personal note, I have had many friends who have helped me out along the way. Thanks to Andy Steinbach for studying with me for comps. Thanks to Thomas Crawford for commiserating with me during the bad times. Thanks to Ruth Rhodes for all the trips up to Dairy Queen for Blizzards (and where are you now?). Thanks to Michelle–then Pierce, now Ruprecht–and Pete Ruprecht for all the card playing (do you still owe me a bomber?). Thanks to everyone at the "Physics House" for all our Thanksgivings and Christmases together. Thanks to Matt Wingate for being a great roommate until Rebecca came along. Thanks to Mrs. Sama for making me hate English. Thanks to Rich Wolfson and Jeff Dunham for helpful advice when making big decisions. Thanks to Mom, Dad, and Kristy for being proud.

One friend and colleague deserves special mention: Kristan Corwin. I am not sure how it worked out this way, but Kristan always seemed to be around when I wanted to talk to someone because I was bored, because I had an exciting new result to share, because I had a problem I did not understand, because I needed someone to cheer me up–whatever. My graduate school experience was much more pleasant, and I have a different outlook because of her. Thank you very much, Kristan.

Finally, there are no words to express my gratitude to my dear wife Rebecca. This is the second thesis she has had to live through, and I promise there will not be a third. Rebecca has been with me through thick and thin and has supported my every decision, even when she felt that she did not. It is no understatement to say that without her support I would not still be in physics. Thank you, Rebecca. Now it is your turn.

CONTENTS

CHAPTER

FIGURES

Figure

TABLES

Table

CHAPTER 1

INTRODUCTION

1.1 Search for Understanding

At some very basic level, physicists are driven by the desire to understand the world around them. We perform experiments and invent theories that probe and describe how things work. Good experiments are sometimes described as "beautiful" and simple theories are sometimes called "elegant." It seems as if there is an underlying desire to have nature, its behavior, and descriptions of its behavior be beautiful, elegant, and simple.

When formulating theories one would like things to be symmetric in some way, just like nature. For example, the physics of a particle in motion is the same regardless of whether time is running forward or backward. Indeed, symmetries are so fundamental that the definite relationship between invariance or symmetry properties of a system and its conserved quantities is described in the mathematical Noether's Theorem [1]. So, when a symmetry is broken, physicists take notice.

Such was the case when parity nonconservation (PNC) was first observed in nuclear beta decay by Wu and collaborators [2]. In this experiment, the scientists studied the decay $^{27}\mathrm{Co}^{60} \rightarrow^{28} \mathrm{Ni}^{60} + e + \bar{\nu}$ by measuring the direction of the emitted electrons relative to the magnetic moment of the $^{27}\mathrm{Co}^{60}$ nuclei. They found that the direction of emission was not symmetric with respect to the plane perpendicular to the magnetic moment. Instead, there is a preferred direction of emission that is "left-

handed" with respect to the direction of an imaginary current that would produce the same magnetic moment of the $^{27}Co^{60}$ nucleus. The physics of the mirror image (a parity reversal) of this reaction is not the same, as shown in Fig. 1.1. In the mirror image, the electron emission is right handed. Thus, the decay does not conserve parity.

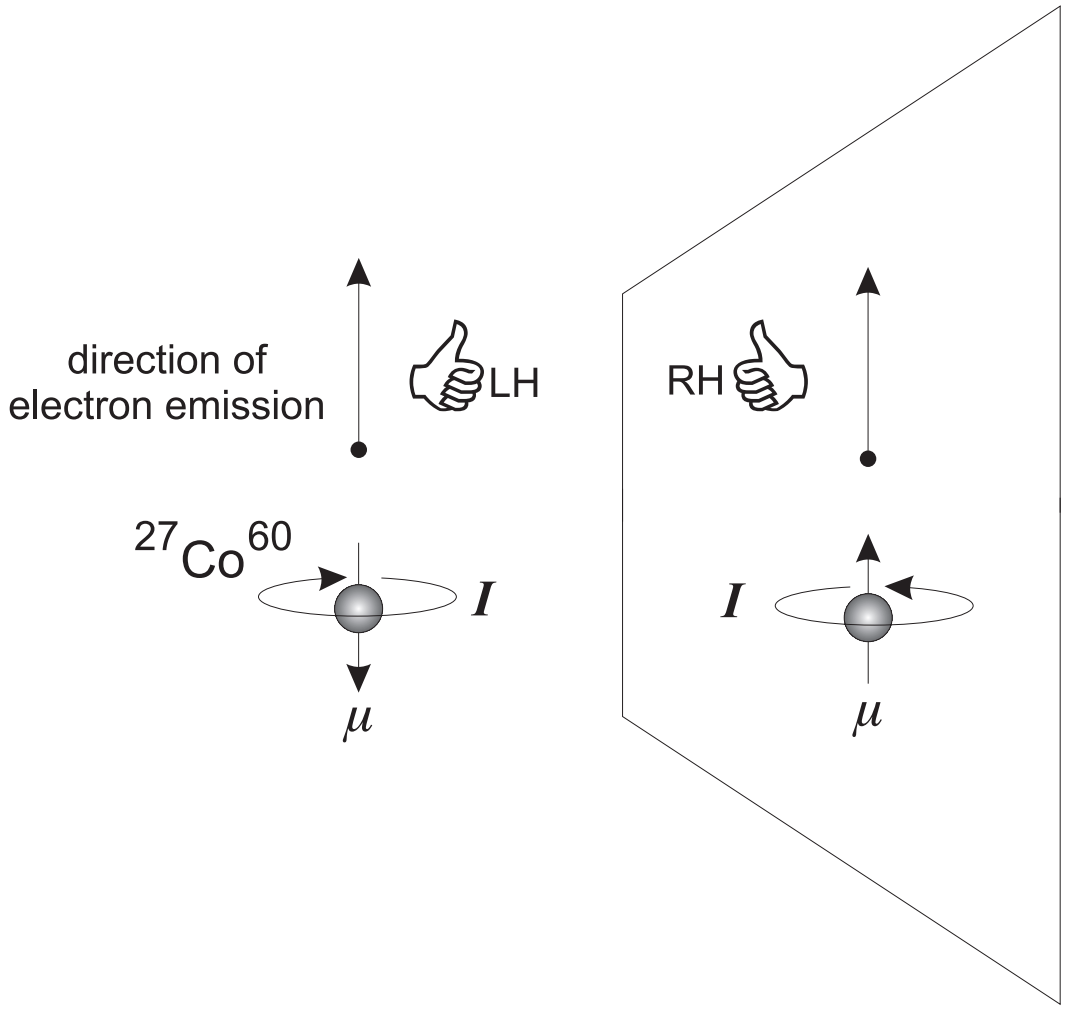

Figure 1.1: A picture of beta decay in the $^{27}Co^{60}$ nucleus. Electrons are emitted in a preferred direction opposite the magnetic moment of the nucleus. In a parity reversal, the direction of the magnetic moment changes, but the direction of electron emission does not. Thus, beta decay process does not conserve parity.

1.2 The Standard Model

The force that is responsible for beta decay is the weak force, which has been unified with the electromagnetic force by a theory developed by Glashow [3], Salam [4], and Weinberg [5] in the 1960's. The Glashow-Salam-Weinberg model unifies the two forces into the electroweak force and, when combined with quantum chromodynamics, is known as the standard model. Part of this model describes the electroweak interaction between six quarks (the up, down, strange, charm, bottom, and top quarks) and six leptons (the electron, muon, tauon, and their three neutrinos). The electroweak force is mediated by four particles: the neutral photon and Z^0 boson, and the charged $W^{\pm}$ bosons.

Although the standard model predicts the electroweak interactions between particles, it is silent as to the masses of those particles. There are also three additional parameters, the fine-structure constant, α, the Fermi constant G_F, and the Weinberg angle, θ_W, whose values must be determined from experiment. In addition, the mechanism for the quarks and leptons to acquire mass is the so-called Higgs mechanism, which is mediated by the Higgs boson. The Higgs boson has never been seen, and the Higgs mechanism is poorly understood.

For the above reasons, physicists have been devoting massive amounts of time and effort to test the standard model. The high energy physics community has achieved great success in their experiments [6] (although the funding for the Superconducting Super Collider, which may have found the Higgs boson, was terminated), and many in the atomic physics community have devoted their efforts to understanding PNC in atoms to test the standard model, as suggested by Bouchiat and Bouchiat [7, 8]. Both communities' experiments have now reached the level of precision where they can test the radiative corrections and search for new physics beyond the standard model.

1.3 Parity Nonconservation in Atoms

Parity nonconservation in atoms comes from the the exchange of a Z^0 boson between an electron and a quark inside the nucleus. This interaction is to the weak force as the exchange of a photon between an electron and a proton is to the electromagnetic force. Feynman diagrams comparing these two interactions are shown in Fig. 1.2. The exchange of a Z^0 boson gives rise to a Hamiltonian that is

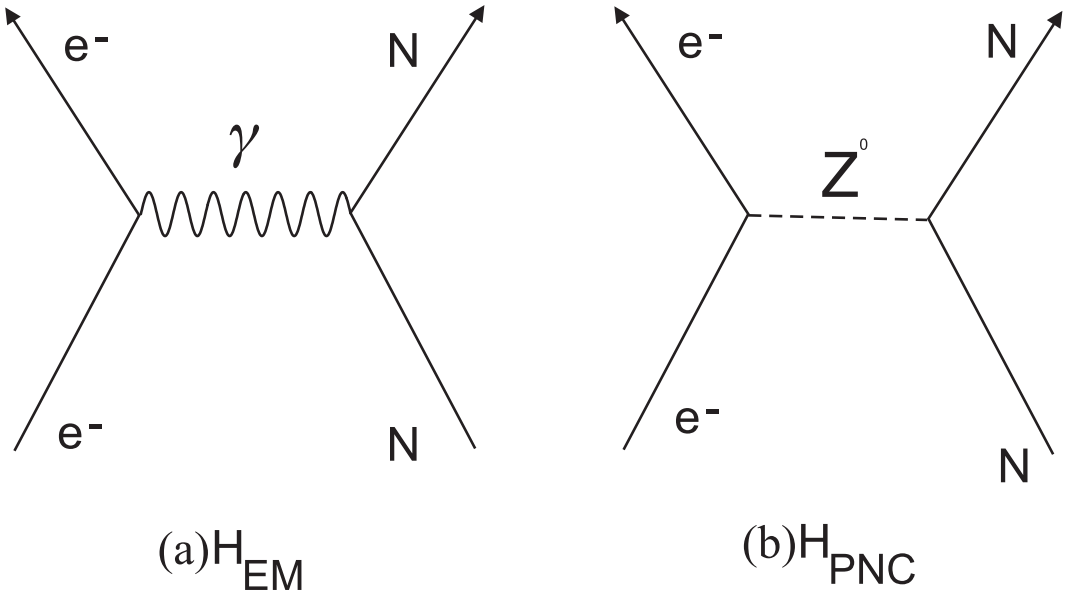

Figure 1.2: Two Feynman diagrams showing (a) electromagnetic interaction via an exchange of a photon and (b) the weak interaction via the exchange of a Z^0 boson. Here N is a nucleon.

proportional to the Dirac matrix γ^5 and the weak charge Q_W. The weak charge is a neutral analog to the electric charge e, and wherever there is an electromagnetic interaction via the exchange of a photon there is also a neutral weak interaction. In atoms, the neutral weak interaction mixes eigenstates with opposite parity, and thus provides a mechanism for electric dipole transitions that do not conserve parity. Experiments that measure the PNC electric dipole transition give access to the value of Q_W, which can then be compared to the standard model prediction.

There are two types of experiments that are typically used to measure the effect of PNC mixing: optical rotation experiments and Stark interference experiments. In optical rotation experiments [9, 10, 11, 12], linear laser light is directed through an atomic vapor. The PNC mixing induces birefringence in the vapor, and causes a rotation of the polarization of the incident light. The angle of rotation is measured and can be used to determine Q_W. Stark interference experiments measure the interference between the small PNC-induced amplitude and a larger electric-field induced electric dipole amplitude.

1.4 Parity Nonconservation Interference Measurements in Cesium

The most precise atomic PNC measurement to date [13] measures the interference between the PNC amplitude and the Stark-induced amplitude between the $6S$ and $7S$ states of cesium. The PNC amplitude is given by

$$E_{\rm PNC} \equiv \overline{\langle 7S \mid} \, \vec{D} \, \overline{\mid 6S \rangle} = (\frac{Q_W}{N}) k_{\rm PNC}, \tag{1.1}$$

where the bars over the bra and the ket indicate that they have small amounts of opposite parity states mixed into the pure parity eigenstates. Here, e is the electron charge, a_0 is the Bohr radius, N is the number of neutrons in the atom, and $k_{\rm PNC}$ is the value of a combination of the relevant parity conserving and PNC matrix elements. It is calculated using the *ab initio* theory of Blundell *et al.* [14] and of Dzuba *et al.* [15]. The quantity measured in Ref. [13] is the ratio of two amplitudes, $\mathrm{Im}(E_{\rm PNC})/\beta$, where β is the tensor transition polarizability that characterizes the strength of the Stark-induced transition. The test of the standard model is through the equation

$$\frac{\mathrm{Im}(E_{\rm PNC})}{\beta} = -i \frac{Q_W}{\beta N} k_{\rm PNC}. \tag{1.2}$$

This equation contains the motivation for all of the work presented in this thesis.

1.5 Motivation for the Present Work

Equation (1.2) connects the measurement of $\mathrm{Im}(E_{\mathrm{PNC}})/\beta$ and the calculation k_{PNC}, allowing the extraction of Q_W. This is atomic physics' link to the standard model.

The left side of the equation is the 0.35% measurement of Ref. [13]. The amplitude E_{PNC} is too small to measure by itself, so the experiment measures it relative to β. The right side contains Q_W, which is the quantity we wish to know, but it also contains two other parameters needed to interpret the experiment: k_{PNC} and β.

The constant k_{PNC} contains matrix elements of the Dirac matrix γ^5 that can only be calculated. Therefore, prior to this work, the uncertainty of k_{PNC} was limited by the 1% uncertainty in the atomic theory calculations. Further, while β has been determined semi-empirically, the best value was again from a 1% atomic theory calculation [14].

Because the goal of PNC measurements in cesium is a high-precision test of the standard model, as a first objective we would like to reduce the uncertainty due to the calculations. The work presented in this thesis achieves this objective.

The main stumbling block in the way of reducing the uncertainty in k_{PNC} is a 2% difference between the measurement and the calculation of the dc Stark shift of the $6S \rightarrow 7S$ transition in cesium. Because the level of agreement between experiment and theory is one indicator of the accuracy of the theory, this difference was of great concern and prevented a reduction in the uncertainty below 1%. In order to resolve this problem, we have measured the dc Stark shift, and our new measurement agrees with the predictions to 0.3%.

Our previous result for Q_W [13] used the calculated value of β from Ref. [14]. We have performed a new measurement that allows the determination of β to 0.3%, which can then be used instead of the calculation. This reduces the number of

quantities that need to be calculated to determine Q_W from two to one. In addition, our result for β can be used as an additional test of the atomic theory.

This thesis is arranged as follows. Chapters 2 and 3 discuss the theory and apparatus used in the experiments described in subsequent chapters, Chapter 4 discusses the measurement of the dc Stark shift, Chapter 5 covers the determination of β, and Chapter 6 discusses the implications of the two experiments on tests of the standard model. Finally, Chapter 7 discusses the possibility of additional improvements or new measurements that may be useful for future tests of the standard model.

CHAPTER 2

THEORY

Using atomic PNC to test the standard model brings together two disparate fields of physics: high-energy physics and atomic physics. It is not the purpose of this chapter to write at length about the underlying theories. Instead, this chapter presents enough theory so that the atomic physics measurements can be understood, and it also illustrates the way in which the measurements provide a test of the standard model. The theory of the weak interaction is covered in detail in the literature, and the reader is referred there for technical details and for general information on atomic theory [16, 17, 18, 19]. Here only an overview will be provided.

This chapter covers the theory necessary to understand the experiments discussed and the implications of those experiments. In addition to the general theory, this chapter also covers the effects of external magnetic fields and their alignment with respect to the experimental apparatus, and it details the exact transition rates the experiments measure. Much of the content of this chapter closely follows the theses of Gilbert [20], Noecker [21], Masterson [22], and Wood [23].

2.1 Weak Interaction

The weak interaction can be mediated by the exchange of a Z^0 boson between an electron and a quark. This exchange, shown in Fig. 1.2(b), is analogous to the exchange of a photon for the electromagnetic interaction, shown in Fig. 1.2(a). In the present form of the standard model, the weak interaction is described by a

Hamiltonian given by

$$H_{\rm PNC} = \frac{1}{2\sqrt{2}} G_F Q_W \gamma^5 \rho_N(r), \tag{2.1}$$

where G_F is the Fermi constant, $\rho_N(r)$ is the nuclear density, and γ^5 is the Dirac matrix, which is responsible for PNC. The weak charge of the nucleus, Q_W, is analogous to the electric charge for the electromagnetic interaction. For an atom with atomic number Z and N neutrons, the value of Q_W is given by

$$Q_W = 2[(2Z+N)C_{1u} + (Z+2N)C_{1d}], \tag{2.2}$$

where C_{1u} and C_{1d} are electron-quark coupling constants for the up and down quarks, respectively, which are described in Chapter 1. Thus, Q_W is atomic physics' "window" into the standard model. At tree level* Q_W is given by

$$Q_W = -(N - Z + 4\sin^2\theta_W), \tag{2.3}$$

where $\sin^2\theta_W$ is the Weinberg angle. Any deviation from the tree level value of Q_W indicates the need for higher order corrections (such as the so-called "radiative corrections") or signals a breakdown in the standard model predictions.

The weak interaction does not conserve parity, so $H_{\rm PNC}$ mixes states of opposite parity as in

$$\overline{\mid \psi \rangle} = \mid \psi^+ \rangle + \sum_i \mid \phi_i^- \rangle \frac{\langle \phi_i^- \mid H_{\rm PNC} \mid \psi^+ \rangle}{E_\psi - E_{\phi_i}} \tag{2.4}$$

where the "+" and "−" indicate opposite parity states. The matrix elements $\langle \phi_i^- \mid H_{\rm PNC} \mid \psi^+ \rangle$ are essentially matrix elements of γ^5. The operator γ^5 does not appear in any atomic observable, so the values of these matrix elements must be calculated. The

*Tree level is essentially the lowest order of the theory.

Bouchiats [8] have shown that in the non-relativistic approximation

$$\langle n'\ell' \mid H_{\rm PNC} \mid n\ell \rangle \propto \left(R_{n'\ell'}(r) \frac{\partial R_{n\ell}(r)}{\partial r} \right) \Big|_{r=0,} \tag{2.5}$$

where n is the principal quantum number, ℓ is the orbital angular momentum quantum number, and $R_{n\ell}(r)$ is the radial wave function of the $|\, n\ell\rangle$ state. Because $R_{n\ell}(r) \approx r^{\ell} Z^{\ell+\frac{1}{2}}$ for small r, $H_{\rm PNC}$ mixes only S and P states, and to a good approximation it only mixes states with $J = 1/2$.

2.2 Cesium Energy Level Structure.

Atomic cesium has a single valence electron with a Xenon-like core. We use the stable isotope ^{133}Cs, which has 55 protons and 78 neutrons. It has nuclear spin $I = 7/2$, electronic spin $S = 1/2$, orbital angular momentum $L = 0, 1, \ldots$, and total electronic angular momentum $\vec{J} = \vec{L} + \vec{S}$. Its total angular momentum is given by $\vec{F} = \vec{I} + \vec{J}$, so with $J = 1/2$ there are two hyperfine levels: $F = 3$ and 4. With $J = 3/2$ there are four hyperfine levels: $F = 2, 3, 4$, and 5. The projection of F onto the quantization axis is given by $m_F = -F, -F+1, \ldots, F-1, F$. The most important of these energy levels are shown in Fig. 2.1.

Perhaps the most familiar spectral features of atomic cesium are the so-called "D1" and "D2" lines, which are electric dipole transitions from the $6S_{1/2}$ ground state to the $6P_{1/2}$ and $6P_{3/2}$ states, respectively. The work in this thesis uses the D2 line for optical pumping and for detection, and it uses the normally forbidden transition between the $6S_{1/2}$ and $7S_{1/2}$ states to study the interesting science.

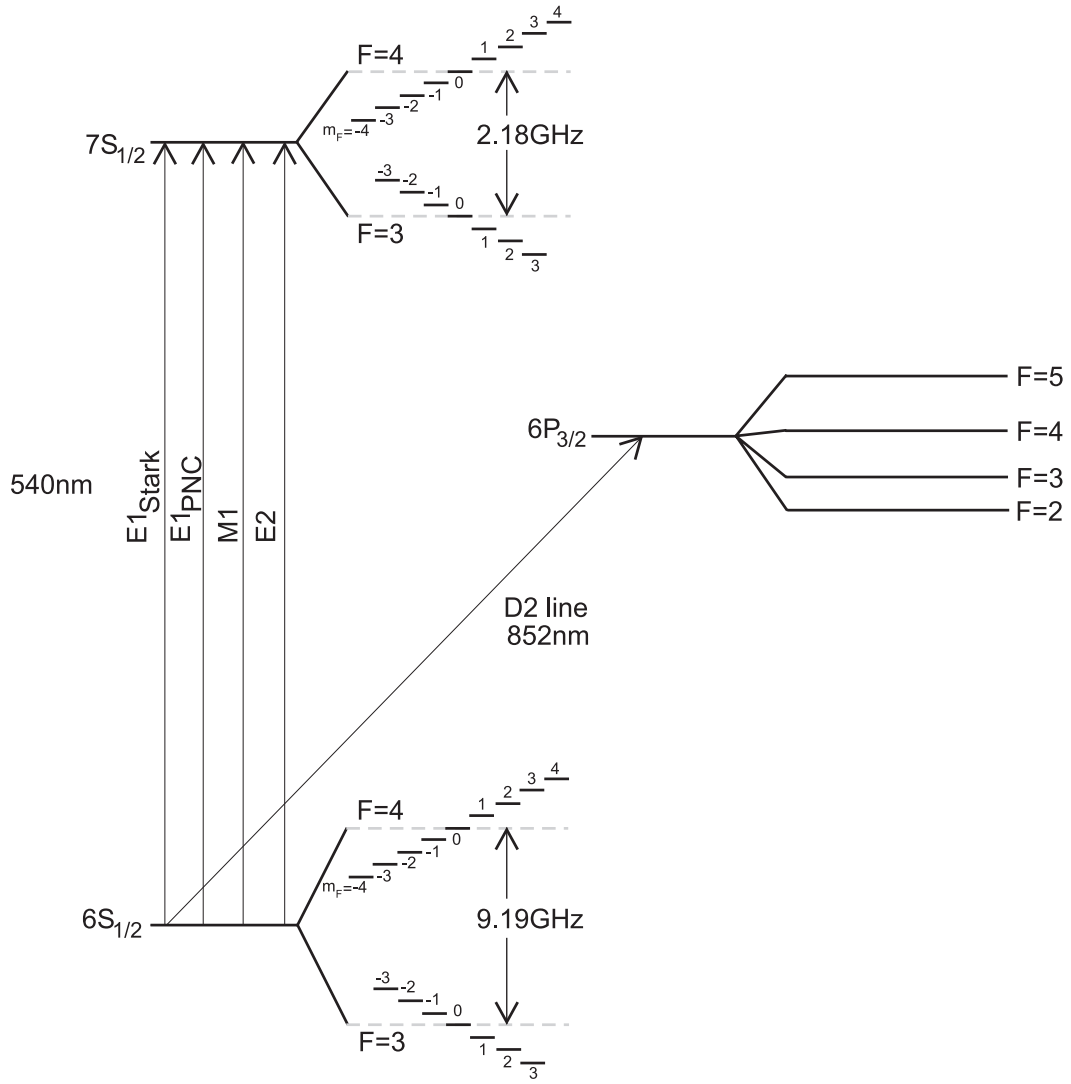

Figure 2.1: The lowest energy levels of the cesium atom. The mechanisms giving rise to the $6S \rightarrow 7S$ transition are shown, as well as hyperfine structure of all the states and the Zeeman structure of the $6S$ and $7S$ states. The $6P_{1/2}$ state is not shown because of its relative unimportance for the work presented in this thesis. Energy splittings are not shown to scale in this figure.

2.3 Electric Dipole Amplitudes

2.3.1 Parity Nonconserving Amplitude

In cesium, the mixing of S and P states by the weak interaction discussed in Section 2.1 is given by

$$\overline{\mid nSFm_F\rangle} = \mid nSFm_F\rangle + \sum_{n'} \mid n'P\rangle \frac{\langle n'P \mid H_{\rm PNC} \mid nSFm_F\rangle}{E_{nS} - E_{n'P}}. \tag{2.6}$$

In the presence of an oscillating laser field with electric field polarization $\vec{\epsilon}$, there is an $E1$ amplitude between the $6S$ and $7S$ states of cesium. This amplitude is given by

$$\begin{aligned}
(E1_{\rm PNC})^{F'm'_F}_{Fm_F} &= \overline{\langle 7SF'm'_F \mid} - e\vec{\epsilon}\cdot\vec{r}\overline{\mid 6SFm_F\rangle} \\
&= \sum_n \left(\frac{\langle 7SF'm'_F \mid H_{\rm PNC} \mid nP\rangle}{E_{7S} - E_{nP}} \langle nP \mid \vec{D} \mid 6SFm_F\rangle \right. \\
&\quad \left. + \langle 7SF'm'_F \mid \vec{D} \mid nP\rangle \frac{\langle nP \mid H_{\rm PNC} \mid 6SFm_F\rangle}{E_{6S} - E_{nP}} \right) \\
&= i{\rm Im}(E_{\rm PNC})\vec{\epsilon}\cdot\langle F'm'_F \mid \vec{\sigma} \mid Fm_F\rangle,
\end{aligned} \tag{2.7}$$

where the unprimed quantum numbers are for the ground state and the primed quantum numbers are for the excited state, and the operator $\vec{\sigma}$ is the Pauli spin matrix. The constant $E_{\rm PNC}$ contains all the radial information as well as the connection to the standard model:

$$\begin{aligned}
E_{\rm PNC} &= \sum_n \left(\frac{\langle 7S \mid H_{\rm PNC} \mid nP\rangle\langle nP \mid \vec{D} \mid 6S\rangle}{E_{7S} - E_{nP}} + \right. \qquad (2.8) \\
&\qquad \left. \frac{\langle 7S \mid \vec{D} \mid nP\rangle\langle nP \mid H_{\rm PNC} \mid 6S\rangle}{E_{6S} - E_{nP}} \right). \qquad (2.9)
\end{aligned}$$

the geometrical matrix element $\langle F'm'_F \mid \vec{\sigma} \mid Fm_F\rangle$ can be written in terms

of the $C_{Fm_F}^{F'm'_F}$ coefficients:

$$C_{Fm_F}^{F'm_F+q} \equiv \left(\frac{1}{\sqrt{2}}\right)^{|q|} \langle F'm_F + q \mid \sigma_{1q} \mid Fm_F\rangle, \tag{2.10}$$

where $q = 0, \pm 1$. These coefficients are simply combinations of Clebsch-Gordan coefficients, and they are tabulated in Appendix A. The PNC amplitude can then be written as

$$\begin{aligned}(E1_{\rm PNC})_{Fm_F}^{F'm'_F} = i{\rm Im}(E_{\rm PNC}) \;\; [&(\mp\epsilon_x + i\epsilon_y) \\ &\times C_{Fm_F}^{F'm_F\pm1}\delta_{m_F m'_F\mp1} + \epsilon_z C_{Fm_F}^{F'm_F}\delta_{mm'}],\end{aligned} \tag{2.11}$$

where we have evaluated the dot product $\vec{\epsilon}\cdot\vec{\sigma}$ in Eq. (2.7). Note that the operators σ_x and σ_y drive $\Delta m_F = \pm 1$ transitions and σ_z drives $\Delta m_F = 0$ transitions.

2.3.2 Stark-Induced Amplitude

An applied external dc electric field $\vec{E}$ polarizes the cesium atom and also mixes states in a similar way the weak interaction does in Eq. (2.4) with $H_{\rm PNC}$ replaced with $e\vec{E}\cdot\vec{r}$. An oscillating laser field then drives the Stark-induced $6S \to 7S$ amplitude given by

$$\begin{aligned}(E1_{\rm Stark})_{Fm_F}^{F'm'_F} = \sum_{n,J,F'',m''_F} \Bigg\{ &\frac{\langle 7SF'm'_F \mid e\vec{E}\cdot\vec{r} \mid nP_JF''m''_F\rangle\langle nP_JF''m''_F \mid e\vec{\epsilon}\cdot\vec{r} \mid 6SFm_F\rangle}{E_{7S} - E_{nP_J}} \\ + &\frac{\langle 7SF'm'_F \mid e\vec{\epsilon}\cdot\vec{r} \mid nP_JF''m''_F\rangle\langle nP_JF''m''_F \mid e\vec{E}\cdot\vec{r} \mid 6SFm_F\rangle}{E_{7S} - E_{nP_J}}\Bigg\}.\end{aligned} \tag{2.12}$$

The Bouchiats [8] showed that this complicated expression can be written in a simple form using an effective dipole operator:

$$\begin{aligned}(E1_{\rm Stark})_{Fm_F}^{F'm'_F} &= \vec{\epsilon}\cdot\langle 7SF'm'_F \mid \vec{r}_{\rm effective} \mid 6SFm_F\rangle \\ &= \alpha\vec{E}\cdot\vec{\epsilon}\,\delta_{F,F'}\delta_{m_F m'_F} + i\beta\vec{\epsilon}\cdot\langle F'm'_F \mid \vec{\sigma}\times\vec{E} \mid Fm\rangle \\ &= \alpha\vec{E}\cdot\vec{\epsilon}\,\delta_{F,F'}\delta_{m_F m'_F} + i\beta(\vec{E}\times\vec{\epsilon})\cdot\langle F'm'_F \mid \vec{\sigma} \mid Fm\rangle.\end{aligned} \tag{2.13}$$

Here α and β are the scalar and tensor transition polarizabilities, respectively. They are given by [8, 24]

$$\begin{aligned}\alpha &= \frac{e^2}{9}\sum_n \left[\langle 7S \mid r \mid nP_{1/2}\rangle\langle nP_{1/2} \mid r \mid 6S\rangle \left(\frac{1}{E_{7S}-E_{nP_{1/2}}}+\frac{1}{E_{6S}-E_{nP_{1/2}}}\right)\right. \\ &+ \left. 2\,\langle 7S \mid r \mid nP_{3/2}\rangle\langle nP_{3/2} \mid r \mid 6S\rangle \left(\frac{1}{E_{7S}-E_{nP_{3/2}}}+\frac{1}{E_{6S}-E_{nP_{3/2}}}\right)\right], \quad (2.14)\end{aligned}$$

and

$$\begin{aligned}\beta &= \frac{e^2}{9}\sum_n \left[\langle 7S \mid r \mid nP_{1/2}\rangle\langle nP_{1/2} \mid r \mid 6S\rangle \left(\frac{1}{E_{7S}-E_{nP_{1/2}}}-\frac{1}{E_{6S}-E_{nP_{1/2}}}\right)\right. \\ &- \left. \langle 7S \mid r \mid nP_{3/2}\rangle\langle nP_{3/2} \mid r \mid 6S\rangle \left(\frac{1}{E_{7S}-E_{nP_{3/2}}}-\frac{1}{E_{6S}-E_{nP_{3/2}}}\right)\right]. \quad (2.15)\end{aligned}$$

The $\Delta F = 0$ transitions are dominated by the α term because $\alpha/\beta = -9.905(11)$ [25]. Here $\langle nS \mid r \mid nP\rangle$ are effective radial integrals which are related to reduced matrix elements by [24]

$$\langle nS \mid\mid r \mid\mid n'P_{1/2}\rangle = \langle n'P_{1/2} \mid\mid r \mid\mid nS\rangle = \sqrt{\frac{2}{3}}\langle nS \mid r \mid n'P_{1/2}\rangle \quad (2.16)$$

and

$$\langle nS \mid\mid r \mid\mid n'P_{3/2}\rangle = -\langle n'P_{3/2} \mid\mid r \mid\mid nS\rangle = \sqrt{\frac{4}{3}}\langle nS \mid r \mid n'P_{3/2}\rangle. \quad (2.17)$$

We use these forms of Eqs. (2.14) and (2.15) to emphasize the fact that α is the **sum** of similar sized terms and β is the **difference** of similar sized terms. Thus, the fractional uncertainty of α is comparable to or better than the fractional uncertainty of its individual terms, while the fractional uncertainty of β is much worse than that of its individual terms.

If we evaluate the dot product as before, the Stark-induced amplitude can

be written as

$$(E1_{\rm Stark})^{F'm'_F}_{Fm_F} = \alpha\vec{E}\cdot\vec{\epsilon}\,\delta_{FF'}\delta_{m_F m'_F} + i\beta(\vec{E}\times\vec{\epsilon})_z C^{F'm_F}_{Fm_F}\delta_{m_F m'_F} \quad (2.18)$$
$$+ \beta[\mp i(\vec{E}\times\vec{\epsilon})_x - (\vec{E}\times\vec{\epsilon})_y]C^{F'm_F\pm1}_{Fm_F}\delta_{m_F m'_F\mp1}.$$

The Stark-induced and PNC electric dipole amplitudes differ significantly in size. If the D1 amplitude has a strength on the order of unity, $E1_{\rm Stark}$ has a strength of 3×10^{-5} when $E = 500$ V/cm, and $E1_{\rm PNC}$ has a strength of 10^{-11}.

2.4 Magnetic Dipole Amplitudes

Although to first order magnetic dipole ($M1$) amplitudes vanish between states with different n, relativistic effects [26] and the off-diagonal hyperfine interaction [8] both contribute to a small amplitude between the $6S$ and $7S$ states. The Hamiltonian for this interaction connecting S states is given by

$$H_{M1} = \vec{\mu}\cdot\vec{B}_{\rm ac} = \frac{\mu_{\rm B}}{\hbar}(\hat{L}+2\hat{S})\cdot\vec{B}_{\rm ac} \quad (2.19)$$
$$= \mu_{\rm B}\vec{\sigma}\cdot\vec{B_{\rm ac}} \quad (2.20)$$

where $\mu_{\rm B}$ is the Bohr magneton, $\vec{\sigma} = 2\hat{S}/\hbar$ is the Pauli spin operator, and if $\vec{k}$ is the propagation vector of the laser, $\vec{B}_{\rm ac} = \vec{k}\times\vec{\epsilon}$ is the oscillating magnetic field of the laser. $\hat{L}$ and $\hat{S}$ are the electron angular momentum and spin operators, respectively. The amplitude for the $M1$ transition is then given by

$$M1^{F'm'_F}_{Fm_F} = \langle 7SF'm'_F \mid H_{M1} \mid 6SFm_F\rangle = M1(\vec{k}\times\vec{\epsilon})\cdot\langle F'm'_F \mid \vec{\sigma} \mid Fm_F\rangle, \quad (2.21)$$

where the radial integrals have been incorporated into the constant $M1$. The radial part can be written as

$$M1 = M \pm M_{\rm hf}\delta_{F,F'\pm1}, \quad (2.22)$$

where M is from relativistic effects, and $M_{\rm hf}$ is from the off-diagonal hyperfine interaction. The $M1$ amplitude has a size of about 2×10^{-6} compared with the D1 line. As before, Eq. (2.21) can be written as

$$M1_{Fm_F}^{F'm'_F} = M1\{[\ \mp(\vec{k}\times\vec{\epsilon})_x + i(\vec{k}\times\vec{\epsilon})_y] \times C_{Fm_F}^{F'm_F\pm1}\delta_{m_F m'_F\mp1} + (\vec{k}\times\vec{\epsilon})_z C_{Fm_F}^{F'm_F}\delta_{m_F m'_F}\}. \tag{2.23}$$

2.5 Electric Quadrupole Interaction

Another transition that is driven by a laser field is the electric quadrupole transition ($E2$), which arises from mixing of $\langle n'D\rangle$ states with $\langle nS\rangle$ states by the off-diagonal hyperfine interaction. This amplitude is very small compared to the allowed $E1$ transitions and even the $M1$ transition ($E2/M \approx 0.01$). However, in order to test the standard model at the few tenths of a percent level, we must account for the small effects of the $E2$ amplitude, as discussed in Section 5.4 and Appendix B. In our case, the $E2$ amplitude requires us to correct our data by only $\sim 0.08\%$; in other experiments the necessary correction is as large as 3% [27]. Because the effect of $E2$ on our measurements is so small, we can determine the ratio $E2/M_{\rm hf}$ by comparing our result for $M_{\rm hf}/M$ with other results that were affected by $E2$. See, for example, Ref. [28] and Section 5.4. A phenomenological discussion of $E2$ following the treatment of Ref. [29] will be presented in Section 5.4.

2.6 Effect of Misaligned $\vec{B}$

In the foregoing discussion it has been assumed that the quantization axis is along $\hat{z}$. It is important to ask what happens if the magnetic field is slightly misaligned from the $\hat{z}$ axis.

The effect of a misaligned magnetic field is to change the definition of the operator $\vec{\sigma}$. The Pauli spin matrix is defined assuming a quantization axis along $\hat{z}$, so we must rotate $\vec{\sigma}'$, which is defined with $\vec{B} = B\hat{z}'$, into the experimental

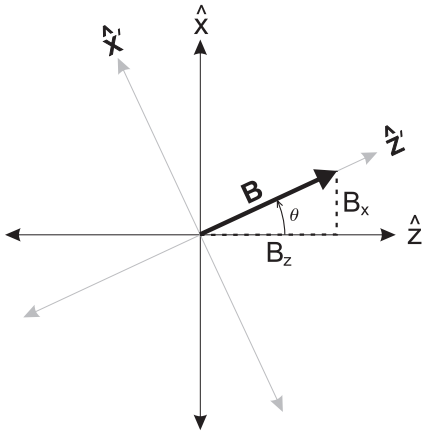

Figure 2.2: A picture showing magnetic field misaligned into the $\hat{x}$ direction.

coordinate system where $\vec{B} = B_x\hat{x} + B_y\hat{y} + B_z\hat{z}$. Using Fig. 2.2 it is easy to see that $\hat{z} = \cos\theta\hat{z}' - \sin\theta\hat{x}'$ and $\hat{x} = \sin\theta\hat{z}' + \cos\theta\hat{x}'$, where $\cos\theta = B_z/B$ and $\sin\theta = B_x/B$. A similar rotation can be performed if $\hat{y}$ replaces $\hat{x}$ in the formulas. The components of the Pauli spin matrix are then given by

$$\begin{aligned} \sigma_x &= \frac{B_z}{B}\sigma'_x + \frac{B_x}{B}\sigma'_z \\ \sigma_y &= \frac{B_z}{B}\sigma'_y + \frac{B_y}{B}\sigma'_z \\ \sigma_z &= \frac{B_z}{B}\sigma'_z - \frac{B_x}{B}\sigma'_x - \frac{B_y}{B}\sigma'_y. \end{aligned} \tag{2.24}$$

Simple algebra then shows that the $C_{Fm_F}^{F'm'_F}$ coefficients are transformed into

$$C_{Fm_F}^{F'm'_F\pm1}\delta_{m_Fm'_F\mp1} \to C_{Fm_F}^{F'm'_F\pm1}\delta_{m_Fm'_F\mp1} \mp \left(\frac{B_x}{B} \pm i\frac{B_y}{B}\right) C_{Fm_F}^{F'm_F}\delta_{m_Fm'_F}. \tag{2.25}$$

This means that a misaligned magnetic field introduces $\Delta m_F = 0$ transitions where there should only be $\Delta m_F = \pm 1$ transitions. The form of $C_{Fm_F}^{F'm_F}\delta_{m_Fm'_F}$ is also changed, but it is not important for our purposes and so it is omitted.

2.7 Measured Transition Rates

As we have seen, in the presence of an external dc electric field and a cw laser field there are five different amplitudes connecting the $6S$ and $7S$ states of cesium: the PNC and Stark-induced $E1$ amplitudes, the $M1$ amplitudes from relativistic effects and off-diagonal hyperfine interactions, and the tiny $E2$ amplitude. There are four hyperfine components to the $6S \rightarrow 7S$ transition: the $\Delta F = 0$ $F = 3$ to $F' = 3$ and $F = 4$ to $F' = 4$, and the $\Delta F = \pm 1$ $F = 3$ to $F' = 4$ and $F = 4$ to $F' = 3$. All the experiments discussed in this thesis use $\vec{E} = E\hat{x}$, $\vec{B} = B\hat{z}$*, and $\vec{k} = \hat{y}$, and a general normalized polarization $\vec{\epsilon} = \epsilon_z \hat{z} + (\epsilon_x + i\epsilon_i)\hat{x}$.

The most recent PNC measurement performed by our group measured the interference between the Stark-induced and PNC electric dipole amplitudes. The geometry in that experiment used $E \simeq 500$ V/cm, $B \simeq 6.6$ G, $\epsilon_i/\epsilon_z \simeq 1$ and 2, and $\epsilon_x = 0$. The final quantity measured was the ratio of the two amplitudes for $\Delta F = \pm 1$ transitions given by**

$$R_{Fm_F}^{F'm'_F} = 2\frac{\mathrm{Im}(E_{\mathrm{PNC}})}{\beta E}\frac{\epsilon_i}{\epsilon_z}\frac{\sum_{m_F} \pm f_{m_F} d_{m_F} \left(C_{Fm_F}^{F'm_F\pm1}\right)^2}{\sum_{m_F} f_{m_F} d_{m_F} \left(C_{Fm_F}^{F'm_F\pm1}\right)^2}, \tag{2.26}$$

where f_{m_F} is the fractional population in a Zeeman sublevel m_F, d_{m_F} is a detuning factor that accounts for the non-degeneracy of different Zeeman transitions (see Section 2.8). The value $\mathrm{Im}(E_{\mathrm{PNC}})/\beta$ can then be extracted if all the other quantities are measured.

In order to measure the dc Stark shift (see Chapter 2.18) we use the $F = 3$ to $F' = 3$ transition. We use electric fields from 1 kV/cm to 10 kV/cm, with $\vec{E} = E\hat{x}$,

*In this section we ignore the problem of misaligned magnetic fields. That will be addressed in Chapter 5

**Actually, the ratios measured on the $\Delta F = \pm 1$ transitions are slightly different because of nuclear PNC. This difference will be ignored in this thesis.

$B = 0$, and $\vec{\epsilon} = \epsilon_x \hat{x} + \epsilon_z \hat{z}$. The transition rate from Eq. (2.12) is simply

$$\mid (E1_{\rm Stark})^{Fm'_F}_{Fm_F} \mid^2 \simeq [\alpha^2 E^2 \epsilon_x^2 \, \delta_{m_F m'_F} + \beta^2 E^2 \epsilon_z^2 (C^{Fm'_F}_{Fm_F})^2 \delta_{m_F m'_F \pm 1}] \Lambda^{E1}(I,\nu), \quad (2.27)$$

where $\Lambda^{E1}(I,\nu)$ is a line shape factor that depends on the intensity I and frequency ν of the excitation laser (see Ref. [30]), and the small $M1$ and $E2$ rates have been ignored.

To measure the tensor transition polarizability β we use the $\Delta F = \pm 1$ transitions. We also have $E = 700$ and 0 V/cm, $B = 4$ G, $\epsilon_z = 1$, and $\epsilon_x = \epsilon_i = 0$. With $E = 0$ V/cm the transition rates from Eq. (2.23) are

$$\mid (M1)^{F\pm 1 m'_F}_{Fm_F} \mid^2 \simeq (M \mp M_{\rm hf})^2 \Lambda^{M1}(I,\nu) (C^{F\pm 1 m'_F}_{Fm_F})^2. \quad (2.28)$$

With $E \simeq 700$ V/cm, [using Eq. (2.18)] they are

$$\mid (E1_{\rm Stark})^{F\pm 1 m'_F}_{Fm_F} \mid^2 \simeq \beta^2 E^2 \Lambda^{E1}(I,\nu) (C^{F\pm 1 m'_F}_{Fm_F})^2. \quad (2.29)$$

Here again, $\Lambda(I,\nu)$ is a line shape factor. The total rate for a given transition is found by summing over m_F and integrating over all ν. If we take the ratio of the total of these two rates, we have

$$R^{\pm} \equiv \left(\frac{M \mp M_{\rm hf}}{\beta E} \right)^2. \quad (2.30)$$

These two ratios can be combined with a semi-empirical value of $M_{\rm hf}$ [27] to determine β.

2.8 Zeeman Effect in Cesium

2.8.1 Effect on Eigenstates

The presence of a dc magnetic field mixes the hyperfine states and shifts the energies of the $2F+1$ Zeeman sublevels. For a small magnetic field, the effect can be treated as a perturbation, and the Hamiltonian is given by

$$H_Z = \frac{\mu_B}{\hbar}\left(\hat{L} + g_S\hat{S}\right)\cdot\vec{B} = \frac{\mu_B}{\hbar}g_S\hat{S}\cdot\vec{B}, \tag{2.31}$$

for $L=0$ states. In large magnetic fields, the different F states can be mixed into one another. However, for the fields used in this thesis and in Ref. [13, 23] the mixing is on the order of or less than 10^{-3} and is negligible. The energy shift for a given state is

$$\begin{aligned}\Delta\varepsilon_{nSFm_F} &= \langle nSFm_F \mid H_Z \mid nSFm_F\rangle \\ &= \mu_B g_F m_F B,\end{aligned} \tag{2.32}$$

where g_F is the Landè g-factor. For the $F=3$ and 4 states $\mid g_F \mid = 4$, so the magnitude of the frequency shift of each sublevel is given by

$$\Delta\nu_{m_F} = (0.35\ \mathrm{MHz/G})\, m_F B. \tag{2.33}$$

2.8.2 Effect on Spectrum

While the mixing of states due to an external magnetic field is negligible, the energy shifts due to the Zeeman effect have profound implications for PNC measurements and for the other measurements presented in this thesis. It is this shift in energy that made the 1988 PNC measurement [31] possible by completely resolving different $6SFm_F \rightarrow 7SF'm_F'$ transitions in a large field. In the 1997 PNC measurement [13], the magnetic field was smaller but the atomic beam was spin polarized.

Therefore, the Zeeman splitting allowed a correction for unwanted transitions that would not be possible without energy shifts. For the experiments described in this thesis, no discrimination is made between different Zeeman sublevels, so the energy shifts serve only to broaden the spectral features observed. In the absence of a magnetic field, there are only the four hyperfine transitions described in Section 2.7. These are shown in Fig. 2.3. The widths of these transitions will depend on, for

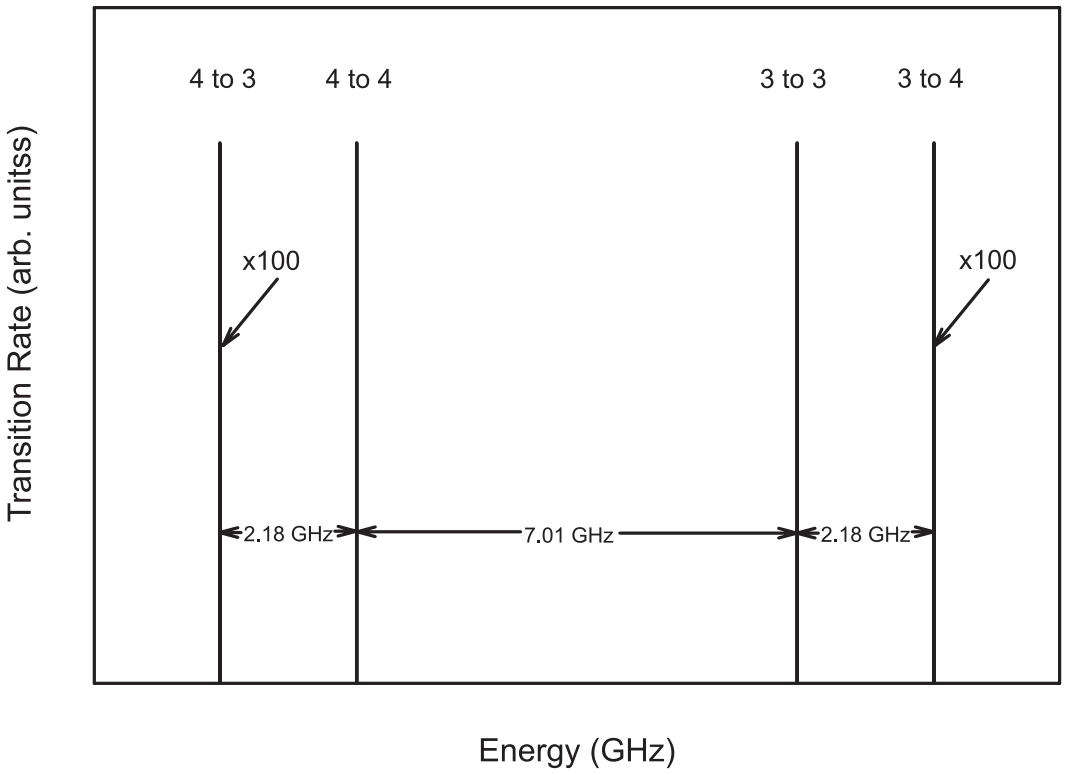

Figure 2.3: The four $6S \rightarrow 7S$ Stark-induced electric dipole hyperfine transitions in atomic cesium in the absence of an external magnetic field.

example, the Doppler width of the atomic beam or the intracavity intensity of the excitation laser.

In the presence of a magnetic field, the spectrum becomes much more complicated. As the Zeeman sublevels lose their degeneracy, each $6S \rightarrow 7S$ hyperfine transition splits into its underlying Zeeman transitions. For $\Delta F = 0$ transitions,

there are three spectral lines, one each for the $\Delta m_F = 0, \pm 1$ transitions, as shown in Fig. 2.4(a). However, for $\Delta F = \pm 1$ transitions, the Landè g-factors for different F levels have opposite signs. The result is the very complicated spectrum shown in Fig. 2.4(b).

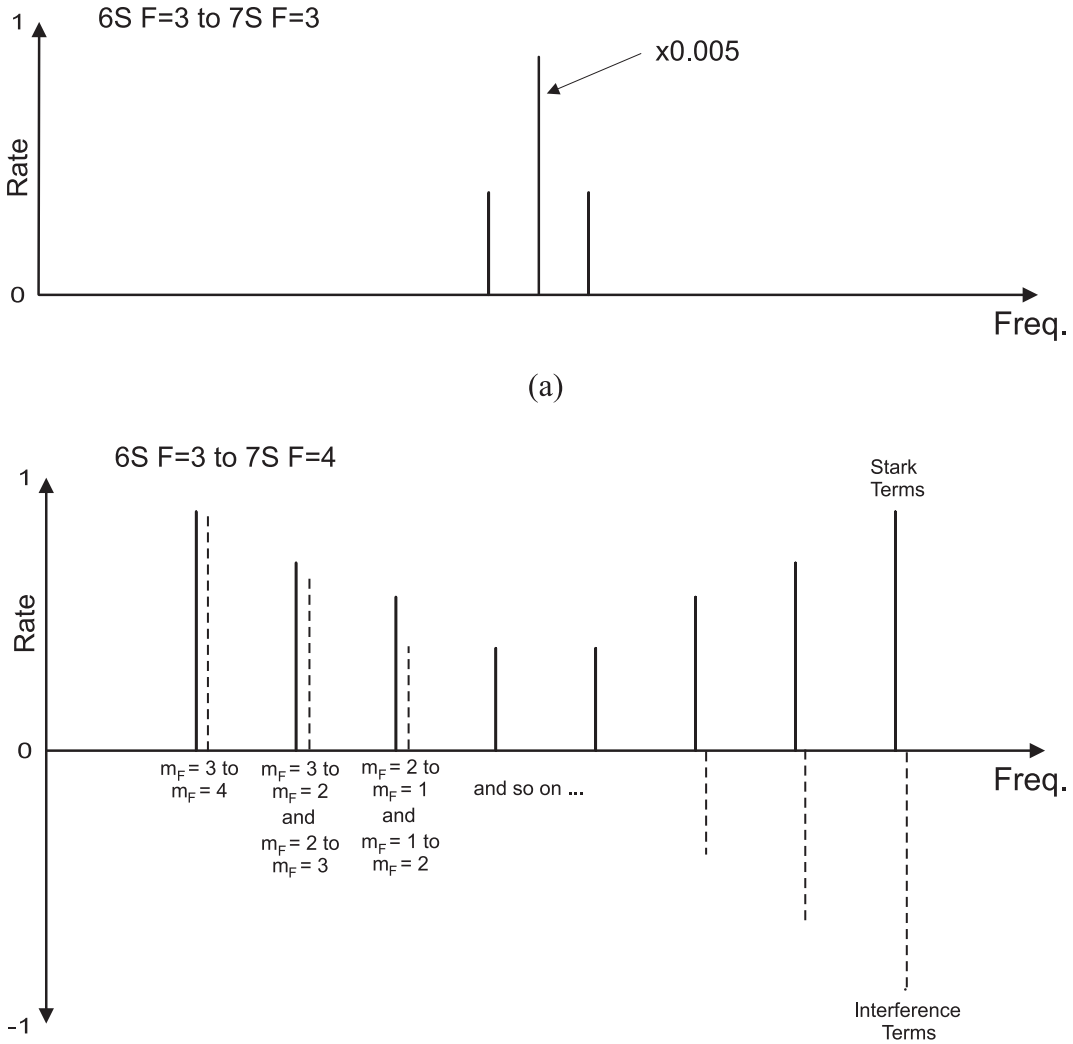

Figure 2.4: The Zeeman spectrum for $6S \rightarrow 7S$ transitions in a small magnetic field. (a) The spectrum for the $F = 3$ to $F = 3$ transition with the $\Delta m_F = 0$ peak greatly reduced. (b) The spectrum for the $F = 3$ to $F = 4$ transition. The Stark-induced rates are shown in solid lines and the Stark-PNC interference terms are shown in dashed lines and offset for clarity.

As mentioned earlier, this separation of different transitions made the 1988 PNC measurement possible. This is because the interference terms on opposite sides of the spectrum have opposite signs, as is shown in Fig. 2.4(b). Without the Zeeman splitting, and assuming an approximately uniform distribution among the Zeeman sublevels, all the interference terms sum to zero. If optical pumping is used to spin polarize the atomic beam as in the 1997 PNC experiment, the Zeeman splitting reduces the level of precision needed when measuring the degree of spin polarization. This point will be discussed in more detail in Section 7.3.

For measuring the dc Stark shift (Chapter 4), the Zeeman effect is unimportant because we use the $F = 3$ to $F' = 3$ transition, where all $\Delta m_F = q$ transitions that have the same value of q are degenerate. Here $q = 0$ or ± 1. For measuring β (Chapter 5), the Zeeman effect broadens the spectral feature but does not affect the total transition amplitudes we measure. Sample scans over the $E1$ $F = +1$ transition with small and large $\vec{B}$ are shown in Fig. 2.5.

In our measurement of β we would like to use as small a magnetic field as possible. This is because it is difficult to make scans over very large frequency ranges, and the smaller the magnetic field is, the narrower the transition will be. However, there is a systematic error that is proportional to the ratio of B_i/B_z, where $i = x$ or y, so we compromise and use an intermediate magnetic field of 4 G.

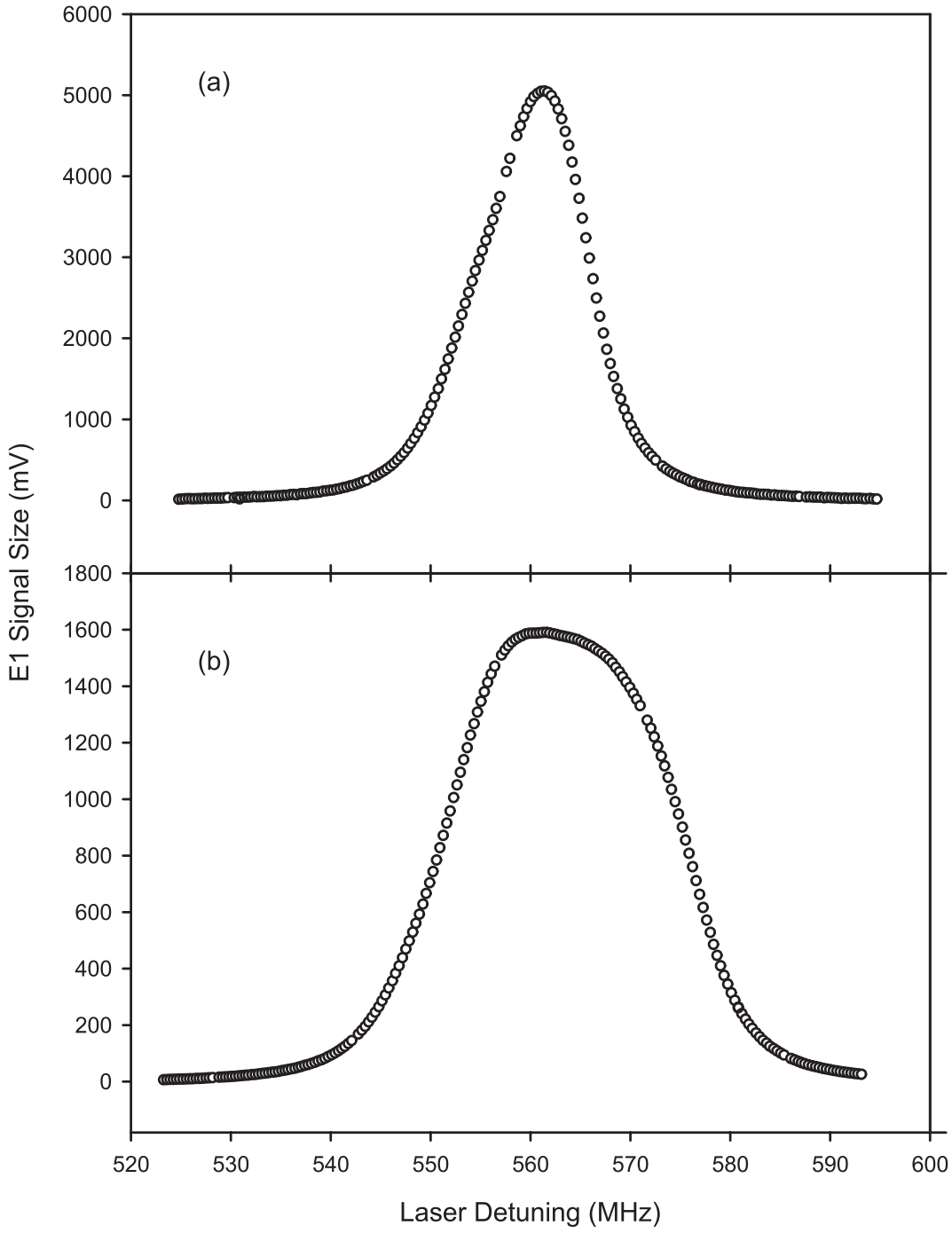

Figure 2.5: Sample scans of the $E1$ transition in (a) small and (b) large magnetic field showing broadening due to the Zeeman effect. The total area of each transition does not change because the Zeeman effect does not change the total transition rate.

CHAPTER 3

APPARATUS

Much of the apparatus used in the experiments described in this thesis was inherited from the previous PNC measurement. Intricate details of the apparatus will not be repeated where they have been presented in the literature or in previous theses, such as for the Pound-Drever-Hall locking scheme that stabilizes the dye laser to the power build-up cavity, or the details of the external cavity diode lasers used in the optical pumping and detection.

The entire apparatus fits onto a large optical table that is isolated from building vibrations by nitrogen-filled legs. A vacuum chamber, which is a large aluminum box measuring about $30 \times 56 \times 66$ cm is bolted to one end of the optical table. Figure 3.1 is a schematic of the apparatus showing the vacuum chamber on the right and the other assorted elements above and to the left. Cesium comes out of an oven in an atomic beam and enters the vacuum chamber. The atomic beam then enters the optical pumping region where the atoms are placed in a single hyperfine state by the hyperfine pumping laser. The atoms then enter the interaction region where there are mutually orthogonal electric, magnetic, and laser fields. The laser field is an intense standing wave with a wavelength of 540 nm. The standing wave is created in a Fabry-Perot etalon with a finesse of 10^5. This etalon increases the power available to drive the $6S \rightarrow 7S$ transition in the cesium atoms and it is called the power build-up cavity (PBC). The 540 nm light is provided by a tunable dye laser that is locked to the PBC using the Pound-Drever-Hall method [32, 33]

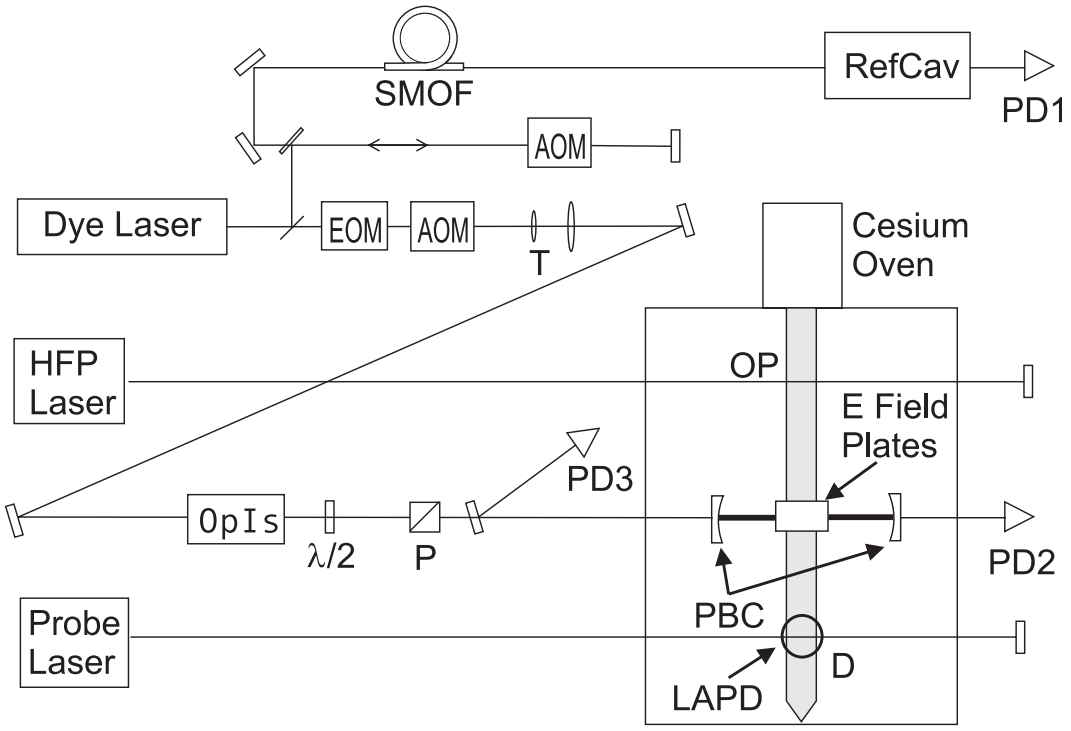

Figure 3.1: The apparatus used in the experiments described in this thesis. SMOF is a single-mode optical fiber, RefCav is the invar reference cavity, AOM is an acousto-optic modulator, EOM is an elecro-optic modulator, T is a mode-matching telescope, HFP is the hyperfine-pumping diode laser, OP is the optical pumping region, OpIs is an optical isolator, $\lambda/2$ is a half-wave plate, P is a polarizer, PBC is the power build-up cavity, D is the detection region, and LAPD is a large area photodiode. PD1, PD2, PD3 are photodiodes.

and the PBC is then locked to a stable reference cavity. The atomic beam finally enters the detection region where atoms that repopulated the depleted hyperfine state after making the $6S \rightarrow 7S$ transition scatter photons from the probe laser. The scattered photons are collected on a large area photodiode, and the photocurrent is proportional to the number of atoms that made the $6S \rightarrow 7S$ transition. A schematic view of just the atomic beam path is shown in Fig. 3.2.

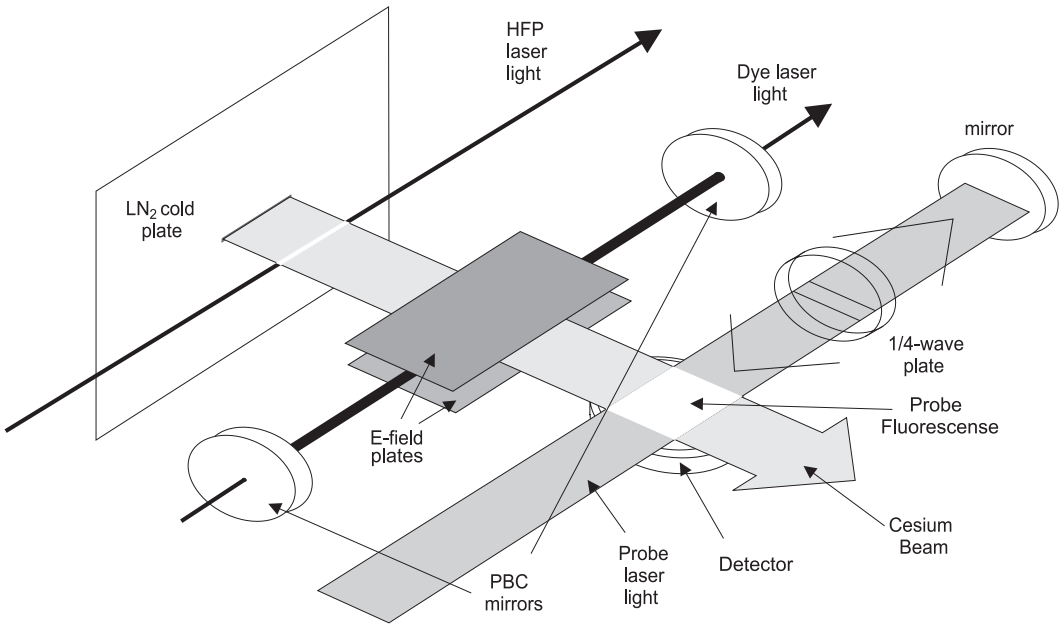

Figure 3.2: Detail of the atomic beam path showing its travel from the liquid nitrogen (LN_2) cooled plate, through the optical pumping region, through the interaction region, and into the detection region.

3.1 The Cesium Oven

The cesium oven used as the source of the atomic beam in these experiments was designed by Carl Wieman and built by Blaine Horner in the JILA instrument shop. It replaces the oven that had been used since the first PNC experiments with cesium were performed by Sarah Gilbert at the University of Michigan [20]. A diagram of the oven is shown in Fig. 3.3. The oven has two sections, the main section in the back of the oven where ampoules of cesium are placed and heated, and the nozzle in the front where the atoms receive their initial collimation.

To load the oven, its pieces are completely assembled except for the rear flange. Then, in a glove box back-filled with argon gas so that the cesium does not react with air, two 10 g cesium ampoules are broken and placed in a small glass "boat." The boat is then placed in the main section of the oven and the rear flange is attached. The oven is then removed from the glove box and attached to the vacuum

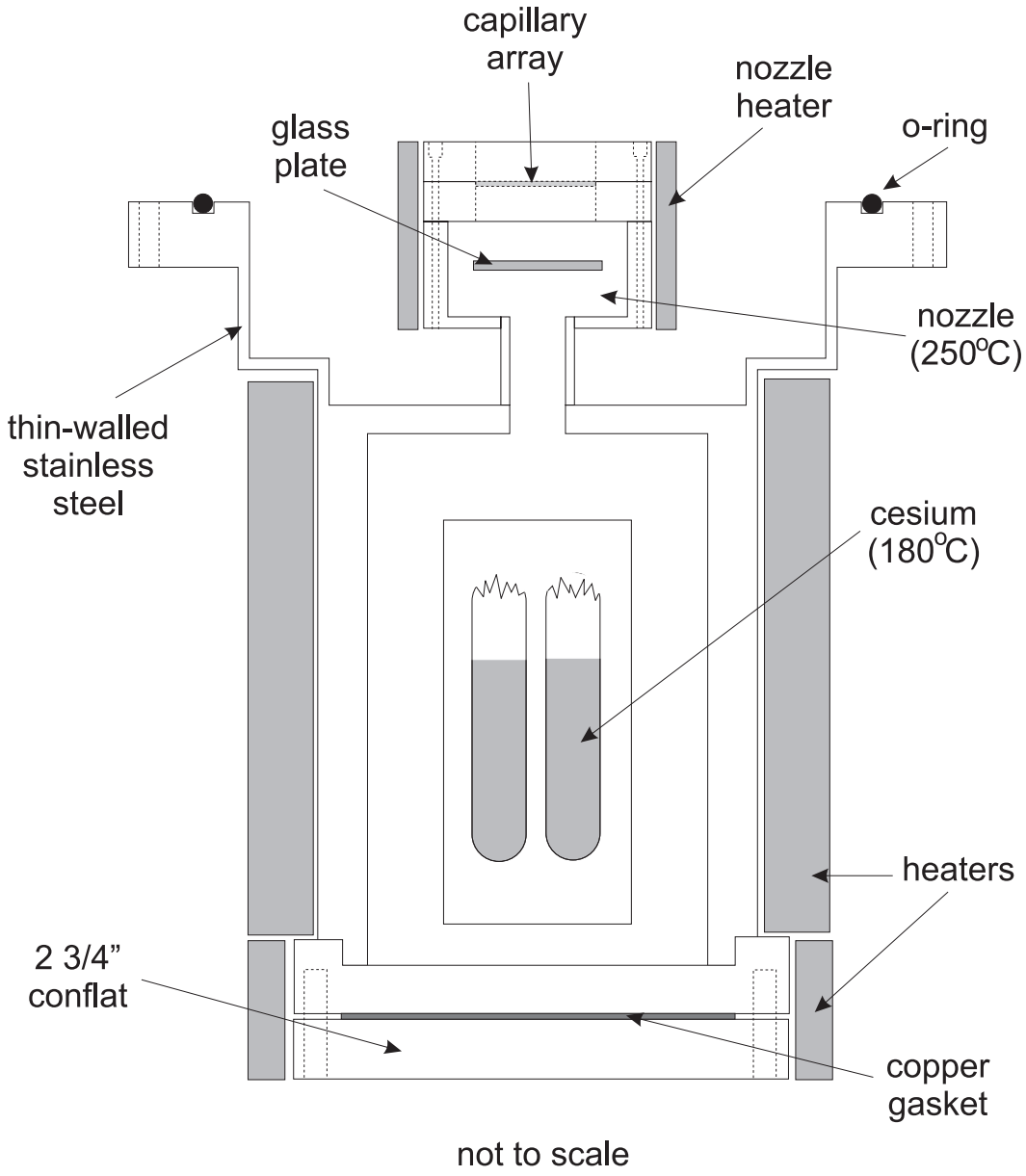

Figure 3.3: A schematic of the cesium oven. Shown are the back section where the cesium ampoules are loaded, the nozzle where the atoms rethermalized to ~250°C, and the assorted heaters, capillary array, etc.

chamber. When the vacuum chamber has been evacuated, the oven gate [34] can be opened. The rear section of the oven is heated by two ceramic heaters fastened around the oven. The entire oven is then wrapped in insulation and temperature

stabilized at around 180°C.

The hot cesium atoms travel from the back of the oven through a small tube to the nozzle which is kept at 250°C to dissociate cesium dimers. A glass plate blocks the direct line-of-sight from the rear of the oven so that the atoms must rethermalize to the nozzle temperature. Once rethermalized, the atoms can leave the nozzle through a glass capillary array that is purchased from Galileo Electo-optics. The arrays are made from blocks of many glass tubes 10 μm in diameter, close packed, and sliced into 0.5 mm thick, 2.54 cm square wafers. Each wafer is then cut into 0.85×2.54 cm rectangles by dragging the corner of a razor blade across its surfaces until enough glass has been scraped away for the array to break cleanly along the scratch. The array covers an opening in the nozzle that is 0.8 cm high and 2.5 cm wide, which gives the initial definition to the atomic beam shape. After leaving the oven, the atomic beam passes through an aperture ∼0.5 cm high × 2.5 cm long in a large copper plate, which is cooled to liquid nitrogen (LN_2) temperature, and then the beam passes through a vertical vane collimator with vane separation of 1 mm. After the vane collimator the beam has a divergence of ∼30 μrad.

It is important to note that capillary arrays are also sold as "microchannel plates", which are made of leaded glass. These plates are often intentionally cut on a bias. That is, the slices are not cut normal to the long direction of the glass tubes. The arrays we received from our supplier varied in the angle at which they were cut from zero to five degrees, despite our specification of zero bias angle. To ensure a high flux in the atomic beam, we measured the bias angle of every array and rejected any arrays that had a bias angle of greater than 0.5°. We were able to use 65% of the arrays delivered to us.

3.2 Optical Pumping Region

Once collimated by the capillary array and the vane collimator, the atomic beam enters the optical pumping (OP) region, which is 10 cm from the oven. Here

the atoms interact with the hyperfine pumping laser (HFP), which is tuned to the $6S_{1/2}$ to $6P_{3/2}$ transition. We use the $F = 3$ to $F' = 4$ transition to deplete the $F = 3$ state when we want to drive transitions from the $6S_{1/2}$ $F = 4$ hyperfine state and we use the $F = 4$ to $F' = 3$ transition to deplete the $F = 4$ when we want to drive transitions from the $6S_{1/2}$ $F = 3$ hyperfine state. These transitions were chosen in previous experiments [22] to minimize the amount of light scattered down the beam that could "undo" the initial optical pumping and to minimize the number of atoms left in the depleted state. The requirements remain the same for the present experiments, so the hyperfine pumping scheme has not been changed.

The hyperfine pumping takes place in a 2.5 G magnetic field, and the polarization of the light is linear and perpendicular the the magnetic field. The light is therefore equal parts σ^+ and σ^- so that atoms should not be preferentially pumped to $m_F < 0$ or $m_F > 0$ states.

The HFP is an external cavity diode laser constructed using an SDL 5401-G1 semiconductor laser locked to a saturated absorption spectrometer as described in Ref. [35]. This laser provides approximately 20 mW/cm^2 of light, which is well above the 1.1 mW/cm^2 saturation intensity of cesium.

In previous experiments, the atomic beam was spin polarized as well as pumped into a single hyperfine state. That "Zeeman pumping", which placed all the atoms into an extreme Zeeman sublevel, is not needed or used for the present experiments.

The result of this mechanical and optical manipulation is a well collimated beam of atoms predominantly (99.95%) in one hyperfine level of the ground state. The horizontal distribution of the atoms is fairly uniform with 64% of the atoms in the center 50% of the beam. The vertical distribution is roughly Gaussian with a height of ~ 0.8 cm. Typical fluxes were 10^{13} atoms/sec, estimated from the shot noise on the signal. (See Section 3.5.3 of Ref. [23] for a discussion of this estimation.)

3.3 Interaction Region

3.3.1 Electric and Magnetic Field Production

In the interaction region the atoms encounter a region of mutually orthogonal electric, magnetic, and laser fields. The electric field is produced by two plates, made either of molybdenum evaporated on glass or of solid molybdenum (depending on the experiment). The plates are centered on both the atomic beam and on the laser field. The magnetic field is produced mainly by a pair of Helmholtz coils, which is also centered on the atomic beam and the laser beam. The laser field is produced by a dye laser coupled into a high-finesse Fabry-Perot etalon as discussed below.

3.3.2 Dye Laser

The $6S \rightarrow 7S$ transition is excited by a 540 nm laser field. For the previous PNC experiment and for the present experiments, the frequency of the laser driving the $6S \rightarrow 7S$ transition must be extremely stable. To achieve the necessary stability, we use the locking scheme shown in Fig. 3.4. The dye laser is a heavily modified Spectra-Physics 380 pumped by a Coherent Innova-90 argon ion laser. Typical ion laser powers range from 3 to 5 W, depending on the age of the dye, and give 200-500 mW of tunable, single-frequency 540 nm light. We use a dye solution made of 1 g/ℓ of Pyromethene 556 dye dissolved in ethylene glycol.

Coarse tuning of the laser is accomplished using an intracavity birefringent tuner, while thick and thin etalons select the longitudinal lasing mode. A Faraday rotator prevents bidirectional lasing. Fine tuning of the laser frequency is performed using three additional intracavity elements. Two galvonometer-mounted glass plates with a range of about 20 GHz control the frequency on a slow time scale (f <2 Hz). A piezoelectric transducer behind one of the cavity mirrors has a range of approximately 300 MHz and controls the frequency at an intermediate time scale (2 Hz< f <2 kHz). Finally, an electro-optic modulator controls the frequency at

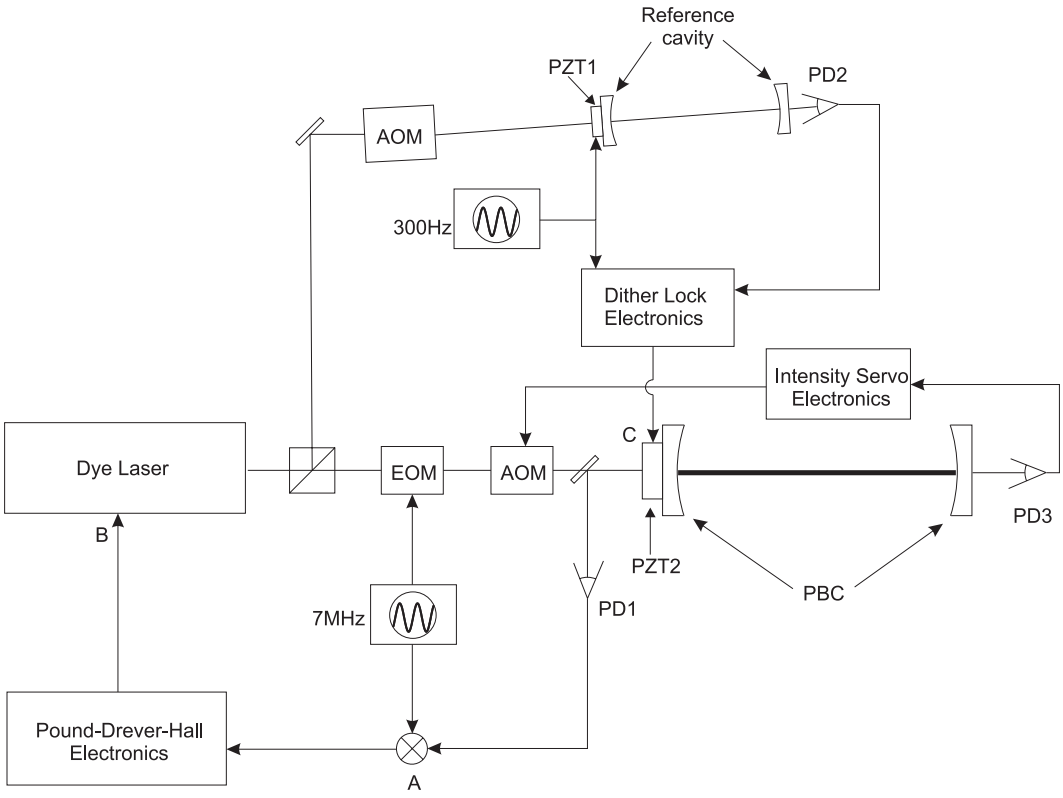

Figure 3.4: A schematic of the dye laser frequency stabilization scheme. The dye laser passes through the EOM where it is phase modulated at 7 MHz and through an AOM before entering the PBC. The light reflected off the PBC is directed to a photodiode (PD1). The signal from PD1 is mixed with the 7 MHz driving signal at A to generate an error signal. The error signal is sent to the Pound-Drever-Hall electronics and then to the dye laser transducers at B. The dye laser is also sent through a second AOM to the reference cavity. The input piezo-electric transducer (PZT) is dithered at 300 Hz. The modulated transmission of the reference cavity is collected on PD2 and sent to the dither lock electronics where an error signal is generated and sent to the PBC PZT at C. The transmission of the PBC collected on PD3 is used to stabilize the intensity of the dye laser.

fast time scales ($\sim$1.3 MHz$> f >$2 kHz).

The gross location of the dye laser frequency is referenced to a group of molecular iodine lines. The proper mode of the laser can be found by scanning the frequency of the laser and observing the fluorescence in an iodine cell. If the laser is far away from the correct frequency it is sometimes necessary to use a portable

scanning double monochromator to set the frequency of the laser near 540 nm.

3.3.3 Fast Frequency Stabilization

The light from the dye laser passes through an electro-optic modulator that puts 7 MHz sidebands on the light. The light then passes through an acousto-optic modulator used to stabilize the laser intensity. The light passes through a telescope for proper mode matching into the etalon. An optical isolator protects the laser from optical feed back, and a half-wave plate and a polarizer are used to control the polarization. The laser light is then incident on the Fabry-Perot etalon.

The frequency of the dye laser is locked to the etalon using the Pound-Drever-Hall method [32]. This method works by looking at the 7 MHz sidebands reflected off the input mirror of the etalon after they are demodulated on a photodiode. When the laser frequency is directly on the resonance of the etalon, the sidebands are phase shifted by equal and opposite amounts. The two sidebands sum together and the demodulated signal size is zero. When the dye laser frequency is slightly detuned from resonance, the sidebands are not phase shifted equally and the demodulated signal is nonzero. Thus, an error signal can be derived from the demodulated sum of the sidebands and used to feed back to the galvos, the piezo and the EOM in the dye laser to keep the frequency of the dye laser on the etalon resonance. When locked to the etalon the dye laser has a line width much less than the 5 kHz resonance width of the etalon.

3.3.4 Power Build-up Cavity

The Fabry-Perot etalon is constructed of two high reflectivity multilayer dielectric mirrors 2.5 cm in diameter. The input mirror has a radius of curvature of 10 m and the output mirror has a radius of curvature of 6 m. The two mirrors are separated by 27 cm, which gives the etalon a free spectral range of $\simeq$550 MHz and a relatively large beam radius of $\omega_0 = 0.41$ mm. Since the etalon geometry is almost

"flat-flat" there is minimal focusing of the beam. In fact, the beam waist only varies by 1% over the length of the etalon.

The two mirrors are of very high quality with the transmittance of each expressed in parts per million rather (ppm) than per cent. The input mirror has $T = 40$ ppm and the output mirror has $T = 13$ ppm. The geometry and the reflectivity combine to give the etalon a finesse of 10^5, and the power inside the etalon is approximately 30,000 times the incident power. For this reason, the etalon is referred to as the power build-up cavity (PBC), and it is one of the main reasons the experiments described in this thesis and the PNC experiment are possible at all. The power density inside the cavity is typically 800 kW/cm^2, which makes observation of the very weak $6S \rightarrow 7S$ transitions easy.

The mechanical design of the PBC is shown in Fig. 3.5. The two mirrors are mounted on aluminum brackets using silicone rubber to minimize stress-induced birefringence. The brackets are then mounted in optical mounts. The input mirror is also mounted to a tube piezo-electric transducer (piezo) to allow for tuning of the

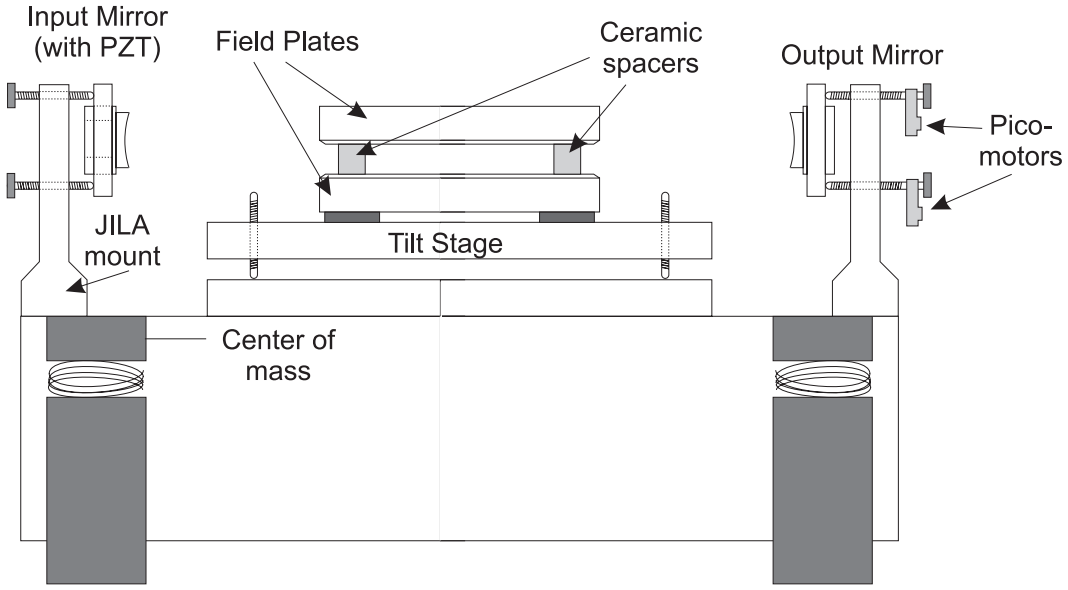

Figure 3.5: Detailed mechanical design of the PBC.

resonant frequency of the PBC. The two mounts are then bolted to a large granite block, which is very rigid and provides a large inertial mass. The granite block is suspended in the plane of its center of mass by four beryllium-copper springs, which are damped by a small amount of sorbothane rubber. This arrangement is to minimize tilts between the cavity and the optical table and to retain a gentle suspension to isolate the cavity from vibration and shock. Since temperature variations will cause frequency shifts, both mirror mounts are temperature stabilized.

3.3.5 Slow Frequency Stabilization

While the line width of the dye laser is less than 5 kHz on a short time scale when locked to just the PBC, the PBC does bounce slightly, and the piezo on the input mirror can creep. Therefore the longer term stability can be unacceptably poor. In order to stabilize the frequency of the dye laser on long time scales, the PBC is locked to a stable reference cavity. This reference cavity was locked to the peak of the $6S \rightarrow 7S$ transition for the PNC experiment, and was only used to stabilize the PBC on a long time scale. However, for the experiments described in this thesis the cavity must serve as a frequency reference by itself.

To improve the stability of the reference cavity, which is already constructed of Invar, the nearly confocal cavity was hermetically sealed, and a second stage of temperature stabilization was added. In addition, light is coupled into a single mode optical fiber before going into the reference cavity because motion of the beam incident upon the reference cavity can cause a change in the point at which the PBC locks to the reference cavity. (See Chapter 4.)

One of the mirrors of the reference cavity is mounted on a piezo. The voltage on this piezo is dithered at 300 Hz, and the transmission through the cavity is monitored on a lock-in amplifier. The signal from the lock-in amplifier provides an error signal that is fed back to the PBC piezo, and thus the PBC is kept locked to the reference cavity.

3.4 Detection Region

After the atoms interact with the frequency-stabilized dye laser light and are excited to the $7S$ state they relax back to the $6S$ state via transitions to the $6P_{1/2}$ and $6P_{3/2}$ states and then to the ground state. The atoms decay to both hyperfine states of the ground state with 75% of the atoms decaying to the state with the same quantum number F to which they were excited That is, of the $7S_{1/2}$ $F' = 4$ atoms, 75% decay to the $6S_{1/2}$ $F = 4$ and 25% decay to the $6S_{1/2}$ $F = 3$. We then detect the number of atoms that made the $6S \rightarrow 7S$ transition by "counting" the number of atoms that are in the initially depleted hyperfine state.

To detect atoms that relax to the $F = 4$ hyperfine state we lock another external cavity diode laser–the probe laser [23, 35]–to the $6S_{1/2}$ $F = 4$ to $6P_{3/2}$ $F' = 5$ transition. Since the dipole selection rule requires $\Delta F = 0, \pm 1$, atoms driven to the $6P_{3/2}$ $F' = 5$ state can only relax back to the $6S_{1/2}$ $F = 4$ (since there are no $F = 5$ or 6 states in the ground state) where they are available to be excited again. We collect roughly 200 scattered photons per atom on this "cycling" transition on a large area photodiode located directly beneath the region where the atomic beam and probe beam intersect. We place a gold mirror above the atomic beam to reflect photons emitted upward back into the photodiode. In order to maximize the number of photons an individual atom can scatter we use two cylindrical telescopes to widen the probe laser beam to about 2.5 cm in width and 1 cm in height.

The situation is a little different for atoms that are excited out of the $F = 4$ hyperfine state. The appropriate cycling transition here is the $6S_{1/2}$ $F = 3$ to $6P_{3/2}$ $F' = 2$. This transition suffers from the problem that it is similar to a "lambda" transition where there are fewer excited state levels than there are ground state levels. Atoms that are excited can eventually evolve into a superposition of ground states are no longer resonant with the excitation recitation; they "go dark" [36, 37, 38].

In order to prevent the atoms from "going dark", the probe beam is linearly

polarized and reflected back upon itself, passing twice through a quarter wave plate. The result is that the polarization of the reflected light is rotated by 90° forming a configuration known as "lin-perp-lin" [39], which has a spatial variation of the polarization. At one point in space the light is linearly polarized, then $\lambda/8$ away the light is σ^+ polarized, then another $\lambda/8$ away the light is linearly polarized, then σ^-, and so on. In addition, a magnetic field gradient is applied in the detection region so that as an atom moves down the atomic beam it is in a different magnetic field each time it is excited to the $6P_{3/2}$ state. In this way the atoms never encounter the right conditions to "go dark." The scheme is not perfect, however, and the number of photons scattered on the $F = 3$ to $F' = 2$ transition is only 45% of the number scattered on the $F = 4$ to $F' = 5$ transition

3.5 Data Acquisition

All of the work presented in this thesis is basic spectroscopy. That is, the frequency of the dye laser is scanned across the $6S \rightarrow 7S$ transition, and the transition rate as a function of laser frequency is recorded. A computer controls the data acquisition in the following manner, schematically illustrated in Fig. 3.6.

The computer sends a signal to a digital-to-analog converter that provides a control voltage to change the frequency of the dye laser. For low-precision measurements of the line shape (Section 7.1) the computer changes the voltage on the reference cavity piezo, thus changing the reference frequency. For the dc Stark shift measurement (Chapter 4) and for the tensor transition polarizability measurement (Chapter 5) the computer controls the frequency of an AOM that shifts the frequency of the light coupled into the reference cavity. The frequency of the dye laser must change to account for the shift.

After a fixed amount of time after the dye laser control voltage changes (to let transients settle, etc.), the computer triggers two gated integrators. These integrators integrate the signal from the probe photodiode and the voltage controlling

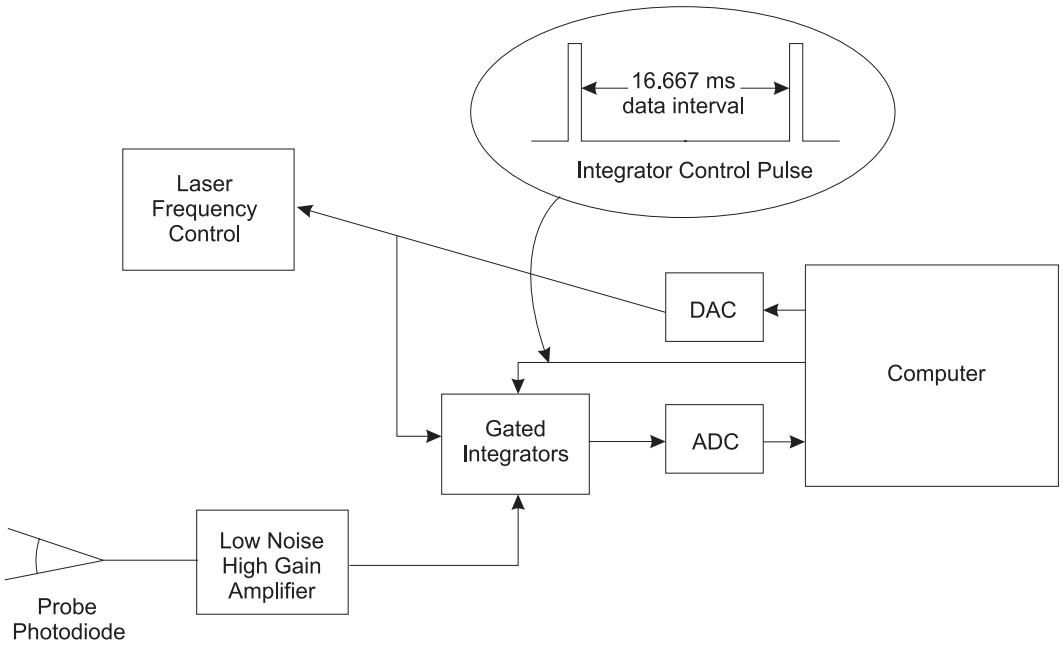

Figure 3.6: A schematic of the data acquisition system. The computer controls the laser frequency through a digital-to-analog converter (DAC). As the laser scans over the transition, the scattered light is collected on the probe photodiode (PPD) and amplified. The voltage to the frequency control and the signal from the PPD are integrated in 16.667 ms intervals, converted on the analog-to-digital converter (ADC) and stored on disk.

the laser frequency. The length of the integration interval, which is also controlled by the computer, is 16.667 ms. This particular interval is chosen to average away any 60 Hz noise. The two voltages are then converted to a digital signal by an analog-to-digital converter and are stored on disk. As the control voltage is scanned, we generate a transition rate versus voltage plot that, with suitable calibration, may be converted to a transition rate versus frequency plot similar to that shown in Fig. 3.7. Plots like this make up the data for all of the experiments described in this thesis.

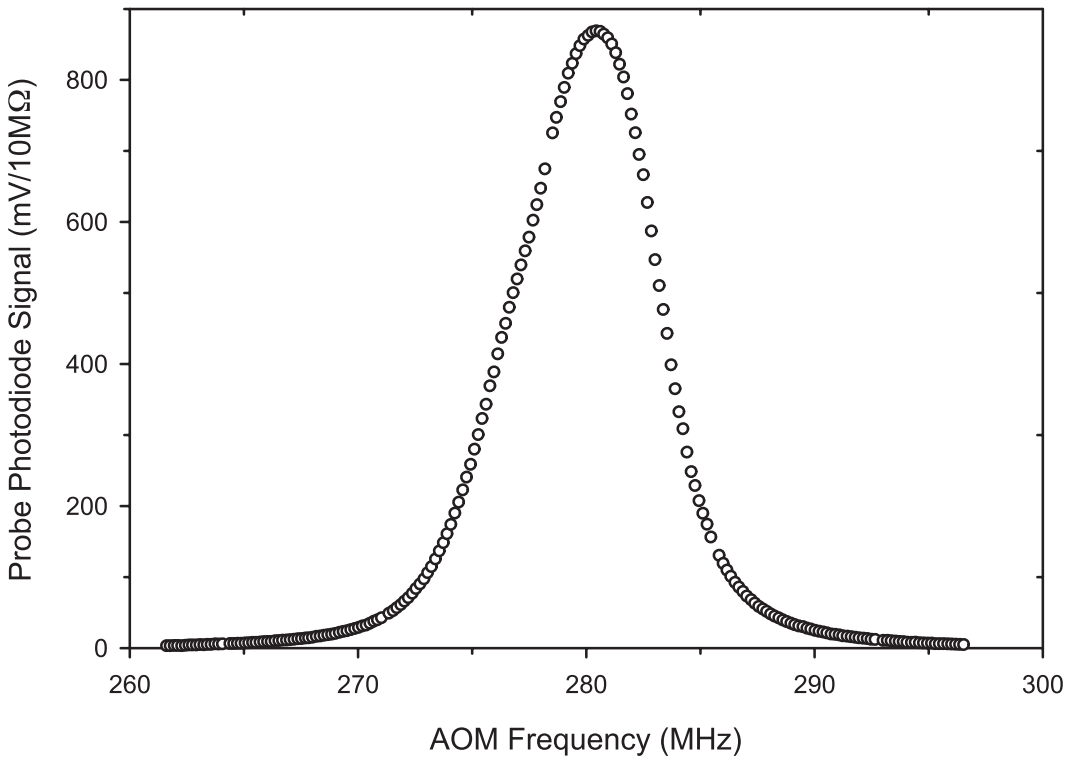

Figure 3.7: A sample of the data taken for the measurements in this thesis. The x-axis is the frequency of the AOM that shifts the frequency of the dye laser before it is incident on the reference cavity, and the y-axis is the signal from the probe photodiode.

CHAPTER 4

MEASURING THE STARK SHIFT OF THE $6S \rightarrow 7S$ TRANSITION

As discussed in Chapter 1, a test of the standard model using measurements of PNC in atomic cesium requires an accurate and precise calculation of atomic structure using atomic theory. The most objective way to test the accuracy of the theory is to compare its predictions with measurements of various atomic properties.

There are many measurements of the properties of cesium, including the lifetimes of the $6P$ states [40], and the hyperfine structure constants of the $6S$, $7S$ [41], $6P_{1/2}$, and $7P_{1/2}$ [42] states. All of these measurements agree with the predictions of Blundell *et al.* [14, 43, 44, 45] and Dzuba *et al.* [46, 15, 47, 48] to better than 1%. There was a notable exception to this good agreement in the measurement of the $6S \rightarrow 7S$ dc Stark shift, where the difference between the theory and the experiment [49] was 2%.

This chapter presents the theory of the dc Stark effect along with the details of our experiment that re-measures the dc Stark shift of the $6S \rightarrow 7S$ transition and eliminates the previous discrepancy. The details of the experiment include discussions of the requirement of a stable reference frequency and its implications for our data taking method and frequency stabilization schemes, the production and measurement of the electric field causing the Stark effect, and the determination of the dc Stark shift from our data. A presentation of our results concludes the chapter.

4.1 Theory of the dc Stark Effect

The theory of the dc Stark effect, which gives rise to the dc Stark shift, is discussed in detail in Ref. [50]. The full theory will not be repeated here. Instead, an outline of the calculation following that in Ref. [51] is presented. The interaction of an atom with a dc electric field $\vec{E}$ can be described by the Hamiltonian

$$H_{\text{Stark}} = -e \sum_i \vec{r_i} \cdot \vec{E}, \tag{4.1}$$

where e is the electric charge, and $\vec{r_i}$ is the vector from the nucleus to the ith electron. In Ref. [50] it is shown that this Hamiltonian can be broken into two components: $H_{\text{Stark}} = H_{\text{scalar}} + H_{\text{tensor}}$. The term H_{scalar} depends on only the magnitude of the electric field, while the term H_{tensor} depends on the field's direction as well as its magnitude.

The Stark Hamiltonian shifts energy levels as well as gives rise to the mixing discussed in Section 2.3.2, which permits the Stark-induced electric dipole transition. If the hyperfine structure is neglected, the energy shift is given by

$$\Delta\varepsilon(n, J, m_J) = -\frac{1}{2}\alpha_0 E^2 - \frac{1}{2}\alpha_2 \frac{3m_J^2 - J(J+1)}{J(2J-1)} \left(\frac{3E_z^2 - E^2}{2} \right), \tag{4.2}$$

where α_0 is the scalar polarization due to H_{scalar} and α_2 is the tensor polarization due to H_{tensor}. These two polarizations are given by

$$\alpha_0 = -\frac{2}{3} \sum_{n'J'} \frac{| \langle nJ \mid p \mid n'J' \rangle |^2}{(2J+1)(E_{nJ} - E_{n'J'})} \tag{4.3}$$

and

$$\alpha_2 = 2\left[\frac{10J(2J-1)}{3(2J+3)(J+1)(2J+1)}\right]^{1/2} \times \sum_{n'J'} \frac{|\langle nJ \mid p \mid n'J'\rangle|^2}{E_{nJ}-E_{n'J'}}(-1)^{J+J'+1}\left\{\begin{array}{ccc} J & J' & 1 \\ 1 & 2 & J \end{array}\right\}, \tag{4.4}$$

where E_{nJ} is the energy of the $|nJ\rangle$ state.

In this approximation it is clear that the tensor polarizability vanishes for $J = 1/2$. However, when higher orders of the theory are considered there is a contribution to α_2 from the combination of the off-diagonal matrix element of H_{tensor} between $J = 1/2$ and $J = 3/2$ states and the matrix element of the hyperfine structure operator between the same states. For the $L = 0$ states we are considering, this mechanism vanishes, but there are still tiny contributions due to the spin-dipolar part of the magnetic hyperfine structure and the quadrupole interaction [50]. In cesium, the tensor polarizability has been measured to be $\alpha_2 = -0.1372(79) \times 10^{-7}$ Hz$(\text{V/cm})^{-2}$ [52]. When compared with the scalar polarizability $\alpha_0 \sim 0.7$ Hz $(\text{V/cm})^{-2}$ it is clear that the tensor polarizability is negligible. Therefore, we are only concerned with the scalar part of the dc Stark shift, which is independent of hyperfine level for energy shifts that are small compared to the fine structure splitting [53].

The energy shift due to the dc Stark shift of an $|nS_{1/2}\rangle$ state is given simply by

$$\Delta\varepsilon_{nS} = -\frac{1}{2}\alpha_{nS}E^2, \tag{4.5}$$

where α_{nS} is the scalar polarizability. The dc Stark shift of the $6S \rightarrow 7S$ transition is given by

$$\nu_{\text{Stark}} = -\frac{\alpha_{7S}-\alpha_{6S}}{4\pi}E^2 = kE^2. \tag{4.6}$$

To determine the constant k we scan across the $6S \rightarrow 7S$ transition at high and low electric fields, measure the line centers of the two scans, and calculate the frequency separation, $\Delta\nu_{\text{Stark}}$, of the two centers. Sample scans are shown in Fig. 4.1. The

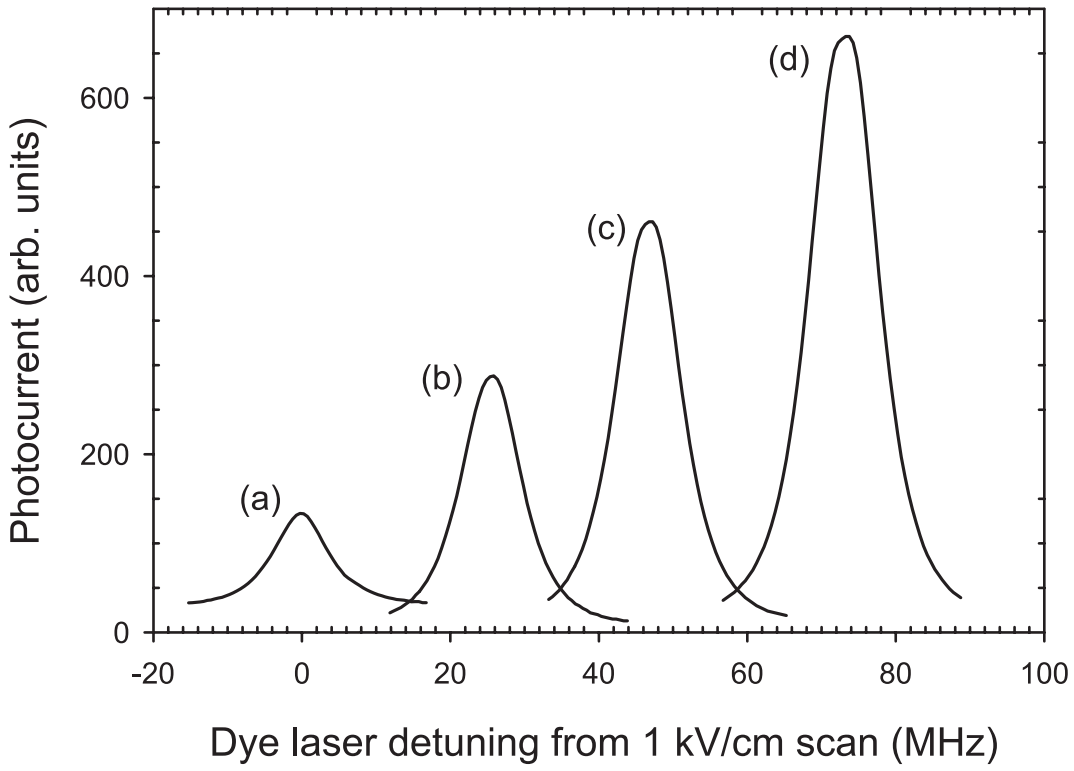

Figure 4.1: Four different scans of the 6S→7S transition with dc electric fields of (a) 1 kV/cm, (b) 6 kV/cm, (c) 8 kV/cm, and (d) 10 kV/cm.

value of k is then given by

$$k = \frac{\Delta\nu_{\mathrm{Stark}}}{E^2_{\mathrm{high}} - E^2_{\mathrm{low}}}. \tag{4.7}$$

Because the value of k is independent of hyperfine level, we use the transition with the highest signal-to-noise ratio: the $F = 3$ to $F' = 3$ transition.

4.2 Details of the Experiment

4.2.1 Data Scans and Frequency Drift

The major challenge in this experiment is determining the frequency separation of two scans to 0.1%. In order to make such a determination we must have a stable reference frequency. We use use the reference cavity described in Section 3.3.5, which is the same cavity discussed in section 5.1.3 of Ref. [23]. In order to make

the cavity stable enough for the present experiment we have hermetically sealed the cavity and added a second stage of temperature stabilization. In addition, we use a simple peak locking scheme rather than the Pound-Drever-Hall locking scheme because of the latter's suceptibility to electronic offsets. The final frequency drift rate of the reference cavity averaged 0.5 MHz/min with a maximum observed drift of 0.8 MHz/min.

As described in Section 3.5, a computer controls the data acquisition. For this experiment the computer uses GPIB commands to control a Hewlett-Packard frequency synthesizer. The output from the synthesizer drives an acousto-optic modulator (AOM), which shifts the frequency of the dye laser light incident on the reference cavity. Since the dye laser is locked to the PBC, and the PBC is locked to the reference cavity, changing the AOM frequency causes the dye laser frequency to change by twice that amount. (Twice because the AOM is double passed. See the next section.)

The scans over the $6S \rightarrow 7S$ transition are 75 MHz wide and take approximately 8 seconds. The frequency separation between a scan at E=1 kV/cm and a scan at E=10 kV/cm is $\sim$70 MHz. Therefore, the maximum allowable drift rate of the reference cavity is 0.5 MHz/min. Even smaller drift rates are required for lower electric fields. For all the data used in the final analysis we measured the drift before and after the measurement to ensure the rate was at an acceptable level.

4.2.2 Coupling Light into the Reference Cavity

The AOM is used to shift the frequency of the dye laser light incident on the reference cavity. Because the angle through which the light is diffracted by the AOM changes as the frequency of the AOM is changed, the AOM is "double-passed" as shown in Fig. 4.2. Double passing the light in the AOM works in the following way.

First we examine the horizontal motion by looking at the top view in

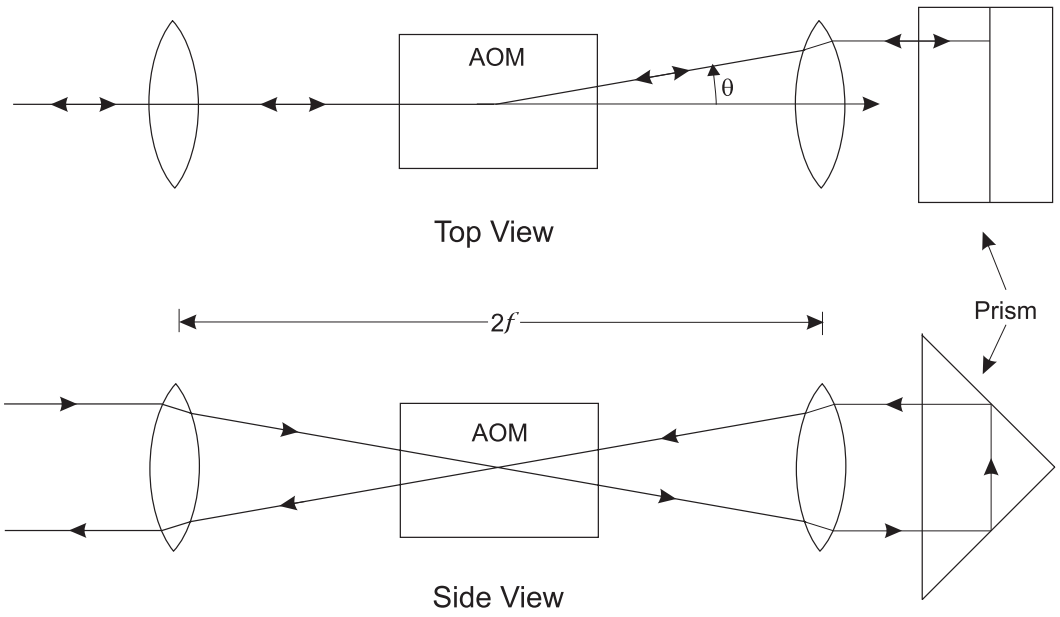

Figure 4.2: Top and side views of light "double-passed" through an AOM. Double passing the light eliminates most of the angular motion associated with a change in AOM frequency.

Fig. 4.2. The light to be passed through the AOM is centered horizontally on a lens that has a focal length f. The center of the AOM transducer is placed at the focal point of the lens, and the action of the AOM diffracts the light at some angle θ. The light then travels to another lens placed a distance f away from the AOM. This second lens also has a focal length f. The second lens bends the light back parallel to the initial direction of the laser beam. The beam is then retro-reflected off a prism and retraces its path back through the lenses and the AOM. As the frequency of the AOM changes, so does the angle θ. However, because of the positioning of the second lens, the laser beam is always normal to the prism and always gets retro-reflected. Therefore, the horizontal motion of the beam has been nearly eliminated.

A consequence of removing the horizontal motion of the laser beam is that the reflected beam travels back upon itself. This makes it difficult to use the light that has passed through the AOM. To describe the solution to this problem, we use

the side view in Fig. 4.2. The light incident on the lens-AOM system comes in above the center of the first lens. The first lens bends the light down through the AOM, causing the light to hit the second lens below its center. The second lens then brings the light back parallel to the initial direction and the prism reflects the light back with a vertical shift, and the light passes back through the second lens above its center. The second lens repeats the action of the first by bending the light down through the AOM and then low on the first lens. The beam is then bent back to parallel by the first lens. The result of the whole system is that the beam coming out of the lens-AOM system is lower than the one going in, but the horizontal motion does not change with changing AOM frequency. The lower beam is easily directed to the reference cavity.

The double-passed AOM system does not eliminate all the motion; the angular displacement with a change in frequency of $\sim$40 MHz is $\sim$0.3 mrad, compared with the usual 260 mrad. This is sufficient to keep the laser beam from moving off the reference cavity. It is not sufficient for measuring 70 MHz separations to 0.1%, however. The reason is as follows.

The reference cavity was constructed to be a confocal cavity. However, the limitations of experimental science preclude us from building a perfectly confocal cavity, so the cavity is only **nearly** confocal. As a result, adjacent modes are not perfectly degenerate. The transmission through the reference cavity of three such modes, (a), (b), and (c), into which the light might couple is shown in Fig. 4.3. As the light incident on the reference cavity moves, the coupling into each mode changes. Figure 4.4(d) shows the results when 60% of the light is coupled into mode (a), 30% is coupled into mode (b), and 10% is coupled into mode (c). Figure 4.4(e) shows the results when the fractions coupled into mode (a) and mode (c) are reversed. Because we use a locking scheme that locks the laser frequency to the frequency of the maximum transmission of the reference cavity, the lock point of the laser frequency will change as the coupling changes. To eliminate this problem from beam

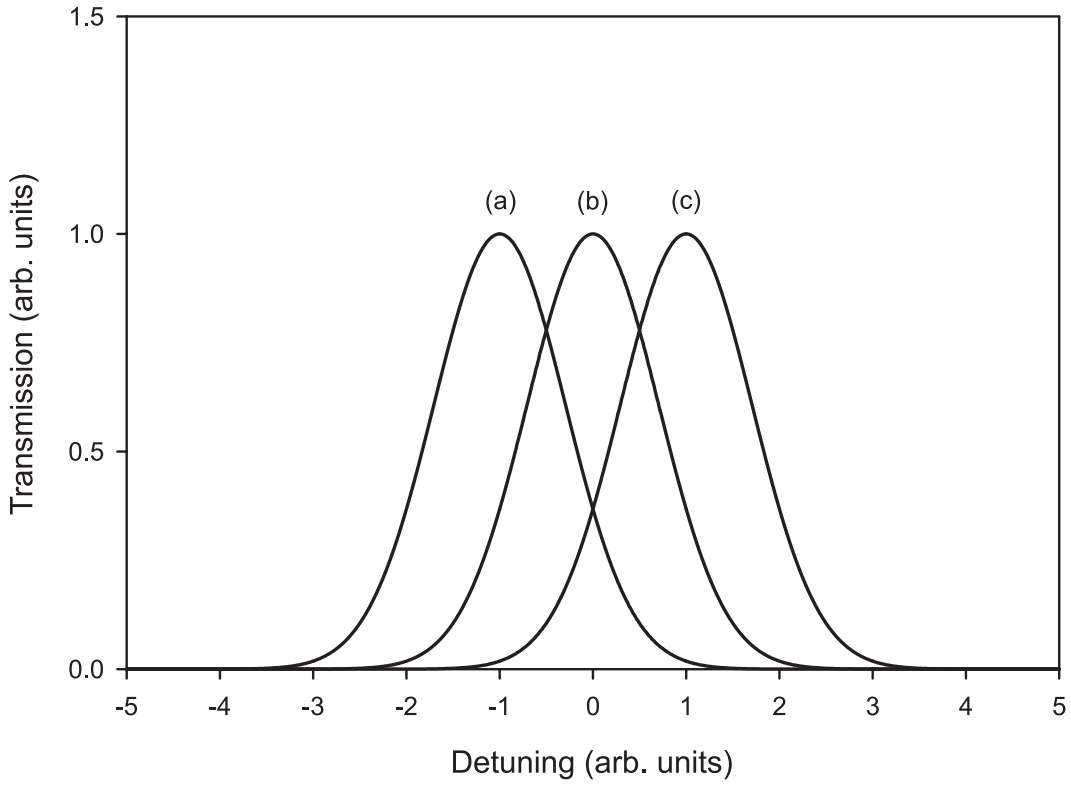

Figure 4.3: Transmission versus frequency of three nearly degenerate modes of the reference cavity.

motion on the reference cavity, we couple the light from the double-passed AOM into one end of a 0.3 m length of single mode optical fiber. The other end of the fiber is fixed to an optical mount. By using this scheme, the **intensity** of the light incident on the reference cavity changes by up to 20% because the light from the AOM moves on the face of the fiber, which changes the coupling efficiency into the fiber. However, the output end of the fiber remains fixed, and thus the light into the reference cavity remains motionless. The variations in intensity transmitted through the fiber do not affect the lock point of the dye laser.

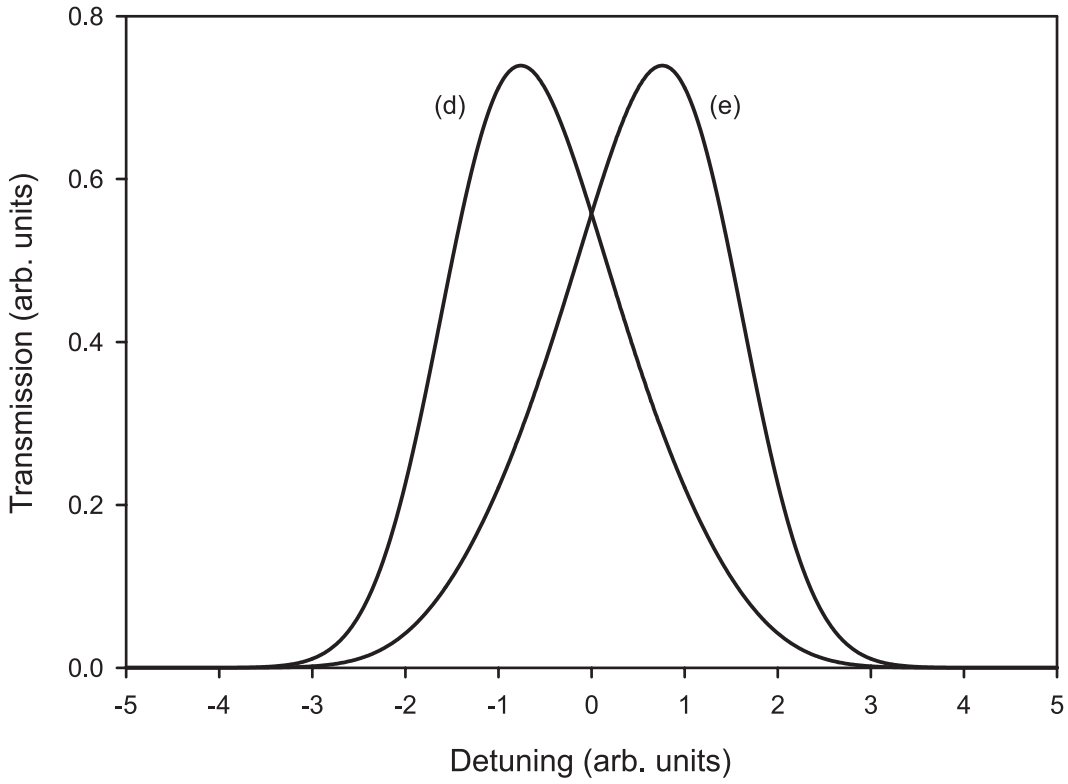

Figure 4.4: Total transmission through the reference cavity versus frequency. The transmission when 60% of the light is coupled into mode (a) (from Fig. 4.3), 30% of the light is coupled into mode (b), and 10% of the light is coupled into mode (c). The transmission shown in (e) is when the fraction of light coupled into modes (a) and (c) has been reversed.

4.2.3 Production and Measurement of the Electric Field

The electric field plates used in this experiment are different from those used in the PNC measurement and in the measurement of β. The plates are $2 \times 5 \times 0.5$ cm blocks of molybdenum mounted in a plexiglas bracket. The plates are separated by 0.48994(25) cm. They were made smaller than the plates used in the PNC experiment to keep them as far away from other conducting surfaces as possible in order to handle safely the 5 kV applied across the plates. In addition, all the corners and sharp edges on the plates are rounded or smoothed to prevent arcing.

The voltage on the plates is measured with a high-voltage probe that was

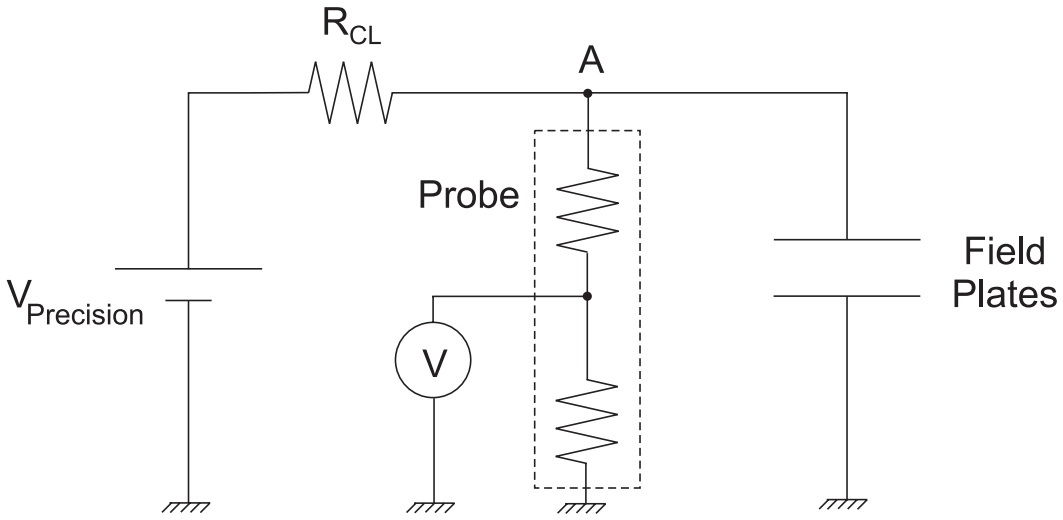

Figure 4.5: The voltage divider measurement of E at point A for the dc Stark shift measurement. $V_{precision}$ is the high-voltage source, R_{CL} is a current-limiting resistor, and the two resistors and the dashed box are the high-voltage probe. The experiment is always run with the probe in place because the probe and R_{CL} in series make a second voltage divider that changes the voltage at A.

calibrated with a NIST-traceable voltage source in the JILA electronics shop. The probe divides the voltage applied to the plates by 901.52(5). The method for measuring the voltage is shown in Fig. 4.5. It is important to note that when the high-voltage probe is in place it makes a voltage divider with the current-limiting resistor R_{CL}. This divider causes a voltage drop across R_{CL}. If the experiment is performed with the probe removed the voltage on the plates will be different than the voltage that was measured. Because of this difference, the probe is left connected at all times.

4.3 Determination of the dc Stark Shift

4.3.1 Determination of Line Centers

To obtain the transition rate versus frequency plots for this experiment, we lock the laser and the cavities with the AOM frequency set in the middle of its

range. We then change the voltage on the reference cavity piezo to tune the dye laser frequency to the peak of the $6S \rightarrow 7S$ transition*. The computer then quickly sweeps the voltage controlling the AOM frequency to a point below the $6S \rightarrow 7S$ transition and then sweeps the voltage across the transition in small steps, taking a 16.667 ms long data point at each step.

An accurate determination of the center of each scan is critical to the success of this measurement. Because the ac Stark effect can cause broadening of the line shape and large frequency shifts of its effective center [$\sim$21 MHz/(MW/cm^2)] [30] we keep the intensity inside the PBC as low as possible. The intensity in this experiment is 200 W compared with the intensity of 4 kW typical for the PNC experiment. Our intensity reduces the ac Stark shift to 0.84 MHz. This is much larger than the acceptable uncertainty on our measurement of high- and low-E peak separations. However, the ac Stark shift does not depend on the dc electric field. Therefore, this small ac Stark shift does not affect the accuracy of our measurement.

Because of the asymmetry introduced by the ac Stark shift, it is impossible to fit our line shapes to a simple function. Therefore it is not straight forward to determine the line center. The line shape does not change significantly with E, however, so it is possible to determine an **effective** line center for each scan. The "center" of a line is found by taking the two frequencies at which the probe signal is $n/10$ times its peak value and averaging the pair of frequencies for each $n = 1, 2, \ldots, 9$. The effective center is then the average of these nine values. We test the reproducibility of this method by changing slightly the value of the probe signal at which we determine the two frequencies. For example, instead of taking the values at $n/10$, we can take the values at $1.01 \times n/10$. The reproducibility of finding line centers in this manner is 0.02 MHz.

We find that saturation of the $6S \rightarrow 7S$ transition can cause small shifts in

*Of course, we only adjust the reference cavity before the initial scan. For successive scans the cavity serves as the frequency reference.

the effective line center. Scans over the transition with and without saturation are shown in Fig. 4.6. As can be seen in Eq. (2.27), the $6S \rightarrow 7S$ "α" transition rate has two terms. To avoid an error from saturation we rotate the linear light until ϵ_x is roughly 10% smaller than its smallest value at which we can measure a shift of the line center. Therefore, there is no effect on our determinations of the line centers from saturation. The small β terms are larger as a result, but the relative size of the "α" rate to the "β" rate is $(\alpha/\beta)^2 = 98.1$, so the small β terms are still unimportant*. In the end we determine the line center to approximately 2 parts in 1000.

4.3.2 Determination of Frequency Separation of two Electric Fields

If the reference cavity were perfectly stable, determining the frequency separation between a low-E scan and a high-E scan would be trivial. However, the reference cavity has a nonzero drift rate as previously discussed. As can be seen in Fig. 4.7, the drift can be nonlinear, even reversing direction from time to time. Taking several scans at high and low electric fields in succession is sufficient to eliminate a linear drift. To account for the nonlinear drift we use a standard least squares technique [54] to fit the centers of 16 scans, which alternate between high and low E, to a third order polynomial plus a constant. The extracted constant is the dc Stark shift. Our final fractional uncertainty in $\Delta\nu_{\mathrm{Stark}}$, which is dominated by the uncertainty in the determination of the line centers, is 0.04% for each ten scan set.

4.4 Results

Once we can determine the separation between two scans taken with different electric fields we can, in principle, determine the value of k. However, a more precise determination can be made if we extract k from the fit to data taken at

*Even if the "β" terms **do** become appreciable, their contribution to the line shape scales the same way the "α" contribution does. Therefore, the frequency shift between effective line centers will be the same as in the absence of the "β" transition.

several different values of the high field. Determinations of k from pairs of fields (eg. 1 kV/cm and 10 kV/cm) are shown in Fig. 4.8. The weighted average of the 14 scans is 0.72618(19) Hz $(\mathrm{V/cm})^{-2}$. The fit of the data to $\Delta\nu_{\mathrm{Stark}} = kE^2$, along with a plot of the residuals is shown in Fig. 4.9. The slope of the line fitting the data is $k = 0.72620(13)$ Hz $(\mathrm{V/cm})^{-2}$. The reduced χ^2's for the fit and the weighted average both indicate a 60% probability that the data are from a random distribution. The contributions to the uncertainty in our final result for k are 0.1% from the measurement of the field plate separation*, 0.04% from the determinations of $\Delta\nu_{\mathrm{Stark}}$, and 0.01% from the measurement of the applied voltage. This yields a total fractional uncertainty of 0.11%. Our final result is

$$k = 0.7262(8)\ \mathrm{Hz(V/cm)}^{-2}, \tag{4.8}$$

which disagrees with the previous result of 0.7103(24) Hz $(\mathrm{V/cm})^{-2}$ [49], but is in excellent agreement with theoretical prediction $k = 0.7257$ Hz $(\mathrm{V/cm})^{-2}$ of Blundell *et al.* [14], and is within 0.3% of the prediction $k = 0.7237$ Hz $(\mathrm{V/cm})^{-2}$ of Dzuba *et al.* [55]. These data are shown in Fig. 4.10. The difference in polarizabilities of the two states, $\alpha_{7S} - \alpha_{6S}$ can be extracted from these numbers. In atomic units, our result is $\alpha_{7S} - \alpha_{6S} = 5837(6)$ compared with the predictions of Blundell *et al.* ($\alpha_{7S} - \alpha_{6S} = 5833$) and Dzuba *et al.* ($\alpha_{7S} - \alpha_{6S} = 5817$). We have attempted to determine the source of the disagreement between the present work and that of Watts *et al.* [49]. However, Watts, who carried out the primary data analysis, is deceased and the records of his analysis are no longer available.

*We measure the separation of the plates by using a high-precision height-micrometer and a dial indicator to measure the difference in each plate's height above a flat granite surface. A more precise measurement could be made optically, but the constraints of the experiment prevent us from constructing the plates out of materials that would allow such a measurement. (See Ref. [13], Section 5.2.)

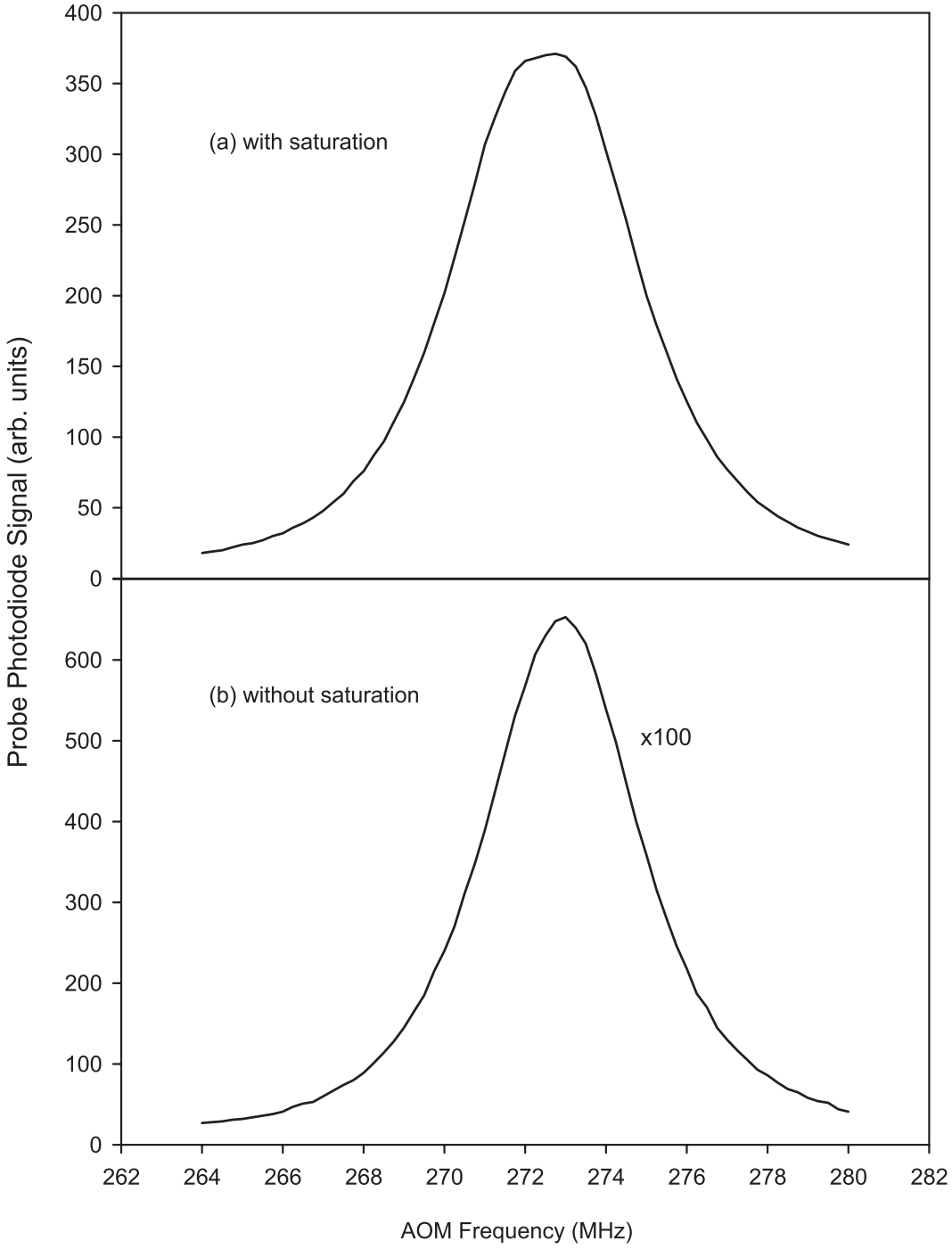

Figure 4.6: Scans over the $6S \rightarrow 7S$ transition (a) with and (b) without saturation. In (a) the electric field is 9 kV/cm and in (b) the electric field is 1 kV/cm. Note that in (b) the signal has been increased by a factor of 100.

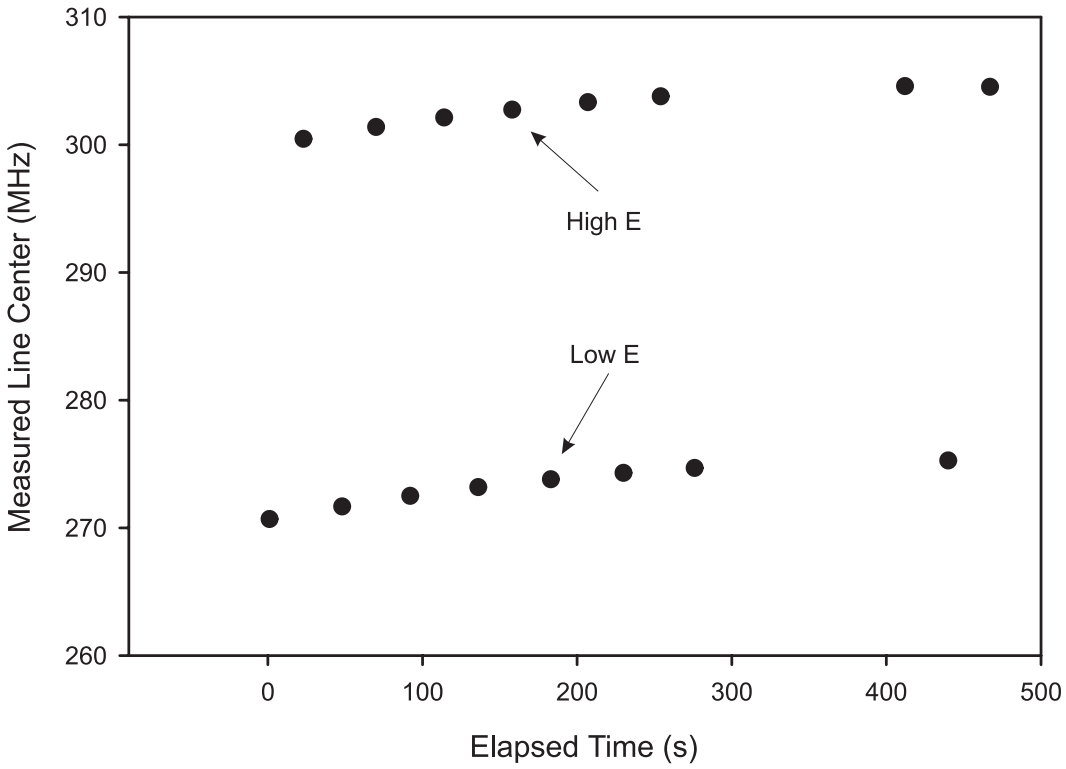

Figure 4.7: Typical data from a data "set" showing the drift of the reference cavity. The separation between the data points is the dc Stark shift.

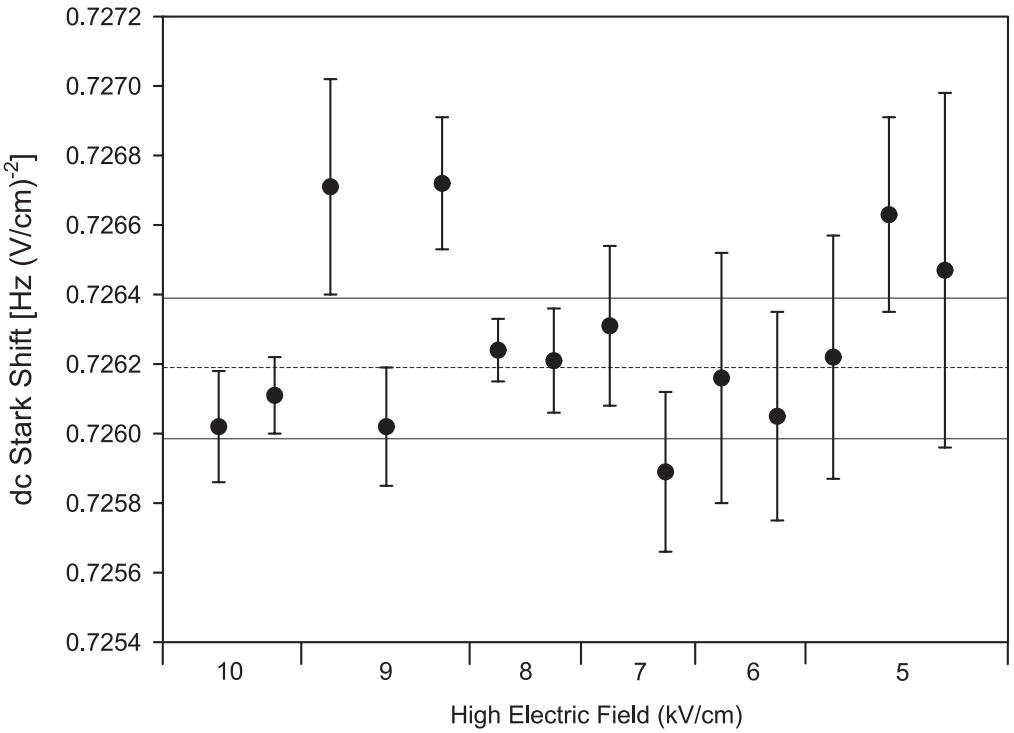

Figure 4.8: Determinations of k from paris of electric fields. The high field value is shown on the $\hat{x}$ axis. The dashed horizontal line is the weighted average $k = 0.72618(19)$ Hz $(\mathrm{V/cm})^{-2}$ and the solid lines show the one σ error bars.

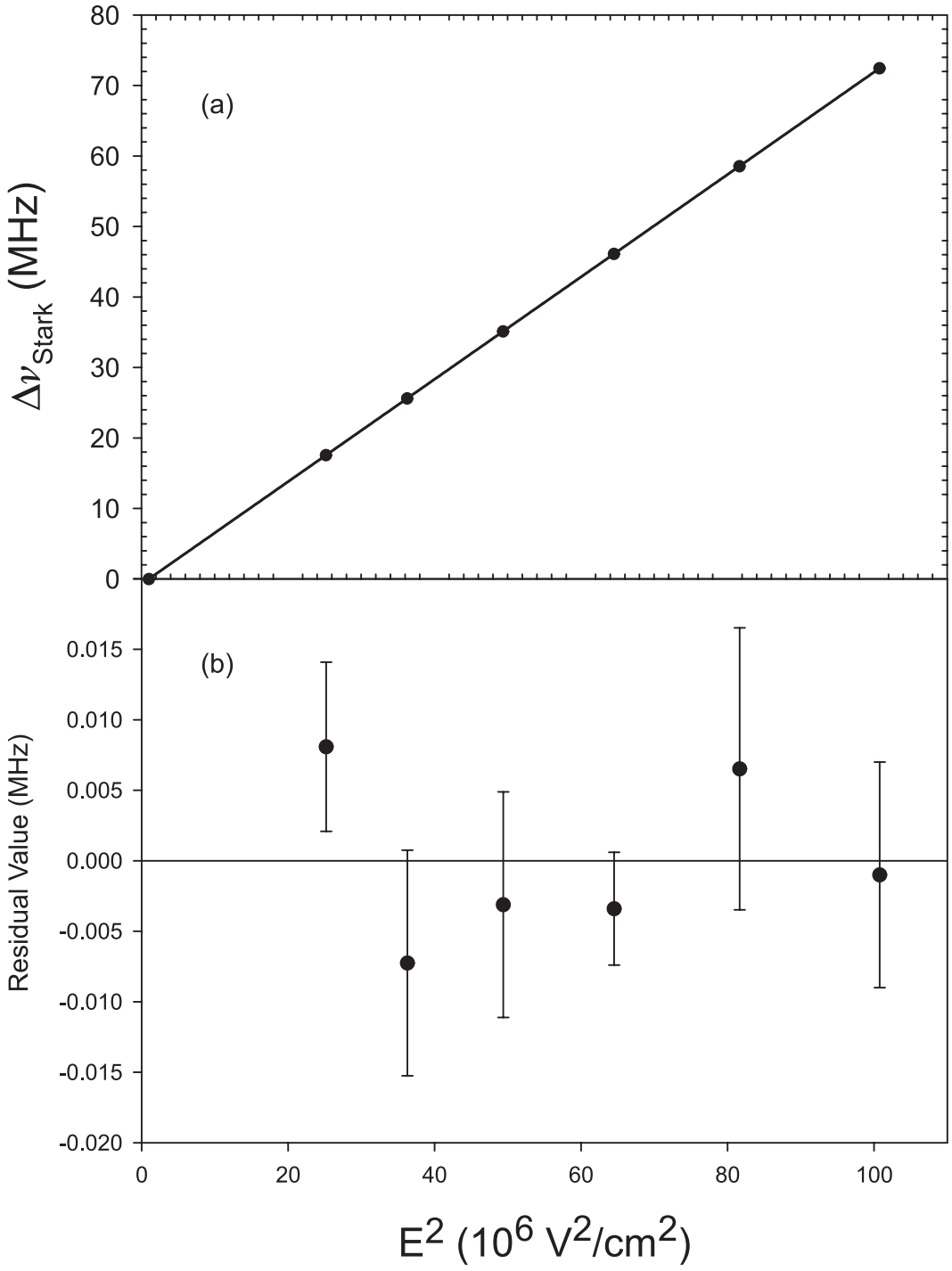

Figure 4.9: (a) Measured values and (b)residuals of $\Delta\nu_{\mathrm{Stark}}$ plotted as a function of E^2. In (a) The error bars are smaller than the data points and values from scans with the same values of E have been averaged together. The solid line is a fit to the data assuming $\Delta\nu_{\mathrm{Stark}} \propto E^2$. The result is $k = 0.72620(13)$ Hz $(\mathrm{V/cm})^{-2}$.

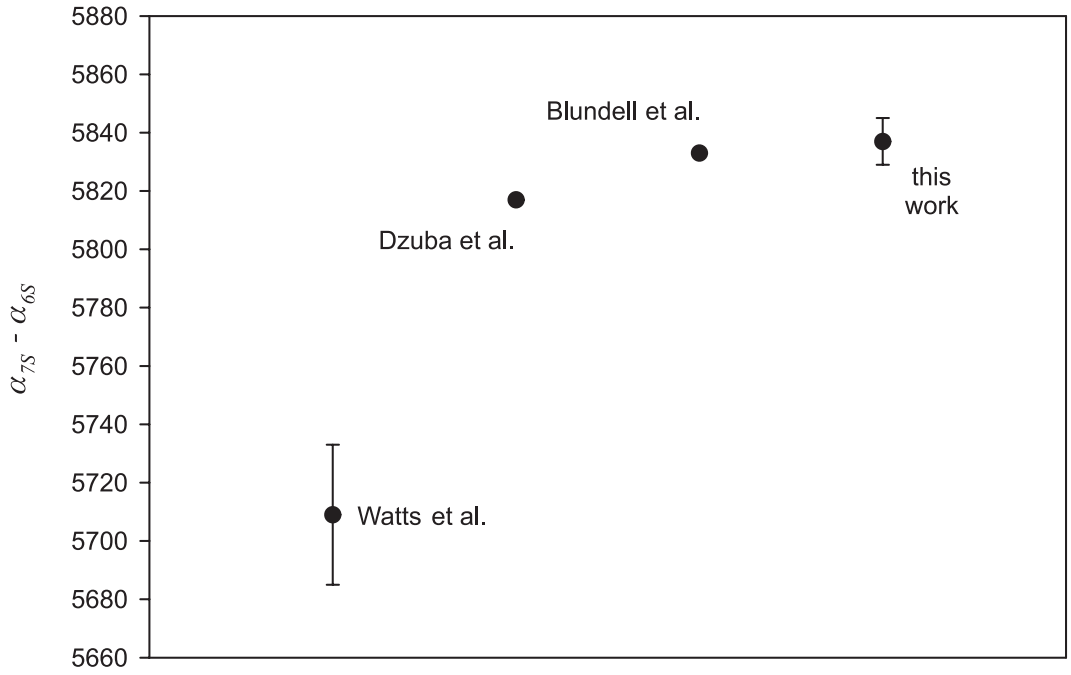

Figure 4.10: A comparison of determinations of the dc Stark shift of the $6S \rightarrow 7S$ transition. The number of Watts *et al.* is from Ref. [49], the number of Dzuba *et al.* is from a private communication, and the number of Blundell *et al.* is from Ref. [14].

CHAPTER 5

MEASURING THE TENSOR TRANSITION POLARIZABILITY

As discussed in Chapter 1, the standard model can be tested by extracting the value of the weak charge Q_W from the equation

$$\frac{\mathrm{Im}(E_{\mathrm{PNC}})}{\beta} = -i\frac{Q_W}{\beta N}k_{\mathrm{PNC}}, \tag{5.1}$$

where the value of $\mathrm{Im}(E_{\mathrm{PNC}})/\beta$ has been measured to 0.35% [13]. Also discussed was the fact that atomic theory calculations are needed to determine the values of k_{PNC} and β*. Because the uncertainty in the theory is the limiting factor in the test of the standard model, it is desirable to reduce the dependence on theory by making an independent measurement of β.

While the measurements of the dc Stark shift and β are both accomplished by scanning a dye laser across the $6S \rightarrow 7S$ transition and measuring the transition rate as a function of frequency, the latter experiment is susceptible to many more problems. Measuring the dc Stark shift requires only the accurate measurement of the frequency separation of two spectral lines. The line shapes, contributions from background signals, magnetic field perturbations, and contamination of the signal from unwanted amplitudes are all examples of effects that do not affect the dc Stark shift measurement but are important for measuring β.

This chapter details our measurement of β. It begins with a description

*β has also been determined semi-empirically, but the calculation from the atomic theory has higher precision.

of the basic idea behind the measurement and continues with a detailed discussion of the experimental complications that must be addressed to make an accurate and precise measurement. The raw data are then presented, and the chapter concludes by covering the issue of the presence of an electric quadrupole transition. The electric quadrupole amplitude has affected previous experiments, and its effects must be considered carefully in the present measurement. A full mathematical treatment of these effects is given in Appendix B.

5.1 Experimental Concept

As discussed in Section 2.7, in order to determine β, we need to first measure the $E1$ and $M1$ amplitudes on the $\Delta F = \pm 1$ transitions. We do this by scanning the dye laser across the appropriate $6S \rightarrow 7S$ transitions and integrating the total fluorescence collected on the probe photodiode. These integrated areas are proportional to the transition rates. If we then take the ratio of the $M1$ area (measured with no applied E) and the $E1$ area (measured with $E = 700$ V/cm), all the unknown parameters (such as beam flux, probe detection efficiency, and intensity inside the PBC) cancel, and to a good approximation we are left with the ratios

$$R^{\pm} \equiv \left(\frac{M \mp M_{\rm hf}}{\beta E} \right)^2 , \tag{5.2}$$

where $R^{\pm}$ correspond to the $\Delta F = \pm 1$ transitions. From these ratios we can extract the value of $M_{\rm hf}/\beta$. [See Eq. (5.6) and Eq. (5.7) for minor corrections.] Then we can use the value of $M_{\rm hf}$ determined in Ref. [27] to extract β. The amplitude $M_{\rm hf}$ can be determined very precisely because it is related to the well-known hyperfine splittings of cesium. The goal is to measure $M_{\rm hf}/\beta$ with a precision of 0.1%. The uncertainty in the final value of β is then dominated by the 0.25% determination of $M_{\rm hf}$ [27].

5.2 Experimental Considerations

5.2.1 Measuring the Areas Correctly

Determining a transition amplitude by measuring the area underneath a spectral feature is straight forward if the line shape fits a well known function, for example a Voigt function. Our line shapes do not fit simple functions, so we must find another way to extract the amplitude.

Consider the sample line shape shown in Fig. 5.1. The signal detected on the photodiode as a function of laser frequency is $f(\nu)$, which is the sum of two quantities: the signal from atoms making the $6S \rightarrow 7S$ transition, represented by $h(\nu)$, and the signal from all other contributions, represented by $BG(\nu)$. The

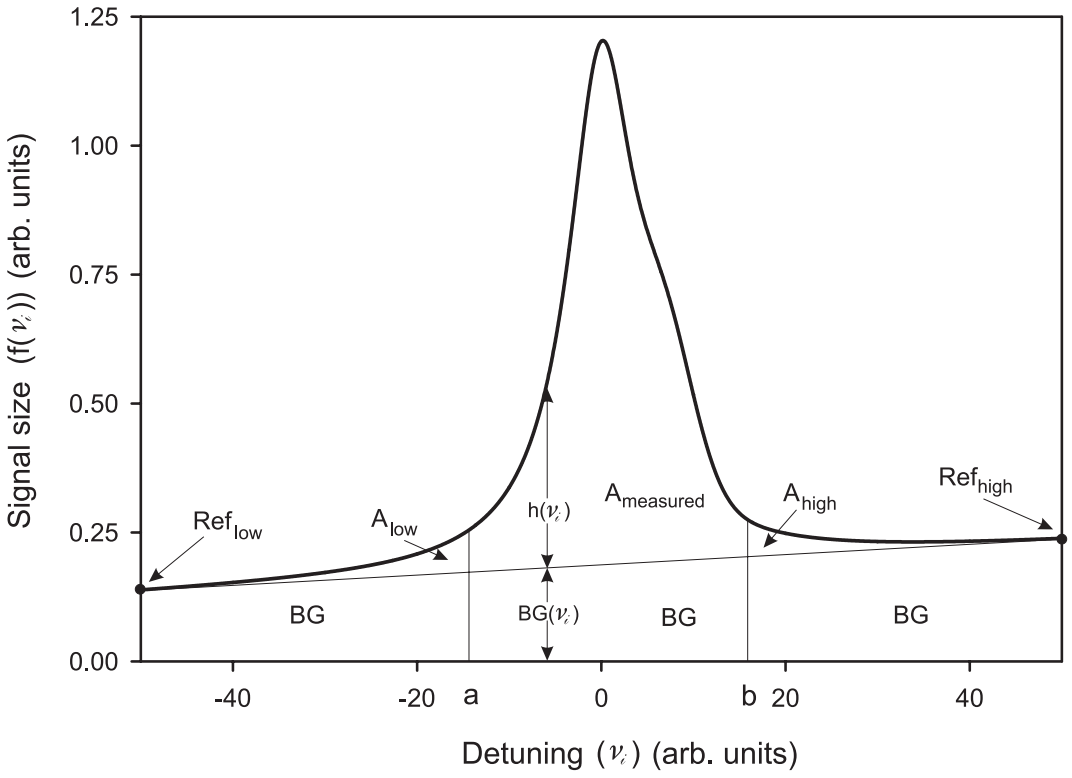

Figure 5.1: A hypothetical scan across the $6S \rightarrow 7S$ transitions. The total signal is $f(\nu_i)$ and the background is $BG_(\nu_i)$. See text for discussion of the symbols in the figure.

quantity we want to measure is given by

$$A_{\mathrm{Total}} = \int_{-\infty}^{\infty} h(\nu) d\nu. \tag{5.3}$$

Of course, we make measurements of the signal size at discrete frequencies, and we can only scan the frequency of the laser within its tunable frequency range. In addition, we cannot measure $h(\nu)$ directly. Rather, we must calculate it from the difference between $f(\nu)$ and $BG(\nu)$. We then have

$$\begin{aligned} A_{\mathrm{Total}} &= \sum_{i=-\infty}^{\infty} [f(\nu_i) - BG(\nu_i)]\Delta\nu_i \\ &= \sum_{i<a} [f(\nu_i) - BG(\nu_i)]\Delta\nu_i + \sum_{i=a}^{b} [f(\nu_i) - BG(\nu_i)]\Delta\nu_i \\ &\quad + \sum_{i>b} [f(\nu_i) - BG(\nu_i)]\Delta\nu_i \\ &= A_{\mathrm{low}} + A_{\mathrm{measured}} + A_{\mathrm{high}}. \end{aligned} \tag{5.4}$$

Clearly we must choose a and b such that A_{low} and A_{high} are negligible. Then we are left with A_{measured}. We are still left with two problems: the noise on the background and the fact that we can only measure $f(\nu_i)$, not $h(\nu_i)$ and $BG(\nu_i)$.

If the background is a linear function of frequency then we can measure its value at a low reference point and a high reference point where the contribution from $h(\nu_i)$ is negligible. Then, if these two reference points are centered around the peak of the transition, we can take their average and use $\sum[f(\nu_i) - BG(\nu_i)] = \sum[f(\nu_i) - BG_{\mathrm{AVG}}]$ to subtract off the contribution from the background. If the background is nonlinear, this method does not give the right answer.

The contributions to the background level from known sources are all essentially linear functions of the dye laser frequency or independent of it. These sources are atoms left in the wrong hyperfine state, scattered light from the PBC mirrors, and scattered light from the probe and hyperfine pumping lasers. The only contri-

bution to the background that might be nonlinear is from molecules interacting with the dye laser and being detected by the probe laser in a frequency sensitive manner. However, we measure the background with varying oven nozzle temperatures (which vary the fraction of Cs_2 molecules in the beam) and find no measurable molecular background. Therefore, the procedure in the previous paragraph does give the correct answer.

Another complication is the fact that there is noise on the background, and this $1/f$ noise is our limiting source of noise. Thus, if we measure the background at the high and low reference points and subsequently scan across the transition, the background will be slightly different at each measurement of $f(\nu_i)$ than it was when we first measured it. To solve this problem, we take advantage of our $\sim$25 Hz data taking frequency: before and after **each** measurement of $f(\nu_i)$ we measure the background at the high and low reference points. In this way we get the average background **at the time of the measurement** of $f(\nu_i)$. We also alternate which reference comes first to eliminate problems that might arise due to hysteresis.

Finally, we must know the frequency separation $\Delta\nu_i$ between each measurement of the transition rate. This is because we are essentially determining the area of the line shape using the trapezoidal rule. We must know both the height and the width of each "rectangle" we use to determine the total area. If the rectangles are not of uniform width and we assume they are, we will get an incorrect result. Therefore, we calibrate the control voltage from the computer to obtain sufficient accuracy in our knowledge of ν_i.

5.2.2 Comparing the Areas Correctly

As mentioned in Chapter 4, the line shapes of the $6S \rightarrow 7S$ transition are asymmetric because of the ac Stark effect [30]. The ac Stark effect causes another problem: it shifts and distorts the $M1$ transitions differently from the $E1$ transitions. This is because the $E1$ transition is driven by the oscillating electric field ($\epsilon_{\rm ac}$) of

the laser and the $M1$ transitions are driven by the oscillating magnetic field ($b_{\rm ac}$) of the laser, while the ac Stark effect causes the largest shift where $\epsilon_{\rm ac}$ is large. Thus, in the regions of large $\epsilon_{\rm ac}$ there is a large ac Stark shift and a high* probability of driving an $E1$ transition. In regions of small $\epsilon_{\rm ac}$ (and a correspondingly large $b_{\rm ac}$) there is a small ac Stark shift and a large probability of driving an $M1$ transition. This effect is shown dramatically in Fig. 5.2.

If the line shapes for the two transitions had simple Voigt profiles with the same widths, for example, and we missed 1% of each area in the wings, the ratio will still be correct. That is $M1/\beta = (0.99 \times M1)/(0.99 \times \beta)$. However, since the two line shapes do not have the same width and they are offset, it would be easy to miss 1% of β and only miss 0.1% of $M1$. We avoid this problem by making the scans across the transitions wide enough to measure all the area for both transitions. We also confirm that the scan width is wide enough by reanalyzing the data by omitting increasingly large amounts of data from the beginning and end of the scans. We do not find a significant variation in the ratios when we do the reanalysis.

The discussion so far has implied that all we need to do is scan across the $M1$ transition and then scan across the $E1$ transition and we have the two values we need to determine the ratio. However, when we scan across the $E1$ transition, the $M1$ transition is not absent, it is just very small. The ratio we actually measure is

$$R^{\pm}_{\rm measured} = \frac{(M \mp M_{\rm hf})^2}{\beta^2 E^2 + (M \mp M_{\rm hf})^2}. \tag{5.5}$$

The ratio we actually want is given by

$$R^{\pm} = \frac{(M \mp M_{\rm hf})^2}{\beta^2 E^2} = \frac{R^{\pm}_{\rm measured}}{1 - R^{\pm}_{\rm measured}}. \tag{5.6}$$

*The terms "high" and "low" are only used in the relative sense. For example, there may be a "high" probability of making a Stark-induced $E1$ transition, but that transition amplitude is over seven orders of magnitude smaller than the $D1$ electric dipole transition.

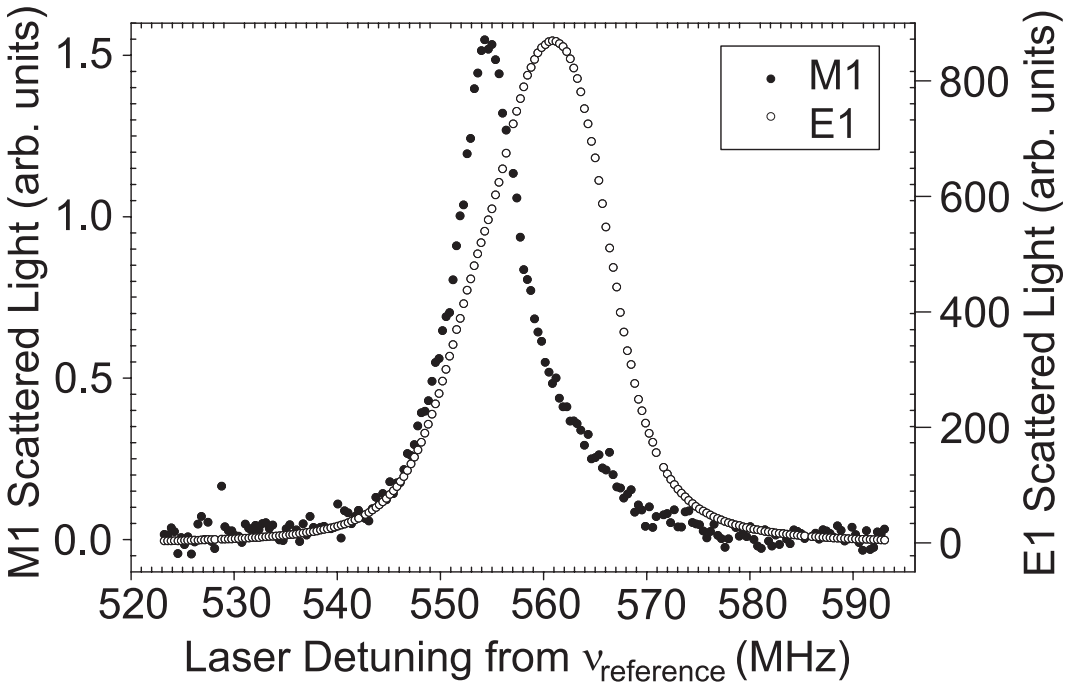

Figure 5.2: Plot comparing the $E1$ and $M1$ line shapes. The asymmetries in the line shapes and the differences in widths and center frequencies are due to the ac Stark effect as discussed in Ref. [30].

5.2.3 Photoionization Correction

Just as the ac Stark effect's dependence on $\epsilon_{\rm ac}$ combines with the dependence of $E1$ on $\epsilon_{\rm ac}$ and $M1$ on $b_{\rm ac}$ to give different line shapes, photoionization also causes a difference in detection efficiency between $E1$ and $M1$ because it is also maximum where $\epsilon_{\rm ac}$ is maximum. This is explained in the following manner.

Atoms that are in a region with a large $\epsilon_{\rm ac}$ have a high probability of making an $E1$ transition. The same atoms also have a high probability of being photoionized. Atoms in a region with a large $b_{\rm ac}$ have a high probability of making an $M1$ transition. However, these atoms have a small probability of being photoionized. Any atoms that are photoionized are no longer available to be detected downstream in the detection region. Thus, a smaller fraction of atoms that made the $E1$ transition is available for detection relative to the fraction of atoms that made the $M1$ transition.

The result is that as the intensity inside the PBC gets higher, the ratio $M \pm M_{\rm hf}/\beta$ gets correspondingly larger. With this effect, the ratios on the two transitions are given by

$$R_I^{\pm} \equiv (\frac{M \mp M_{\rm hf}}{\beta E})(1 + \eta I). \tag{5.7}$$

The intensity inside the PBC is proportional to the power that is transmitted through the output mirror, which we measure on a photodiode. I is this voltage, and η is a parameter that describes the difference in photoionization probabilities. In order to correct for this effect, we must take data at several intensities and extrapolate the result to zero intensity. The data taken for this correction are shown in Section 5.3.

5.2.4 Non-B_z Magnetic Field Systematic Error

As mentioned in Section 2.6, a misaligned magnetic field can change the definition of the operator $\vec{\sigma}$. This, in turn, changes the rates we measure. Using Eq. (2.28) and Eq. (2.25) we find that the ratios we measure become

$$R = \frac{(M \mp M_{\rm hf})^2 \sum_{m'_F} \left[\left(\frac{B_z}{B}\right)^2 (C_{Fm_F}^{F\pm 1 m'_F})^2 \delta_{m'_F m_F \pm 1} + \left(\frac{B_x}{B}\right)^2 (C_{Fm_F}^{F\pm 1 m'_F})^2 \delta_{m'_F m_F} \right]}{\beta^2 E^2 \sum_{m'_F} (C_{Fm_F}^{F\pm 1 m'_F})^2} \tag{5.8}$$

for a small rotation of $\vec{B}$ into the $\hat{x}$ axis, and

$$R = \frac{(M \mp M_{\rm hf})^2 \sum_{m'_F} (C_{Fm_F}^{F\pm 1 m'_F})^2}{\beta^2 E^2 \sum_{m'_F} \left[\left(\frac{B_z}{B}\right)^2 (C_{Fm_F}^{F\pm 1 m'_F})^2 \delta_{m'_F m_F \pm 1} + \left(\frac{B_y}{B}\right)^2 (C_{Fm_F}^{F\pm 1 m'_F})^2 \delta_{m'_F m_F} \right]} \tag{5.9}$$

for a small rotation of $\vec{B}$ into the $\hat{y}$ axis. This would not be a problem if the populations of the m_F sublevels were uniform. This is because

$$\sum_{m_F} (C_{Fm_F}^{F\pm 1 m_F})^2 = 2 \sum_{m_F} (C_{Fm_F}^{F\pm 1 m_F \pm 1})^2. \tag{5.10}$$

Therefore, the ratios are constant, regardless of the value of B_x or B_y.

However, we know that pumping the atoms into a single hyperfine state redistributes the atoms in a nonuniform way. The populations from a uniform distribution, from a simple Monte Carlo rate equation simulation, and from a full quantum mechanical treatment are shown in Table 5.1. When we pump atoms into the $F = 3$ state, more atoms tend to fall into the Zeeman sublevels near $m_F = 0$, and when we pump atoms into the $F = 4$ state, more atoms tend to fall into the Zeeman sublevels near $|m_F| = 4$.

The $C_{Fm_F}^{F'm'_F}$ coefficients have a nonuniform dependence on the initial m_F state that is similar to the dependence of the Zeeman sublevel population distribution. The $\Delta m_F = 0$ transitions are stronger for transitions starting from near $m_F = 0$, and the $\Delta m_F = \pm 1$ transitions are weaker for the same transitions. The result is that on the $F = 3$ to $F' = 4$ ($F = 4$ to $F' = 3$) transitions the numerator gets larger (smaller) as $\vec{B}$ rotates into $\hat{x}$ and weights the $\Delta m_F = 0$ transitions more heavily. Similarly the denominator gets larger (smaller) as $\vec{B}$ rotates into $\hat{y}$. This behavior has been verified experimentally. The results of the theory are compared

Table 5.1: The fractional population in a given Zeeman sublevel after hyperfine pumping has been performed. The uniform distribution assumes that no redistribution of the populations takes place. "Bennett" refers to the populations found using a simple Monte Carlo simulation of hyperfine pumping. "Marte" refers to the results of a full quantum mechanical calculation performed by Peter Marte [56].

		Method					Method		
F	m_F	Uniform	Bennett	Marte	F	m_F	Uniform	Bennett	Marte
3	3	0.1429	0.1030	0.1163	4	4	0.1111	0.1430	0.1230
	2	0.1429	0.1570	0.1442		3	0.1111	0.1308	0.1061
	1	0.1429	0.1598	0.1632		2	0.1111	0.1067	0.1038
	0	0.1429	0.1598	0.1666		1	0.1111	0.0831	0.1040
	-1	0.1429	0.1598	0.1593		0	0.1111	0.0749	0.1109
	-2	0.1429	0.1570	0.1369		-1	0.1111	0.0831	0.1028
	-3	0.1429	0.1030	0.1134		-2	0.1111	0.1067	0.1068
						-3	0.1111	0.1308	0.1104
						-4	0.1111	0.1430	0.1321

with data in Fig. 5.3. The results shown are for the $F = 4$ to $F' = 3$ transition with the magnetic field rotated into the $\hat{x}$ direction. It is clear that the full quantum mechanical treatment gives reasonable qualitative agreement.

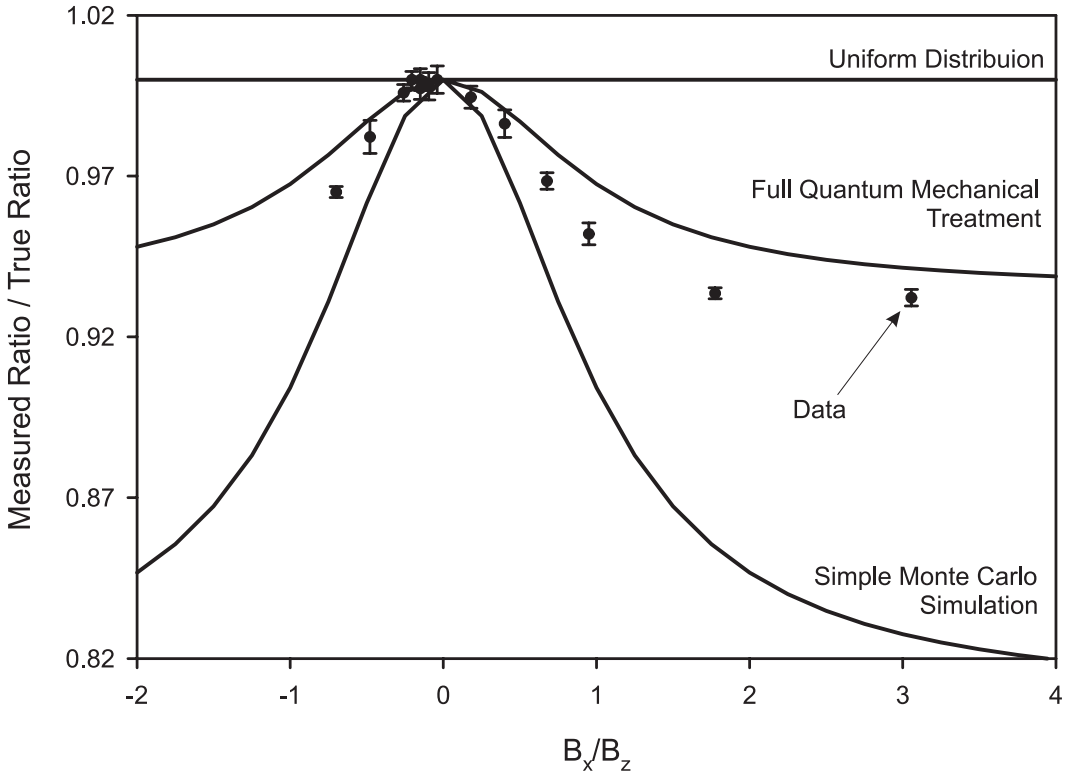

Figure 5.3: Data and theory showing the effect of misaligned $\vec{B}$ on the ratio $M + M_{\rm hf}/\beta$ on the $F = 4$ to $F' = 3$ transition. Here the magnetic field is rotated into the $\hat{x}$ direction.

This error due to misaligned magnetic fields is the most serious systematic error we need to address. Using the data we collected (not the theoretical prediction), we find that in order to have the effect of a misaligned magnetic field contribute less than 0.02% we must keep B_x and B_y less than 220 mG when the main field is set at $B_z = 4$ G. This is an easy requirement to meet since we routinely kept these fields less than 1 mG for the PNC measurement. To confirm the absence of any effect we also take data with main magnetic fields smaller than 4 G. If there is a residual misaligned component, the fractional error in the ratio will get larger as the main

field gets smaller. These data are shown in Fig. 5.4. The fractional difference between

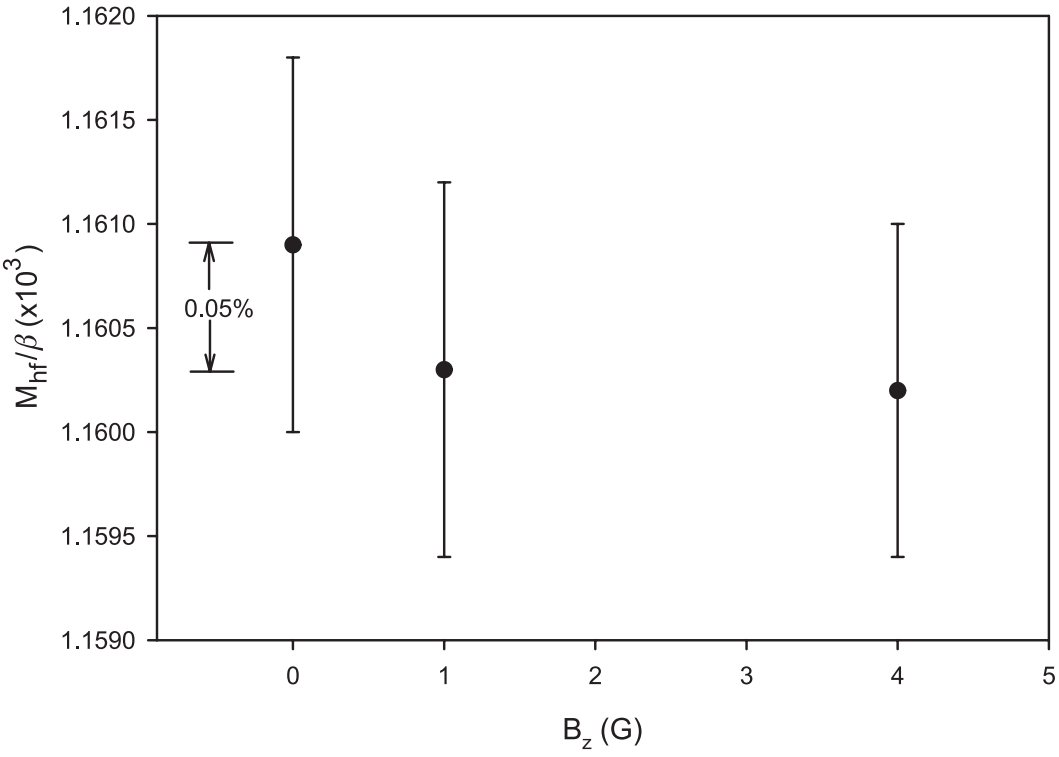

Figure 5.4: Measured ratios $M_{\rm hf}/\beta$ as a function of B_z. Any deviation as the value of B_z is scaled indicates the presence of a misaligned B_x or B_y.

the measurements at 1 G and 4 G is $0.1(1.0) \times 10^{-3}$. The misaligned magnetic field that is required to give this change is 9.5±95 mG. If we assume the actual stray field is 100 mG, then the field is a factor of two smaller than the maximum misaligned field we can tolerate. Thus, the error due to a misaligned field is negligible in our measurements.

5.3 Preliminary Data

The final data taken to measure the ratio $M_{\rm hf}/\beta$ were taken over a period of one week and the conditions of the experiment were changed twice during that period to ensure the measured ratio did not depend on things that we thought it should not, for example collimator angle (which changes the direction of the atomic

beam), alignment of the dye laser into the PBC, and beam density. The raw data with no corrections are shown in Table 5.2. A least squares fit of these data to

Table 5.2: Table of raw data for the ratios $R_I^{\pm} = (M \pm M_{\rm hf}/\beta E)(1 + \eta I)$ with no corrections and with $E = 707.63(68)$.

I	R^+ (10^{-3})	R^- (10^{-3})
2.300	2.5112(06)	1.1602(08)
2.000	2.5047(12)	1.1573(16)
1.500	2.4926(10)	1.1522(24)
1.000	2.4793(29)	–
0.800	2.4775(34)	–

Eq. (5.7) with the correction shown in Eq. (5.6) gives

$$R_I^+ = 2.4636(24) \times 10^{-3}[1 + 0.009522(13)I\,]. \tag{5.11}$$

The data plotted against this line are shown in Fig. 5.5. The reduced χ^2 for the fit is 0.20 indicating a probability of 90% that the data come from a random distribution.

The correction for photoionization is dominated by the fraction of atoms that make the $E1$ transition. Therefore, the fact that $M1_{3\to4} = M - M_{\rm hf}$ compared to $M1_{4\to3} = M + M_{\rm hf}$ has no effect of the correction $(1 + \eta I)$ and we expect that the correction factor η is the same for both ratios. If we use the slope from the R^+ fit to find the least squares fit to the R^- data we find that

$$R_I^- = 1.1357 \times 10^{-3}[1 + 0.009522I\,]. \tag{5.12}$$

The reduced χ^2 for this fit indicates a 90% probability that the data come from a random distribution. This means the data are consistent with our assumption that both ratios scale the same way with intensity. However, we do not use this fit to determine $M_{\rm hf}/\beta$ because the poor signal-to-noise ratio on the $F = 4$ to $F' = 3$ transition at low intensities does not allow sufficient precision in the determination

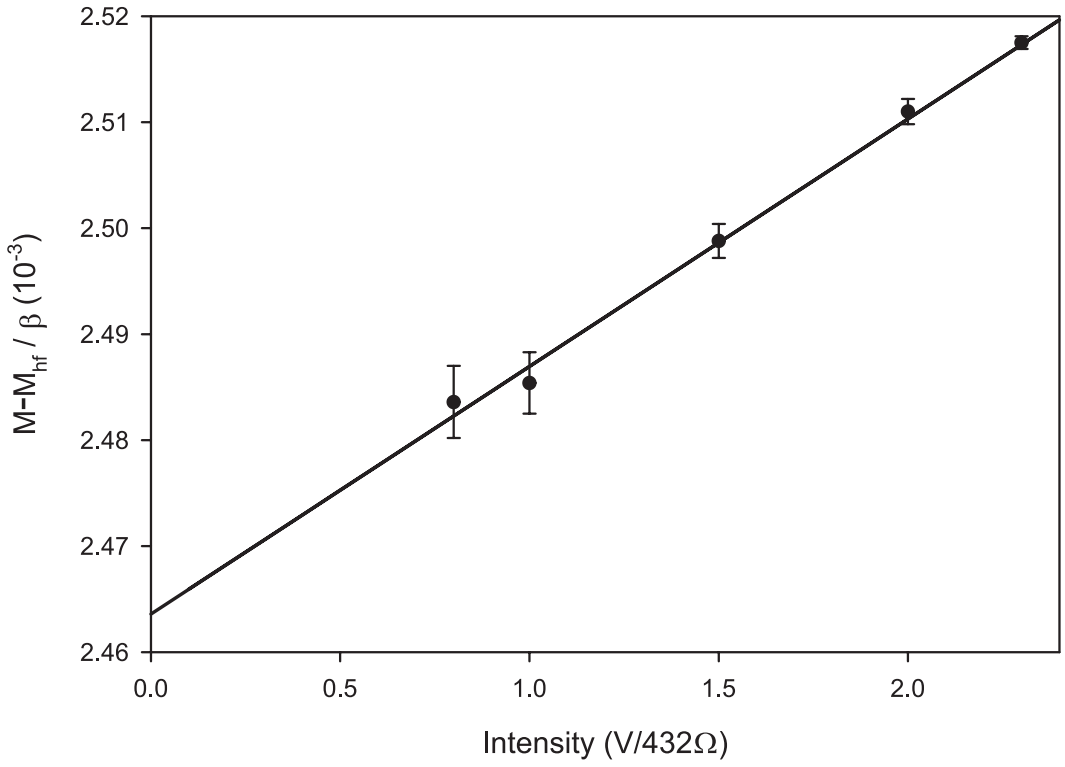

Figure 5.5: Plot of $M - M_{\rm hf}/\beta$ vs. laser intensity showing the effect of photoionization.

of R_0^-. Instead, we use the ratio R_I^+/R_I^- using data at higher intensities where the signal-to-noise ratio is high. This does allow sufficient precision, and it eliminates the need to determine R_0^-.

The equation

$$\frac{M_{\rm hf}}{M} = \frac{1 - \sqrt{R_I^+/R_I^-}}{1 + \sqrt{R_I^+/R_I^-}} \tag{5.13}$$

gives the value of $M_{\rm hf}/M$ without the need to make a correction for photoionization effects. The weighted average of R_I^+/R_I^- for the three largest intensities shown in Table 5.2 corrected according to Eq. (5.6) is $R_I^+/R_I^- = 2.1673(14)$. This gives a preliminary value of $M_{\rm hf}/M = -0.1910(2)$.

The equation

$$\frac{M_{\rm hf}}{\beta} = \sqrt{R_0^+}\left(1 - \sqrt{\frac{R_I^-}{R_I^+}}\right)\frac{E}{2} \tag{5.14}$$

gives the value of $M_{\rm hf}/\beta$. Here it is only necessary to use the determination of R_0^+, and we can use the more precise values of R^- at higher intensities. The preliminary value is $M_{\rm hf}/\beta = -5.6325(85)$ V/cm. We can combine this value with $M_{\rm hf} = -151.86(38)\,a_0^3$ V/cm [27] to arrive at the value $\beta = 26.962(41)_{\rm expt}\,(67)_{\rm theory}\,a_0^3$. However, these values need to be corrected for $E2$.

5.4 Accounting for the Electric Quadrupole Amplitude

The data given in the previous section is very nearly the final data, with the effects of magnetic field misalignments, photoionization, offset line centers, asymmetric line shapes, and nonzero background taken into consideration. However, we have not yet considered the effects of the electric quadrupole amplitude ($E2$) in the measurements. If we had a uniform population distribution among the m_F states there would be no correction for the $E2$ amplitude because its effects cancel exactly. (See Appendix B.) We do not have a uniform distribution, as discussed in Section 2.6, so we need to correct the data.

Electromagnetic amplitudes beyond the usual electric and magnetic dipole amplitudes are commonly ignored because of their relatively small size compared to allowed $E1$ and $M1$ amplitudes. However, when dealing with amplitudes such as the PNC $E1$ amplitude and the first-order forbidden $M1$ amplitude, the $E2$ amplitude must be considered to reach accuracies of 0.1%.

Bouchiat and Guéna [27] consider the $E2$ amplitude in their reanalysis of several experiments that determine the ratio $M_{\rm hf}/M$ for the $6S \rightarrow 7S$ transition in cesium. In particular, they say that the work of Ref. [28] does not measure $M_{\rm hf}/M$,

but instead measures the ratio

$$R = \frac{M_{\rm hf}}{M}\left(1 - \frac{3}{4}\frac{E2}{M_{\rm hf}}\right). \tag{5.15}$$

Clearly, if the ratio $E2/M_{\rm hf}$ is small enough, there is no error. However, the results of Ref. [27] indicate that $E2/M_{\rm hf} = 42(13) \times 10^{-3}$ and so $M_{\rm hf}/M = -0.1886(17)$ rather than the value $M_{\rm hf}/M = -0.1830(4)$ found in Ref. [28]. Indeed, if we compare this with our result of $M_{\rm hf}/M = -0.1910(2)$, there is clearly a discrepancy.

As shown in Appendix B, if we have the population distributions calculated by Peter Marte, then the measurements of the ratio R^+ need a -0.094% correction and the measurements of the ratio R^- need a $+0.079\%$ correction. This is a small but significant correction to our data. The revised numbers that follow assume that there is a 50% uncertainty in these corrections, mainly from the uncertainty in the determination of the population distribution.

To arrive at the fractional corrections in the previous paragraph, we begin by assuming that the $E2$ amplitude does not affect our measurements. The difference between the values of $M_{\rm hf}/M$ determined by the present experiment and in Ref. [28] then gives us the value of $E2/M_{\rm hf}$ using the equation

$$\left(\frac{M_{\rm hf}}{M}\right)_{\rm present} = \left(\frac{M_{\rm hf}}{M}\right)_{\text{Ref. [28]}}\left(1 - \frac{3}{4}\frac{E2}{M_{\rm hf}}\right)^{-1}. \tag{5.16}$$

Then we use this value of $E2/M_{\rm hf}$ to correct our data for the $E2$ contributions. Our new value of $M_{\rm hf}/M$ can again be compared with that of Ref. [28] to determine an improved value of $E2/M_{\rm hf}$, and so on. This procedure is iterated until we arrive at an internally consistent value of $E2/M_{\rm hf}$. Our final value is $E2/M_{\rm hf} = 53(2) \times 10^{-3}$, which gives the corrections mentioned above. The final results for this experiment are given in Table 5.3. Our new value of β is compared to previous results in Fig. 5.6.

Table 5.3: Final results for the $M_{\rm hf}/\beta$ experiment. The uncertainties shown are one sigma values. In the first three values, the uncertainty is purely experimental, and in the final value the uncertainties have been separated into their contributions from experiment and theory.

Quantity	Without $E2$ Correction	With $E2$ Correction
$E2/M_{\rm hf}$	–	0.053(3)
$M_{\rm hf}/M$	−0.1910(2)	−0.1906(3)
$M_{\rm hf}/\beta$ (V/cm)	−5.6325(85)	−5.6195(91)
$\beta\,(a_0^3)$	$26.962(41)_{\rm expt}\,(67)_{\rm theory}$	$27.024(43)_{\rm expt}\,(67)_{\rm theory}$

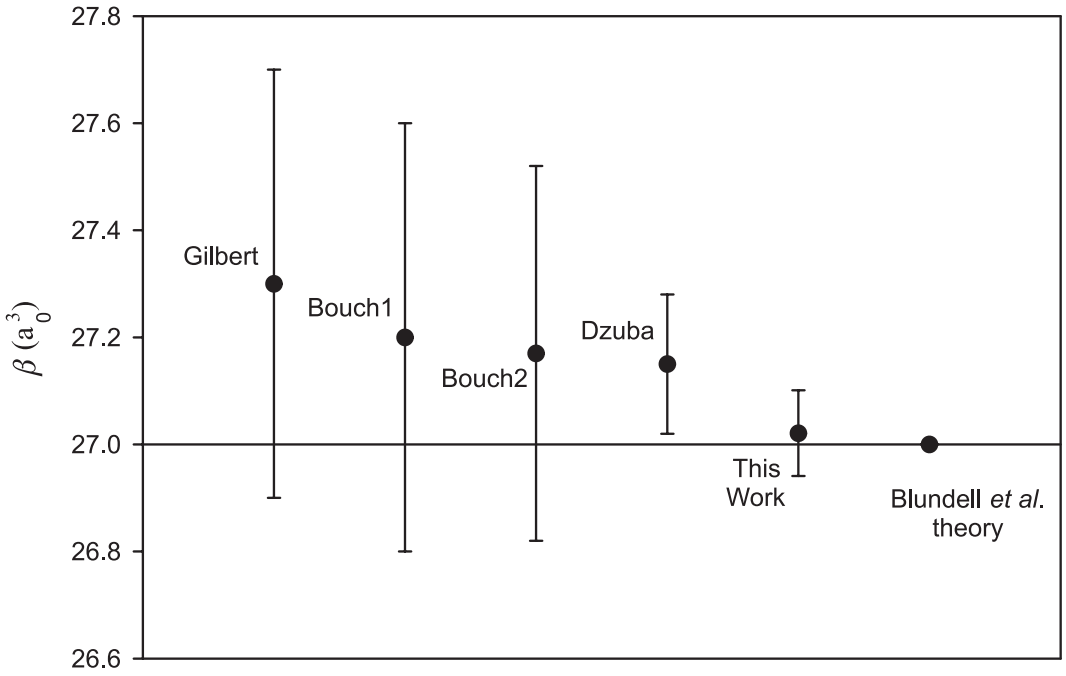

Figure 5.6: An historical comparison of the determinations of β. Gilbert is from Ref. [57], Bouch1 is from Ref. [58], Bouch2 is from Ref. [59], Dzuba is from Ref. [24], and the theory is from Ref. [14].

CHAPTER 6

CONCLUSIONS AND IMPLICATIONS

We have now presented the two main results of this thesis. We find that the $6S \rightarrow 7S$ dc Stark shift is $k = 0.7262(8)$ Hz(V/cm)$^{-2}$, and we find that the $6S \rightarrow 7S$ tensor transition polarizability is $\beta = 27.024(43)_{\rm expt}(67)_{\rm theory} a_0^3$. We will now use the measurement of the dc Stark shift to re-evaluate the uncertainty of the atomic theory calculations, and then use our new measurement of β, along with our previous measurement of $\mathrm{Im}(E_{\rm PNC})/\beta$, to obtain a value for the weak charge Q_W. This value of Q_W will be compared with the prediction of the standard model. The comparison provides a test of the standard model.

6.1 Re-evaluation of Atomic Theory

The test of the standard model using a measurement of PNC in atomic cesium requires calculations of the cesium matrix elements. If the uncertainty of the experiment is significantly smaller than the uncertainty of the calculations, then the test will be limited by the theory.

There are two groups that have made a considerable effort to develop the theory to determine the structure of cesium: Blundell, *et al.* [43, 14, 45] at the University of Notre Dame and Dzuba, *et al.* [15, 47, 48] now at the University of New South Wales. The most important result of their calculations is the value of

$k_{\rm PNC}$, which is given by

$$k_{\rm PNC} = \frac{N}{Q_W}\sum_n \left(\frac{\langle 7S \mid \vec{D} \mid nP\rangle\langle nP \mid H_{\rm PNC} \mid 6S\rangle}{E_{6S}-E_{nP}} + \frac{\langle 7S \mid H_{\rm PNC} \mid nP\rangle\langle nP \mid \vec{D} \mid 6S\rangle}{E_{7S}-E_{nP}} \right). \tag{6.1}$$

The quantity $k_{\rm PNC}$ is made up of two types of matrix elements: allowed electric dipole matrix elements like $\langle 6P \mid \vec{D} \mid 6S\rangle$, and unmeasurable matrix elements like $\langle 6P \mid H_{\rm PNC} \mid 6S\rangle$. Because $H_{\rm PNC}$ is proportional to the Dirac matrix γ^5, these latter matrix elements are essentially the matrix elements of γ^5.

Of equal importance to the calculated value of $k_{\rm PNC}$ is the accuracy of the calculation; if the calculation is only good to 2%, then the subsequent test of the standard model is limited to 2%. Therefore, the two groups have spent considerable time evaluating the accuracy of their calculations. Because the behavior of the two sorts of matrix elements is so different—the matrix elements of $\vec{D}$ are sensitive to the value of the wave function at large $\vec{r}$ and the matrix elements of γ^5 are sensitive to values of small $\vec{r}$—one must be careful to test the predictions of the theory using quantities that behave in a similar fashion to both of these matrix elements. The most objective way to estimate the accuracy of the theory is to compare its predictions with the results of experiments.

In order to provide these comparisons, many groups have performed high-precision measurements of the properties of cesium. Among the most precise of these are measurements of the hyperfine structure constants. These measurements are particularly relevant because of the similarity of their behavior to the behavior of the matrix elements of γ^5. Other precise measurements are of the lifetimes of excited states such as the $6P_{\frac{1}{2},\frac{3}{2}}$ states. The lifetime measurements are important because they involve the same radial matrix elements as $k_{\rm PNC}$, such as $\langle 6P \mid \vec{D} \mid 7S\rangle$.

To quote from Ref. [14]: "If all known properties of cesium could be reproduced by some *ab initio* calculation scheme to within 0.1%, we feel it would be rea-

sonable to trust a PNC calculation carried out in the same fashion to this same level, subject to a scatter analysis along the lines presented above." The "scatter analysis" mentioned is one where the measured values of E_{nS}, E_{nP}, and $\langle nS \mid \vec{D} \mid nP \rangle$ are used in different combinations with *ab initio* calculations to estimate how much the value of $k_{\rm PNC}$ would change with small changes in the calculated parameters*.

In Blundell *et al.* [14], the authors quote a variation of 0.78%, but the standard deviation of their calculated numbers is more accurate: $\sigma = 0.40\%$. Thus, if we can show that the theory's predictions agree with experiments at the 0.4% level, then it should be reasonable to trust the calculation of $k_{\rm PNC}$ to that same level.

All of the measurements made prior to the publication of Ref. [14] show only small differences from the theory (less than 1%) with the exception of the measurement of the dc Stark shift [49], where there was a 2% difference between the theory and experiment (Chapter 4). This difference is now 0.3%. In addition, there are new experiments that reveal errors in earlier lifetime measurements of sodium [60, 61] and lithium [62]. These new experiments eliminate what had appeared to be troubling 1% errors in calculations for these atoms that are equivalent to the calculations in cesium. Finally, the agreement is very good for the newly-measured $7S \rightarrow 9S$ interval in ^{210}Fr [63, 64]. Now is an opportune time to revisit the comparison between the experiments and the predictions and re-evaluate the uncertainty that should be attributed to the theory.

In Table 6.1 we have collected the most precise measurements of several quantities in cesium that provide tests of the theory, along with the "rescaled" predictions of Dzuba, *et al.* and the *ab initio* predictions of Blundell *et al.*

Particularly notable are the top three lines of the table, which show that the agreement has dramatically improved from the 1-2% agreements of the older

*This scatter analysis is performed by Blundell *et al.* to estimate their uncertainty. They do not change the numbers they report, however. When the *ab initio* calculation of Dzuba *et al.* did not "reproduce the energy level, (they) multiplied the correlation correction by some numerical factor to fit the energy." [47] That is, they use the experimental energies to "correct" their calculations.

Table 6.1: Fractional differences ($\times 10^3$) between measured and calculated values of quantities relevant for testing PNC calculations in atomic cesium. We only list the most precise experiments. The second column lists the most relevant aspects of the wave functions that are being tested. $\langle 1/r^3 \rangle_{nP}$ is the average of $1/r^3$ over the wave function of the electronic state nP. Where the experiment has improved or changed significantly since the publication of Ref. [14], the difference from the old experiment is listed in brackets.

Quantity measured	Calculation tested	Difference ($\times 10^3$) Dzuba[a]	Blundell[b]	σ_{Expt}
6S→7S dc Stark shift[c]	$\langle 7P \,\|\| \, \vec{D} \,\|\| \, 7S \rangle$	$-3.4[19]$	$-0.7[22]$	1.0[4]
$6P_{1/2}$ lifetime[d]	$\langle 6S \,\|\| \, \vec{D} \,\|\| \, 6P_{1/2} \rangle$	$-4.2[-8]$	4.3[1]	1.0[43]
$6P_{3/2}$ lifetime[d]	$\langle 6S \,\|\| \, \vec{D} \,\|\| \, 6P_{3/2} \rangle$	$-2.6[-41]$	7.9[−31]	2.3[22]
α[e]	$\langle 7S \,\|\| \, \vec{D} \,\|\| \, 6P_{1/2} \rangle$, and $\langle 7S \,\|\| \, \vec{D} \,\|\| \, 6P_{3/2} \rangle$	–	-1.4	3.2
β[f]	same as α	–	-0.8	3.0
6S HFS[g]	$\psi_{6S}(r=0)$	1.8	-3.1	–
7S HFS[h]	$\psi_{7S}(r=0)$	-6.0	-3.4	0.2
$6P_{1/2}$ HFS[i]	$\langle 1/r^3 \rangle_{6P}$	-6.1	2.6	0.2
$7P_{1/2}$ HFS[j]	$\langle 1/r^3 \rangle_{7P}$	-7.1	-1.5	0.5

experiments* .

The standard deviation of the fractional differences between theory and experiment in Table 6.1 is 4.0×10^{-3}. We believe this to be the most objective number to use to represent the 68% confidence level for the atomic theory, and thus for the uncertainty on $k_{\rm PNC}$. Using the average of $k_{\rm PNC} = 0.905 \times 10^{-11} ie a_0$ [14] and $k_{\rm PNC} = 0.908 \times 10^{-11} ie a_0$ [15], we find the value

$$k_{\rm PNC} = 0.9065(36) \times 10^{-11} ie a_0. \tag{6.2}$$

6.2 Final Result and Implications

We now have all the numbers—with less than 0.5% uncertainty—to determine the value of the weak charge and to test the standard model. When we

*The footnotes in Table 6.1 are as follows. [a]Refs. [15, 47, 48]; [b] [14, 43, 44, 45]; [c] This work; [d]Ref. [40]; [e] Using the present work and α/β from Ref. [25]; [f]This work; [g]Defined; [h]Ref. [41]; [i]Ref. [65], [i]Ref. [42].

combine the 0.40% value of $k_{\rm PNC}$ from Eq. (6.2) with our new 0.30% value for β and the 0.35% measurement $\mathrm{Im}(E_{\rm PNC})/\beta$ from Ref. [13], we find

$$Q_W = -72.06(28)_{\rm expt}(34)_{\rm theory}. \tag{6.3}$$

This value is virtually the same as our previous result $Q_W = -72.11(27)_{\rm expt}(89)_{\rm theory}$ [13] but more precise. It would be extremely satisfying to use this number to say that the standard model is either right or wrong, but a quick look at a recent 105 page review paper on tests of the standard model [66] shows that it is not an easy task to draw such a simple conclusion.

The value of Q_W given by Eq. (2.2) depends on the two coupling constants C_{1u} and C_{1d}. These constants depend on the definition of $\sin^2\theta_W$, and they depend on which radiative corrections are included in the calculation. Using the analysis of [67, 68], we find that the standard model predicts $Q_W = -73.20(13)$. This value differs from our measured value by 2.5σ. A comparison of our values of Q_W and the standard model prediction is shown in Fig. 6.1.

Assuming that the difference from the standard model is not due to an experimental error or a statistical fluctuation, it suggests several possibilities. The first is that there is some very perverse feature of the calculated electronic wave functions and the γ^5 operator that causes errors in the calculation of this matrix element to be much larger than for directly measurable matrix elements. In this case, our assumption that the standard deviation of the values in Table 6.1 represents the accuracy of $k_{\rm PNC}$ is wrong. The second is that there are contributions or corrections to atomic PNC within the standard model that have been overlooked. We see no justification for either of these possibilities, but they clearly need to be explored further. The first offers a formidable but not overwhelming challenge to both theoretical and experimental atomic physicists.

The final possibility is that the discrepancy is indicative of the presence

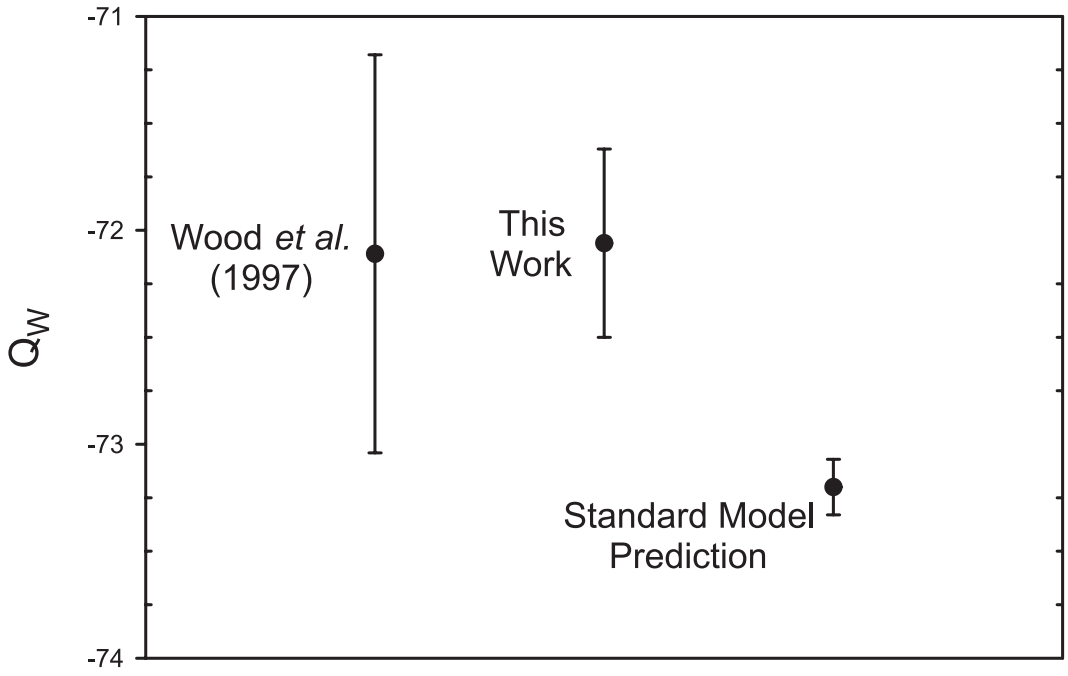

Figure 6.1: A comparison of values from Ref. [13], this work, and the standard model. The difference between this work and the standard model is 2.5σ.

of some new physics not contained in the standard model. Physics that would be characterized by the S parameter is not a likely candidate because the size of the contribution needed ($S = -1.44(35)_{\rm expt}(46)_{\rm theory}$) would be in conflict with other data [6]. However, there are other types of new physics, such as an additional Z boson, that would be consistent all other current data. For example, there is a theory that predicts the existence of an extra Z_χ boson [67] with a mass given by

$$\Delta Q_W({}^{55+N}_{55}\mathrm{Cs}) \simeq 0.4(2N+55)\frac{m_W^2}{m_{Z_\chi}^2}. \tag{6.4}$$

Using our value of Q_W this theory predicts $m_{z_\chi} = 692(29)$ GeV/c^2. The possibility that this theory—or other theories like it [69, 70, 71, 72, 73]—is correct also needs to be explored further.

CHAPTER 7

CONSIDERATIONS FOR FUTURE EXPERIMENTS

The implications of atomic parity nonconservation for the standard model depend on both experiments and theory. The present work lessens the dependence of the test of the standard model on the theory, but does not eliminate it. If the re-evaluation of the uncertainty in the theory stands up to scrutiny, and if the calculated value of the PNC matrix elements does not change significantly with further refinement of the theory, then atomic PNC reveals a need for extensions to the standard model.

It is worthwhile to consider improvements in the experiments. Therefore, this chapter explores ways that the measurement presented in Refs. [13, 23] might be improved. There are three approaches I have studied: reduce (or eliminate) the effect of the largest systematic errors, increase the signal-to-noise ratio to reduce the amount of time it takes to reach a given precision, or make another measurement using the same technique on the so-called "α" transition. Section 7.1 describes a method that can be used to make the $6S \rightarrow 7S$ line shape symmetric and thus eliminate or reduce many of the systematic errors that are enhanced by an asymmetric line shape. Section 7.2 details an experiment on transversely cooling the atomic beam to increase the signal-to-noise ratio. Section 7.3 discusses repeating the PNC measurement using the "α" transition.

7.1 Cavity Sidebands

7.1.1 Experimental Idea

Without the high-finesse Fabry-Perot etalon, the PNC measurement presented in Refs. [13, 23] would not have been possible. The increase in laser power inside the cavity makes it possible to drive very weak transitions with high signal-to-noise ratios. The standing-wave nature of the laser field inside the etalon does have one large drawback: a spatially-varying ac Stark shift due to the sinusoidal variation of laser intensity.

Because the intensity inside the cavity is proportional to $\sin ky$, atoms crossing through the laser beam at different positions suffer from different size ac Stark shifts. Furthermore, atoms that have a nonzero transverse velocity see a changing intensity and thus experience a varying ac Stark shift. The spatially varying ac Stark shift causes the asymmetry and broadening in the spectral lines of the $6S \rightarrow 7S$ transition as discussed in Ref. [30]. The asymmetry couples with other effects such as $E1$-$M1$ interference to produce PNC systematic errors. If the asymmetry can be eliminated, some of the most troublesome systematic errors could also be eliminated.

Because the asymmetry comes directly from the spatially varying laser intensity, if we could make the intracavity power uniform, the asymmetry would be eliminated. This can be accomplished by phase modulating the laser light incident upon the PBC at the free spectral range of the PBC. The following discussion will show how this is possible.

A phase modulated laser field of the form $\epsilon = A\cos[(\omega t - \delta \sin \omega_m t)]$ can also be written in terms of Bessel functions as [74]

$$\begin{aligned} \epsilon = A[J_0(\delta)\cos\omega t &+ J_1(\delta)\cos(\omega-\omega_m)t - J_1(\delta)\cos(\omega+\omega_m)t \\ &+ J_2(\delta)\cos(\omega-2\omega_m)t + J_1(\delta)\cos(\omega+2\omega_m)t], \end{aligned} \tag{7.1}$$

where terms involving Bessel functions higher than order two are neglected. Presented in this form it is easy to see that the phase modulation at ω_m puts sidebands on the laser that are separated from the main frequency by integer multiples of ω_m. The size of the sidebands relative to the carrier with a modulation index of $\delta = 1.2045$ is shown in Fig. 7.1.

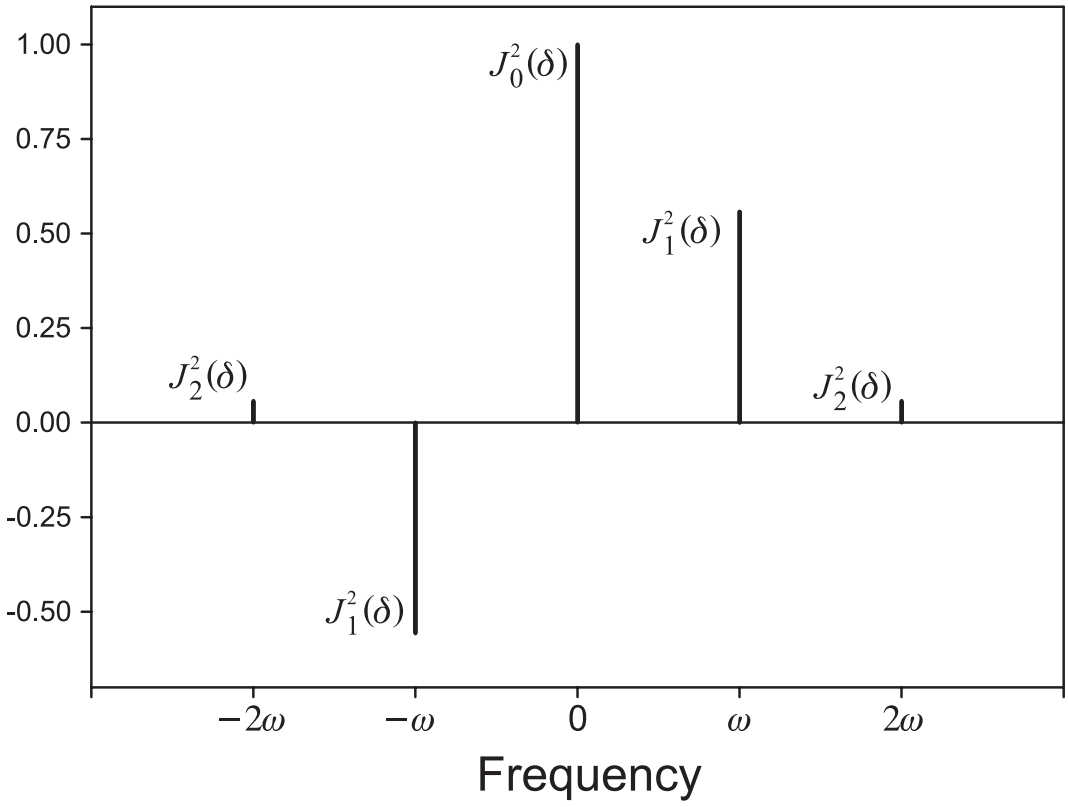

Figure 7.1: Relative sizes of phase modulation sidebands with $\delta = 1.2045$. The height of each line indicates the amount of power in each sideband relative to the carrier $[J_0^2(\delta)]$. A negative height indicates a 180° phase shift with respect to the other sidebands.

If the laser field is incident on a perfectly stable Fabry-Perot etalon with a free spectral range $\omega_{\mathrm{FSR}} = 4\pi\ell/c$, where ℓ is the cavity length, and if $\omega_m = \omega_{\mathrm{FSR}}$, then Appendix C shows that the standing wave inside the etalon is given by

$$\begin{aligned}\epsilon = A[2J_0(\delta)\sin ky \sin \omega t &+ 2J_1(\delta)(\sin k_+ y \sin \omega_+ t - \cos k_- y \sin \omega_- t) \\ &+ 2J_2(\delta)(\sin k_{--} y \sin \omega_{--} t + \sin k_{++} y \sin \omega_{++} t)],\end{aligned} \tag{7.2}$$

where $\omega_\pm \equiv \omega \pm \omega_m$, $\omega_{\pm\pm} \equiv \omega \pm 2\omega_m$ and so on. If the natural lifetime of an atom is long compared to both ω and ω_m, and $A = 1/\sqrt{2}$, then the atom "sees" a time averaged intensity given by

$$\begin{aligned}I = \sin^2 ky[J_0^2(\delta) &+ 2J_1^2(\delta)\cos 2k_m y + 2J_2^2(\delta)\cos 4k_m y] \\ &+ 2[J_1^2(\delta)\sin^2 k_m y + J_2^2(\delta)\sin^2 2k_m y].\end{aligned} \tag{7.3}$$

When $\delta = 0$, there is no phase modulation and the intensity is simply $I = \sin^2 kz$. This is exactly the situation discussed in Ref. [30] that gives rise to a spatially varying ac Stark shift and asymmetric line shapes. When $\delta \neq 0$, there is still the $\sin^2 kz$ term. Now, however, that term is multiplied by a much more slowly spatially varying term that depends on k_m. In addition, there is a term that does not have the fast $\sin^2 kz$ dependence. The result is a rapidly spatially varying intensity superimposed on a more uniform profile. The envelope of the rapidly varying part is shown in Fig. 7.2. The question now is what effect will this have on the ac Stark shift and on the $6S \rightarrow 7S$ transition rate for each atom?

The size of the ac Stark shift depends on the detuning of the laser light from allowed transitions such as the $6S_{1/2} \rightarrow 6P_{3/2}$ transition. The detuning of the carrier from this transition is approximately 2×10^8 MHz, and the first side band is only different by 500 MHz, which is 2.5×10^{-6} of the carrier detuning. For the purposes of the ac Stark shift, the sideband and the carrier are indistinguishable. Thus, the ac Stark shift depends on the time average of the sidebands and the carrier combined.

Conversely, the strength of the $6S \rightarrow 7S$ transition depends on the laser detuning from the $6S \rightarrow 7S$ resonance. Therefore, the carrier is on resonance, but

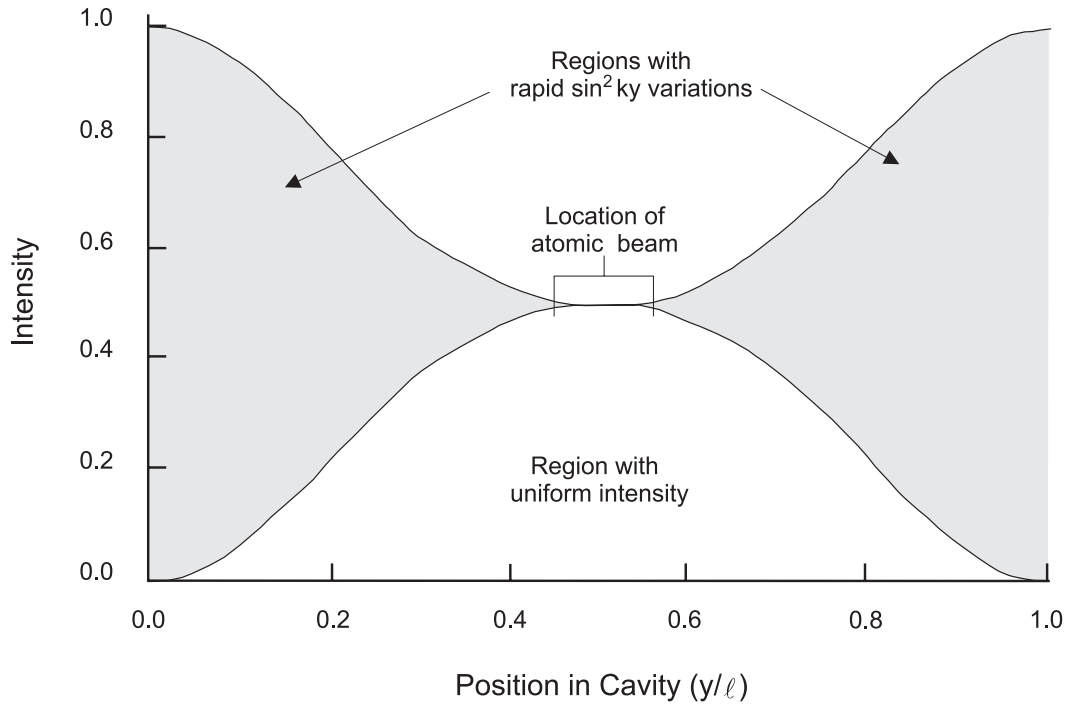

Figure 7.2: A plot showing the intensity of the laser light inside the PBC as a function of position in the cavity when the incident light is phase modulated at the free spectral range of the PBC. The intensity is the sum of two terms: one that varies rapidly with position ($\sin^2 ky$) and one that varies slowly (trigonometric functions of $k_m y$.) Close to either end of the cavity the intensity varies rapidly, but near the center where the atomic beam intersects the laser beam, the intensity is very close to uniform.

the sidebands are well detuned (~ 100,) from resonance. Thus, the strength of the $6S \rightarrow 7S$ transition depends on the time average of only the carrier. The result is that we can eliminate the spatial dependence of the ac Stark shift at the expense of a factor of two in signal size.

7.1.2 Experimental Implementation

In order to put sidebands on the light inside the PBC we borrowed a home-built electro-optic modulator (EOM) from Dr. John Hall's laboratories. We drive the EOM using a tunable frequency synthesizer. The EOM has a resonant frequency of 503 MHz and is tunable from 489 MHz to 518 MHz. The resonant frequency is

very sensitive to temperature, so any attempt to make permanent use of the EOM must include temperature stabilization. For the purpose of demonstrating the effect of the sidebands, temperature stabilization is not needed. In its usual configuration, the free spectral range of the PBC is slightly larger than 518 MHz, so during this experiment the input mirror of the PBC is mounted on a modified optical mount as shown in Fig. 7.3.

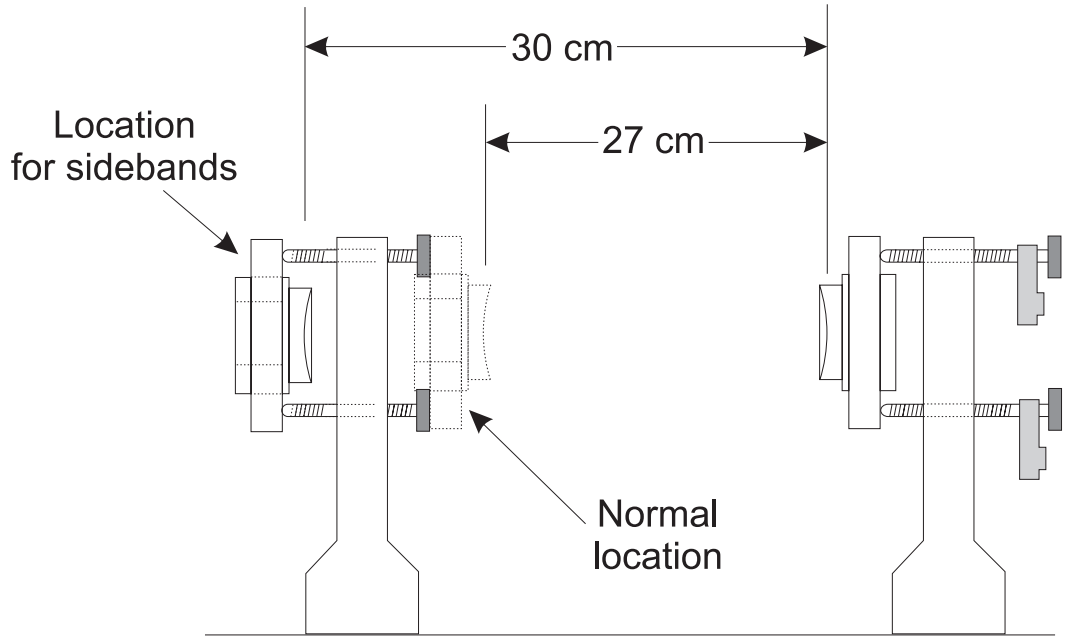

Figure 7.3: Under normal conditions, the length of the PBC is 27 cm. In order to change the free spectral range of the PBC to match the resonant frequency of the EOM used to phase modulate the dye laser the input mirror has to be moved in front of its mount to make the cavity length 30 cm.

To monitor the sidebands on the dye laser we place a scanning Fabry-Perot etalon after the PBC and use it as a spectrum analyzer. The amount of power in the sidebands is easily monitored using the etalon. The dye laser with sidebands was then simply locked to the PBC using the usual Pound-Drever-Hall scheme.

The asymmetry of the $6S \rightarrow 7S$ line shape is emphasized if the photoionization current on the electric field plates is monitored. Therefore, we connect an electrometer to the field plates during this experiment so we can look at both the probe scattered light and the photoionization line shapes. We use the $6S_{1/2}$ $F = 3$ to $7S_{1/2}$ $F' = 4$ transition for these measurements.

7.1.3 Results

Sample scans over the "β" $6S \rightarrow 7S$ $E1$ transition with and without sidebands are shown in Fig. 7.4. The dramatic reduction of the asymmetry in the line shapes is evident by comparing the pairs of scans. However, a significant reduction in peak signal also occurs. Scans were also taken (unintentionally at first) with the modulation index slightly off the optimum $\delta = 1.0245$. In that case, the peaks of the scans are very sharp and the asymmetry is prominent. It only takes a change in δ of about 1% to begin to see the asymmetry again.

7.1.4 Conclusion

The addition of the sidebands on the dye laser to remove the asymmetry in the line shape of the $6S \rightarrow 7S$ transition can be considered a success, but it is not at all clear that this is a viable solution to the problem of line shape asymmetry for two reasons.

First, the price of having the sidebands to produce a uniform intensity is a factor of two loss in the amount of laser light that is resonant with the $6S \rightarrow 7S$ transition. Losing a factor of two in signal means we need to take twice as much data to get the same uncertainty as before. The whole purpose of the sidebands was to eliminate a major source of systematic error so that we would not have to take as much data. Reducing the resonant intensity by a factor of two does not achieve this goal. If the line shape asymmetry were the limiting systematic the sidebands might be an excellent solution, but that is not the case with the PNC measurement.

Second, putting sidebands on the dye laser is a complicated task. The additional temperature stabilization that would be required, as well as finding some way to determine when the modulation index is correct, would add many complications to an almost hopelessly complicated experiment. So, while the sidebands do make the line shape symmetric, in the end it seems that phase modulating the dye laser is not a modification that we would like to make to a next-generation PNC experiment.

7.2 Improving the Signal-to-Noise Ratio

7.2.1 Increasing Beam Flux

The second way to improve upon the last PNC measurement would be to improve the signal-to-noise ratio. Increasing the signal-to-noise ratio by a factor of n also reduces by a factor of n the amount of time required to reach a given level of precision, since the PNC measurement is shot noise limited.

We investigated the effect of turning up the oven temperature, which should increase the number of atoms in the beam. As shown in Fig. 7.5, the beam size as measured by the probe laser does increase with temperature initially, but at higher temperatures the number of atoms reaching the detection region begins to plateau. A plausible explanation for this effect is that at high temperatures there are so many atoms emerging from the oven nozzle that not all of the atoms pass through the first beam-defining aperture. The result is that a cloud of atoms forms just in front of the oven nozzle and becomes the effective source of the atomic beam. A hotter oven only means a bigger cloud, not a denser beam. Details of such a process are given in Ref. [75].

At approximately 225°C the oven repeatably exhibits behavior we call "crashing": the size of the beam increases by 30 to 50% and then settles to a value 10 to 20% lower than when the temperature was changed. This decreased level then slowly decreases with time. If the oven is turned off, allowed to cool, and turned back

on again, the signal size at a given temperature is lower than before but stable. We cannot explain this behavior, but it gives us an upper limit for the oven temperature.

Another drawback of a very dense atomic beam is that the efficiency with which the optical pumping lasers spin-polarize the atomic beam decreases as the density of the atomic beam increases. Data showing this effect are shown in Fig. 7.6. At low beam flux, the spin-polarization is near 98%, but as the beam size is increased, the spin-polarization drops off significantly. Future PNC experiments using this apparatus will rely on highly spin-polarized samples of atoms, so an increase in the density of the atomic beam that causes a reduction in the degree of spin-polarization is undesirable.

7.2.2 Transversely Cooling the Atomic Beam

7.2.2.1 Experimental Concept

An alternative to simply increasing the number of atoms in the beam is to transversely cool the atomic beam to decrease its divergence and to increase the number of atoms available for making the $6S \rightarrow 7S$ transition. However, the techniques normally used to cool atoms do so by making the hot atoms scatter many photons and thus dissipate energy. If we were to use the same techniques in the PNC experiment, a significant portion of those scattered photons would be scattered back along the beam where they can be absorbed by atoms that have already been spin-polarized. The result is a subsequent depolarization of the beam, which is unacceptable.

In 1986 Dallibard and Cohen-Tannoudji [76] published a paper describing the so-called "Dressed-Atom" approach that describes the interaction of atoms with high-intensity standing-wave laser field. In the regime of high intensity, simple pictures of the light-atom interaction (as used in describing Doppler cooling) break down. The dressed atom approach uses the basis states $|i, n\rangle$, where i is either 1 or 2, and n indicates the number of photons in the electromagnetic field. At low laser

intensities these "dressed" states reduce to the normal basis states $|s,n\rangle$, where s represents the ground (g) or excited (e) state of the atom. At high intensities, the states $|1,n\rangle$ and $|2,n\rangle$ are different linear combinations of the $|g,n\rangle$ and $|e,n\rangle$ states. A comparison of the two sets of basis states is shown in Fig. 7.7.

Where the laser intensity is small, the states reduce to the normal $|s,n\rangle$ set. Where the laser intensity is high, the $|i,n\rangle$ basis states must be used, and the energies of these states depend on the intensity. Therefore, in any laser beam (where the intensity profile is, for example, Gaussian) there is a maximum energy shift at the center of the beam. The energy shift gets smaller as the atom moves away from the center. If the atom is in a standing wave, the intensity varies sinusoidally in the longitudinal direction as well as varying as a Gaussian in the transverse direction. This longitudinal variation is shown in Fig. 7.8. In the Dressed-atom picture, atoms moving along a standing wave can be cooled via stimulated emission. Using Fig. 7.8 as a guide, we now describe the idea behind the cooling.

Consider an atom in the $|1,n+1\rangle$ state moving along the standing wave. The probability of this atom making a transition to another state is small in the nodes and large in the anti-nodes. As the atom moves from node to anti-node it loses energy. If it makes a transition at the peak of the anti-node (point A), then that energy loss is permanent. The atom, now in the $|2,n\rangle$ state (point B), again moves along the standing wave. Now, however, the probability of making a transition is large at the nodes and small at the anti-nodes. If the atom again makes a transition (at point C), the energy loss from anti-node to node is again permanent. As the atom moves along the standing wave the process repeats itself (points D and E) and the atom is cooled. More important, since the force due to stimulated emission cooling is much greater than that due to Doppler cooling, many fewer photons are required to do the same amount of cooling and the problem of depolarizing the beam is minimal.

There are two demonstrations of this cooling effect on a cesium atomic beam where the standing wave is detuned from the $6S_{1/2} \rightarrow 6P_{3/2}$ transition. One

experiment [77] uses a high power ring dye laser, and another experiment [78] uses a low power diode laser coupled into a power build-up cavity. In both cases, cooling of atoms with transverse velocities of less than 4 m/s was achieved. However, it was unclear whether the same mechanism could cool atoms with transverse velocities of up to 17 m/s. If this is possible, it may lead to an increased signal-to-noise ratio for the PNC experiment.

7.2.2.2 Horizontal Cooling

In order to utilize transverse cooling of the atomic beam we need a stable, high-power laser and a power build-up cavity into which we can inject the power. We use a Ti:sapphire laser that provides 300 mW of 852 nm light and a cavity constructed of two flat, 1 in diameter mirrors separated by 5 cm. The finesse of the cavity is roughly 40, and the ultimate power density inside is 3.4 W/cm^2. The cavity is placed in the optical pumping region with the optical pumping magnetic field coils removed. Once aligned, the cavity does not creep out of alignment; all that is needed to peak up the power inside the cavity is minor realignment of the input laser beam.

All horizontal collimating elements after the cavity are removed (a vertical-vane collimator and two beam defining apertures) so as many atoms as possible actually reach the detection region. In the two previous references, detection of the velocity distribution is performed using a hot wire detector. The transverse velocity of a group of atoms is inferred from its position in space. In our experiment we detect the atoms by collecting the light scattered by the atomic beam as we sweep the probe laser across the $6S_{1/2} \rightarrow 6P_{3/2}$ transition. The transverse velocity is inferred from the Doppler shift of a particular group of atoms and we use a saturated absorption spectrometer as a reference. In the rest of the chapter the units of velocity are MHz. These may be converted to m/s using the formula $v = \lambda\Delta\nu$, where $\lambda = 852$ nm and $\Delta\nu$ is the Doppler shift.

Our detection method limits our sensitivity to the amount of cooling. Imagine an atomic beam with a Gaussian distribution transverse velocities. If the width of the distribution is 20 MHz FWHM, then we would measure a line width very close to 20 MHz. Now imagine we can cool all the atoms in the beam to zero transverse velocity. A hot wire detector would measure a large signal right near zero velocity; we would measure a line width of about 10 MHz since we are limited by the natural line width of the $6S_{1/2} \rightarrow 6P_{3/2}$ transition.

In order to overcome this limitation, we leave in the first vertical-vane collimator. This allows us to "steer" the beam. Thus, we can move the beam so that the transverse velocities are centered at various Doppler shifts, not necessarily near zero shift. Then, if we cool all the atoms to zero transverse velocity we will see the entire line shape move to zero Doppler shift. Sample uncooled line shapes are shown in Fig. 7.9.

The previous experiments used carefully chosen detunings to optimize their cooling; once we saw evidence of cooling we selected the detuning that appeared to give the "best" effect. The detuning for all the data shown here is $\delta = 48$ MHz $= 9,$, where , is the natural line width of the $6S_{1/2} \rightarrow 6P_{3/2}$ transition. It is possible to study the effects of detuning extensively, but the discussion that follows shows that the exact detuning does not ultimately affect the increase in signal that is possible, so we do not perform this study.

Taking the data for this experiment is almost trivial. Interpreting the data, however, is not. Figures. 7.10 through 7.15 show scans with and without cooling for a variety of collimator positions. In all cases, the effect of the cooling is evident, whether it is a narrowing of the line width (Fig. 7.10) or a significant shift of the atoms toward zero Doppler shift (Fig. 7.15). Also shown in each figure is the difference between the cooled and the uncooled lines showing clearly that atoms are removed from areas with high transverse velocity and placed in areas of low transverse velocity.

In order to quantify the effects of the cooling we would like to be able to look at the number of atoms having a given transverse velocity. That is, we want to know the population distribution (or equivalently, the velocity distribution) of the beam. Since the fluorescence we measure is the convolution of the population distribution with the natural line shape, we should, in principle, be able to deconvolve the population distribution from the fluorescence if we know the natural line shape. In practice this is very difficult because the solution to the deconvolution is not unique.

As an alternative to a deconvolution, we can make an ansatz about the population distribution and then convolute that with the natural line width of the $6P_{3/2} \rightarrow 6S_{1/2}$ transition. We can then use the difference between the line shape prediction of the ansatz and the measured line shape to modify our initial ansatz. Several iterations give good agreement with measured line shape. An example of an initial ansatz and the final population distribution for the data shown in Fig. 7.16. The asymmetry is not surprising because of the probable bias angle in the capillary array as mentioned in the caption of Fig. 7.9. The velocity distribution of the whole atomic beam with no collimation is shown in Fig. 7.17.

Ultimately, we want to know the final velocity distribution of the atomic beam after cooling. To do this, we need to compare the velocity distributions in the beam before and after cooling. So, we perform the iteration discussed for each collimator position. This gives us the velocity distribution for each position before and after cooling. We then ask the question: "What fraction of atoms in a given velocity class is transferred to near the zero transverse velocity class?" The answer gives us the effect of cooling as a function of transverse velocity. The maximum, average, and minimum effects of cooling are shown in Fig. 7.18.

Now that we know what fraction of the atoms with a given transverse velocity will be cooled to near zero transverse velocity, we can determine the population distribution of the whole atomic beam with and without cooling. These data are

shown in Fig. 7.19 The number of atoms with zero transverse velocity increases by about a factor of eight. Clearly the cooling technique is successful at slowing atoms with transverse velocities between 10 MHz and 4 MHz to less than ∼4 MHz.

The net effect of the cooling on the atomic beam is not as dramatic as Fig. 7.19 would suggest, however. The line shapes we would expect if we **measured** the beam and the $6S \rightarrow 7S$ transition are shown in Fig. 7.20. The severe reduction in the improvement of the signal is due to the fact that in the PNC experiment we must always convolve the population distribution with the natural line width of the detection. In addition, the ac Stark broadening [30] will broaden the $6S \rightarrow 7S$ transition regardless of cooling, and this effect is not shown in the figures. The variation in intensity in the radial direction of the dye laser is unavoidable, and the variation of the intensity along the laser due to the standing wave can only be eliminated if we sacrifice a factor of two in power, as discussed in Section 7.1. We estimate the reduction in the benefit of cooling by the ac Stark shift is 50%, which limits the improvement in the $6S \rightarrow 7S$ signal size to a factor of 1.5.

7.2.2.3 Vertical Cooling

It is important to remember here that the previous discussion is relevant only for cooling in the horizontal direction. For the vertical direction, the natural line widths are not important. What is important is the total number of atoms interacting with the dye laser that is driving the $6S_{1/2} \rightarrow 7S_{1/2}$ transition. For this analysis we assume that we can cool the beam perfectly in the vertical direction.

First, the relative number of atoms emerging from a long thin tube at an angle θ is given approximately by [75]

$$N(\theta) = 1.00978 - 0.85898\theta - 0.09489\theta^2 + 0.15163\theta^3. \tag{7.4}$$

The capillary array in the oven nozzle can be thought of as many infinitely thin tubes

stacked one upon another. The total number of atoms coming out of a vertical slice in the array is then given by

$$N_{\text{Total}} = 2\int_0^{\pi/2} N(\theta)d\theta \times 5 \text{ mm.} = 6.35. \tag{7.5}$$

This is simply twice the sum of all the atoms with trajectory angles from 0 to 90° times the height of the array. The total number of atoms in an uncooled beam intersecting the dye laser beam is given by

$$N^{\text{Hot}}_{\text{Intersect}} = 2\int_{-2.5\text{mm}}^{2.5\text{mm}} N\left(\text{Sin}^{-1}(|x|/260\text{mm})\right) dx \times 1\text{mm} = 0.5. \tag{7.6}$$

This is twice the contribution from each of the infinitely thin tubes in one half of the array that are a distance x from the middle of the array that reach the laser beam 26 cm away. If we can perfectly collimate the beam, then all the N_{Total} atoms will be compressed into the height of the array. The number of atoms intersecting the beam will be

$$N^{\text{Cooled}}_{\text{Intersect}} = \frac{\text{height of laser}}{\text{height of array}} \times N_{\text{Total}} = \frac{1\text{mm}}{5\text{mm}} \times 6.35 = 1.27 \tag{7.7}$$

In this case, we gain the ratio of

$$\frac{N^{\text{Cooled}}_{\text{Intersect}}}{N^{\text{Hot}}_{\text{Intersect}}} = 2.54. \tag{7.8}$$

7.2.3 Conclusion

The best improvement we can get by cooling is approximately a factor of 1.5 in the horizontal direction and a factor of 2.54 in the vertical direction giving a factor of 3.8 total improvement. This assumes that the ac Stark shift [30] only reduces the improvement in horizontal cooling by 50% and that we can cool the beam perfectly in the vertical direction. This seems to be an overly optimistic situation.

Further, attempts to increase the beam flux by increasing the oven temperature are counter productive.

The bottom line is that, while we get approximately eight times more atoms within a ± 4 MHz Doppler width, the largest improvement in signal on the $6S \rightarrow 7S$ transition will be about a factor of three. With only this marginal improvement, a second measurement of PNC using the same technique as Refs. [13, 23] is not attractive.

7.3 Prospects for Further Parity Nonconservation Measurements

Equation (2.26) shows the quantity measured in the recent PNC measurement [13, 23]. In that experiment we measure the interference between a PNC electric dipole amplitude and the "β" Stark-induced electric dipole transition. This experiment provides the value $\mathrm{Im}(E_{\mathrm{PNC}})/\beta$. A similar experiment that uses the "α" Stark-induced amplitude from Eq. (2.13) can provide the value $\mathrm{Im}(E_{\mathrm{PNC}})/\alpha$. This would be a useful quantity to measure because it would provide another determination of the quantity $\mathrm{Im}(E_{\mathrm{PNC}})$ as well as providing a consistency check of the past measurements of $\mathrm{Im}(E_{\mathrm{PNC}})/\beta$ and α/β [25]. Perhaps the most important reason to make a measurement of $\mathrm{Im}(E_{\mathrm{PNC}})/\alpha$ is that we could check the value of the nuclear anapole moment determined in Ref. [13]. However, there are several problems that bring the feasibility of such an experiment into question.

The measurement of $\mathrm{Im}(E_{\mathrm{PNC}})/\beta$ is performed on both the $F = 3$ to $F' = 4$ and $F = 4$ to $F' = 3$ $6S \rightarrow 7S$ transitions. When using the $\Delta F = +1$ ($\Delta F = -1$) transition, the $F = 4$ ($F = 3$) hyperfine state is depleted. Atoms making the $6S \rightarrow 7S$ transition repopulate the $F = 4$ ($F = 3$) state where they are detected using the $6S_{1/2}F = 4$ to $6P_{3/2}F' = 5$ ($6S_{1/2}F = 3$ to $6P_{3/2}F' = 2$) cycling transition. These detection schemes are favorable because 75% (67%) of the atoms making the $6S \rightarrow 7S$ transition repopulate the proper detection state.

However, the measurement of $\mathrm{Im}(E_{\mathrm{PNC}})/\alpha$ is performed on the $\Delta F = 0$

transitions. Here only 33% (24%) of the atoms excited to the $F' = 3$ ($F' = 4$) state end up in the proper $F = 4$ ($F = 3$) state where they can be detected. So, attempting a measurement of $\mathrm{Im}(E_{\mathrm{PNC}})/\alpha$ starts with a signal-to-noise ratio more than a factor of $\sqrt{2}$ smaller than that of the already-difficult measurement of $\mathrm{Im}(E_{\mathrm{PNC}})/\beta$.

Another consideration is the problem of fractional populations alluded to in the discussion of Eq. (2.26). The previous measurement of PNC in cesium used a spin-polarized atomic beam with roughly 98% of the atoms in a single extreme m_F sublevel. Equation (2.26) included detuning factors d_{m_F}, which indicate the relative importance of transitions that are detuned from the main transition because of the Zeeman effect. The largest of the detuning factors is 0.845, while the smallest is 0.127. The effect of these factors is to reduce the precision with which we need to know the populations of the m_F levels.

On the $\Delta F = 0$ transitions the Zeeman effect does not resolve transitions from different m_F sublevels because the g-factors for hyperfine levels with the same F are equal. (See Fig. 2.1.) The result is that all the detuning factors in the "α" analog of Eq. (2.26) are unity. For the $\mathrm{Im}(E_{\mathrm{PNC}})/\beta$ measurement we only needed to measure the populations to 1% to have an uncertainty of 0.1% in the final measurement; for a measurement of $\mathrm{Im}(E_{\mathrm{PNC}})/\alpha$ that requirement becomes an order of magnitude more severe. We would need to measure the populations to 0.1% to have 0.1% in the final measurement. At present, our ability to measure the populations is 0.1 to 0.2%. In order to be comfortably below the uncertainty required, a much better modeling of the optical pumping processes that we use to spin polarize the beam would have to be accomplished.

Further, while one would not expect a measurement of $\mathrm{Im}(E_{\mathrm{PNC}})/\alpha$ to take the more than 15 years that the measurement of $\mathrm{Im}(E_{\mathrm{PNC}})/\beta$ took, a considerable amount of time (perhaps two graduate student lifetimes) would be needed to find and eliminate all the systematic errors that will inevitably plague the new measurement.

These three considerations make a measurement of $\mathrm{Im}(E_{\mathrm{PNC}})/\alpha$ using a

spin-polarized atomic beam an unlikely next step.

7.4 Summary

The previous 0.35% measurement of PNC in atomic cesium is a notable achievement that, when combined with the 0.3% measurement of β and the re-evaluation of the *ab initio* theory, provides a 0.6% test of the standard model. As with any measurement with this importance, a confirming experiment is always comforting. However, it does not seem feasible to make another measurement of PNC using the present methods, whether it is a measurement of $\mathrm{Im}(E_{\mathrm{PNC}})/\beta$ or $\mathrm{Im}(E_{\mathrm{PNC}})/\alpha$, mainly because of signal-to-noise concerns.

Therefore, the work on parity nonconservation using an atomic beam has come to a conclusion after more than 15 years. Future work may involve cold, trapped atoms or measurements on a chain of isotopes to eliminate the need for the atomic theory calculations.

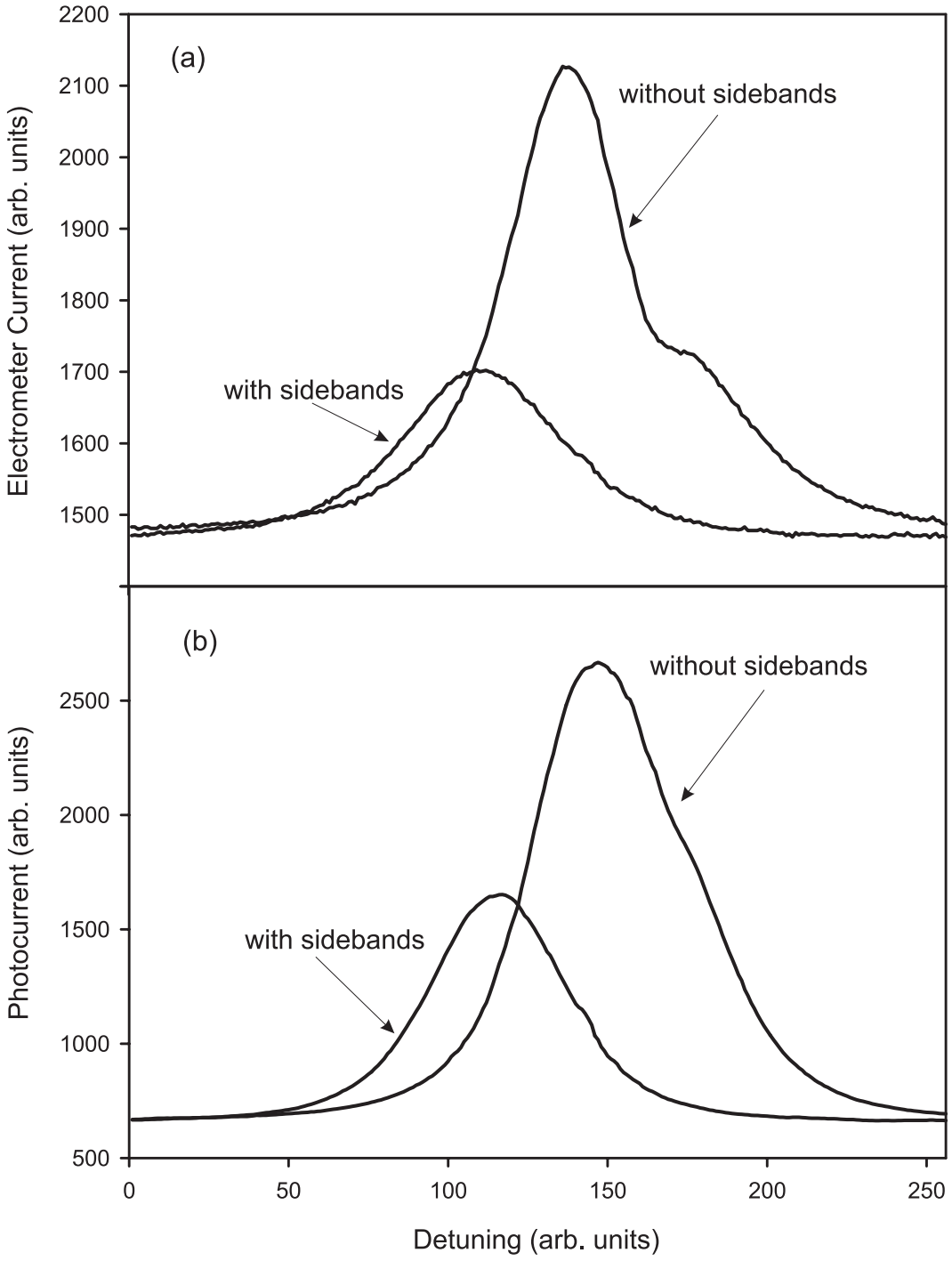

Figure 7.4: Sample scans over the "β" $6S \rightarrow 7S$ $E1$ transition with and without sidebands using (a) photoionization detection and (b) probe detection. The asymmetry disappears with sidebands, but the peak signal also drops significantly

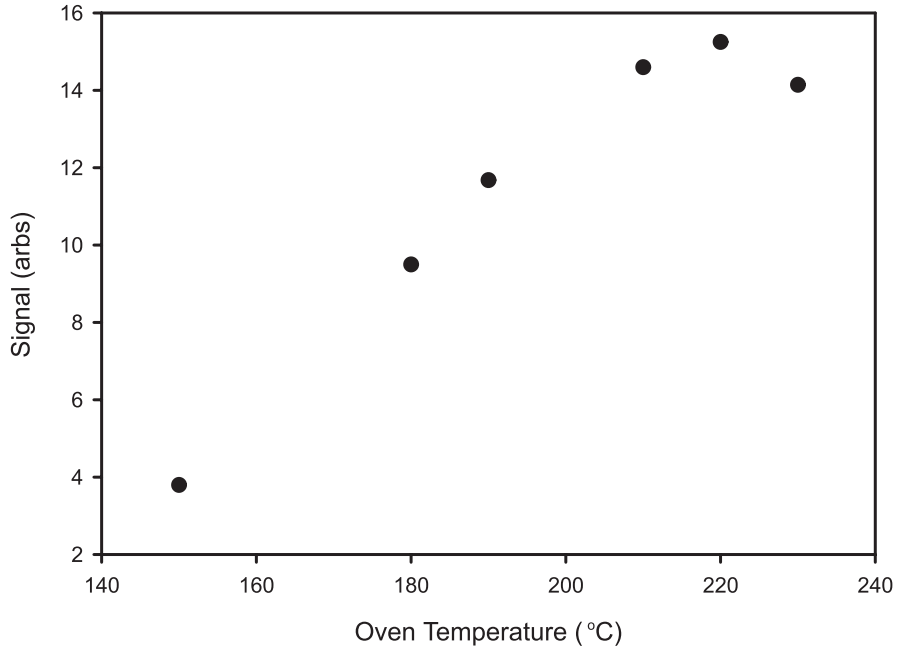

Figure 7.5: This plot shows the size of the atomic beam as a function of the oven temperature. A "saturation" effect at higher temperatures can be seen, as well as evidence of an oven "crash" at about 225°C.

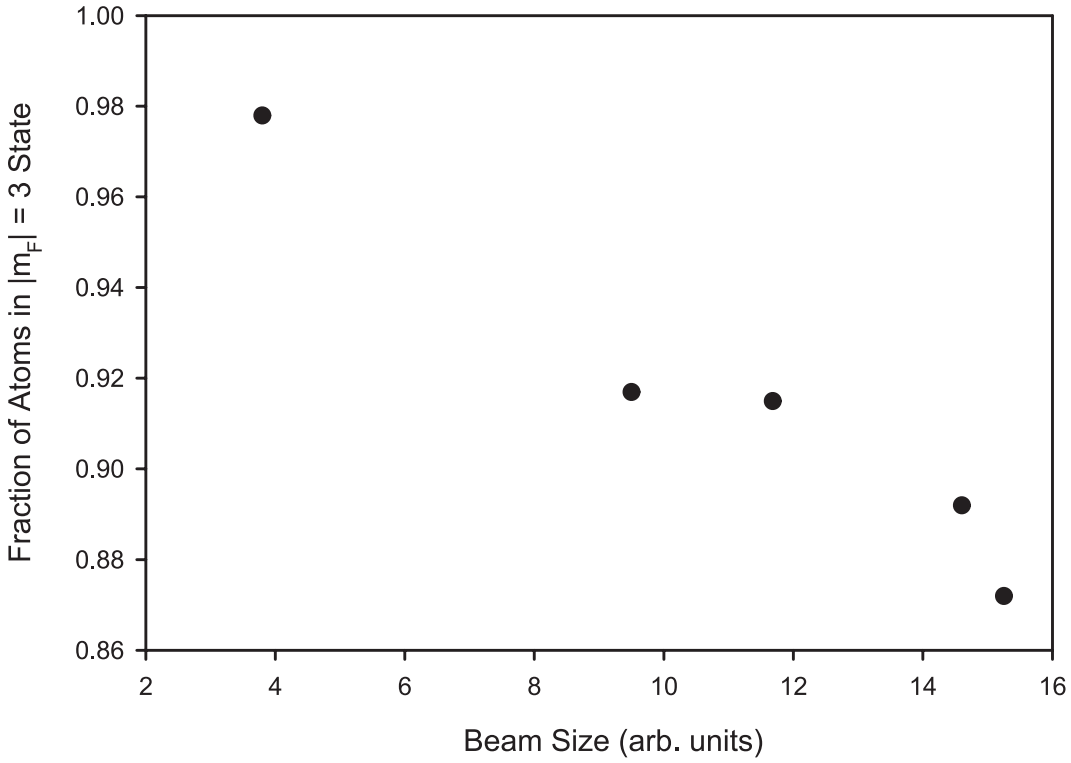

Figure 7.6: This plot shows the spin polarization as a function of the size of the atomic beam. Significant deterioration of the spin-polarization at large beam sizes is obvious.

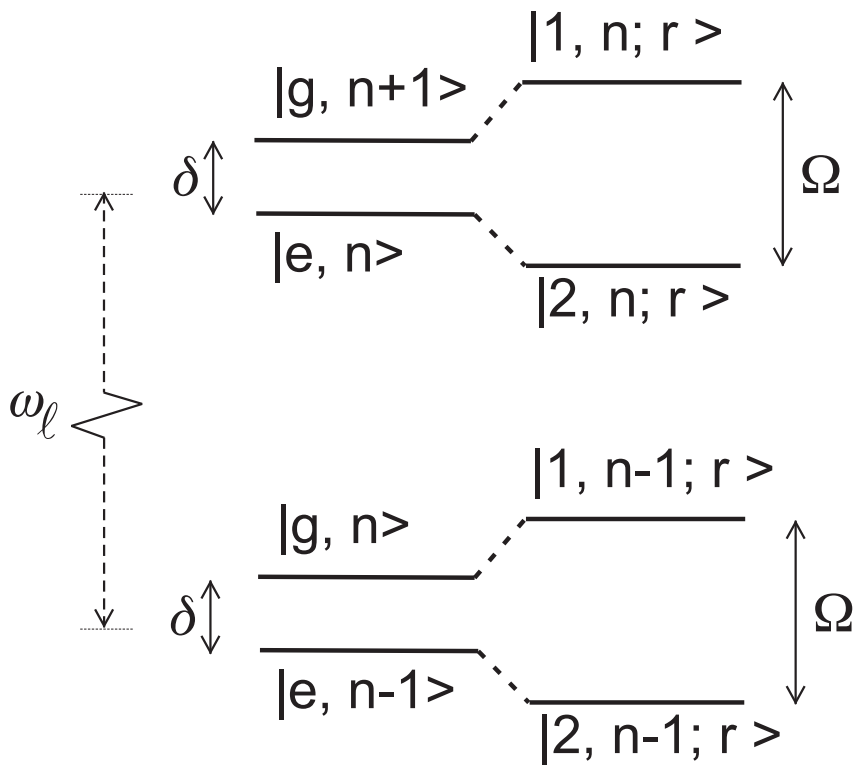

Figure 7.7: The bare and dressed states of an atom in an intense standing-wave laser field. Here δ is the detuning of the laser from the $|g\rangle$ to $|e\rangle$ transition, g and e are ground and excited states, n is the number of photons in the laser field, ω_ℓ is the frequency of the laser, 1 and 2 are linear combinations of the g and e states, and Ω is the generalized Rabi frequency.

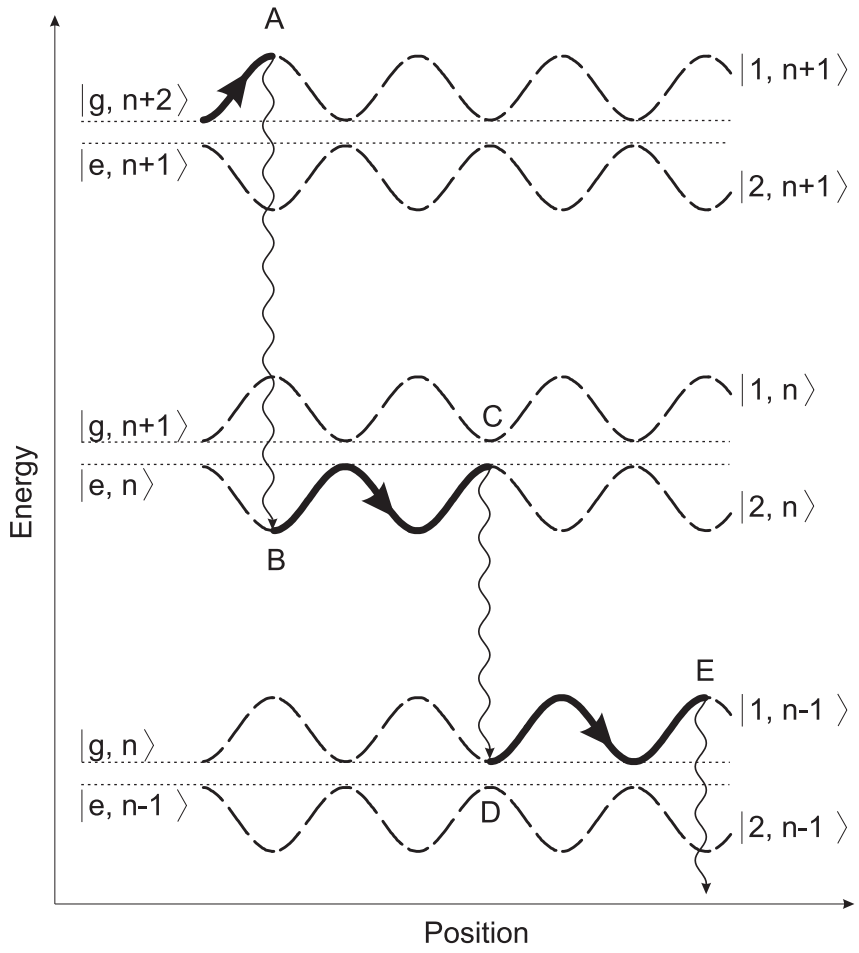

Figure 7.8: The energy levels of an atom in an intense standing-wave field. The atoms starts in $|1, n+1\rangle$ and ends in $|1, n-1\rangle$ and is cooled by losing energy as it moves from troughs to peaks and then moves to a different state.

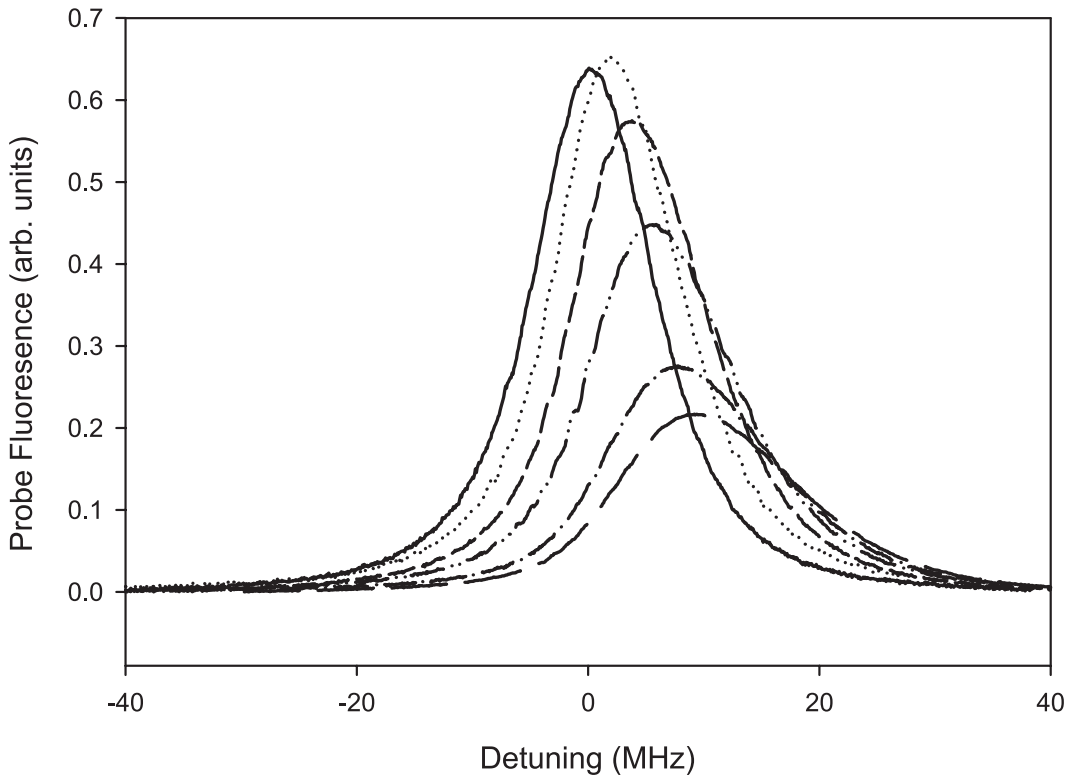

Figure 7.9: Doppler profiles of the atomic beam with no cooling at various collimator positions. The fact that the line with the largest signal is slightly offset from zero detuning indicates that the capillary array in the oven nozzle is slightly tilted.

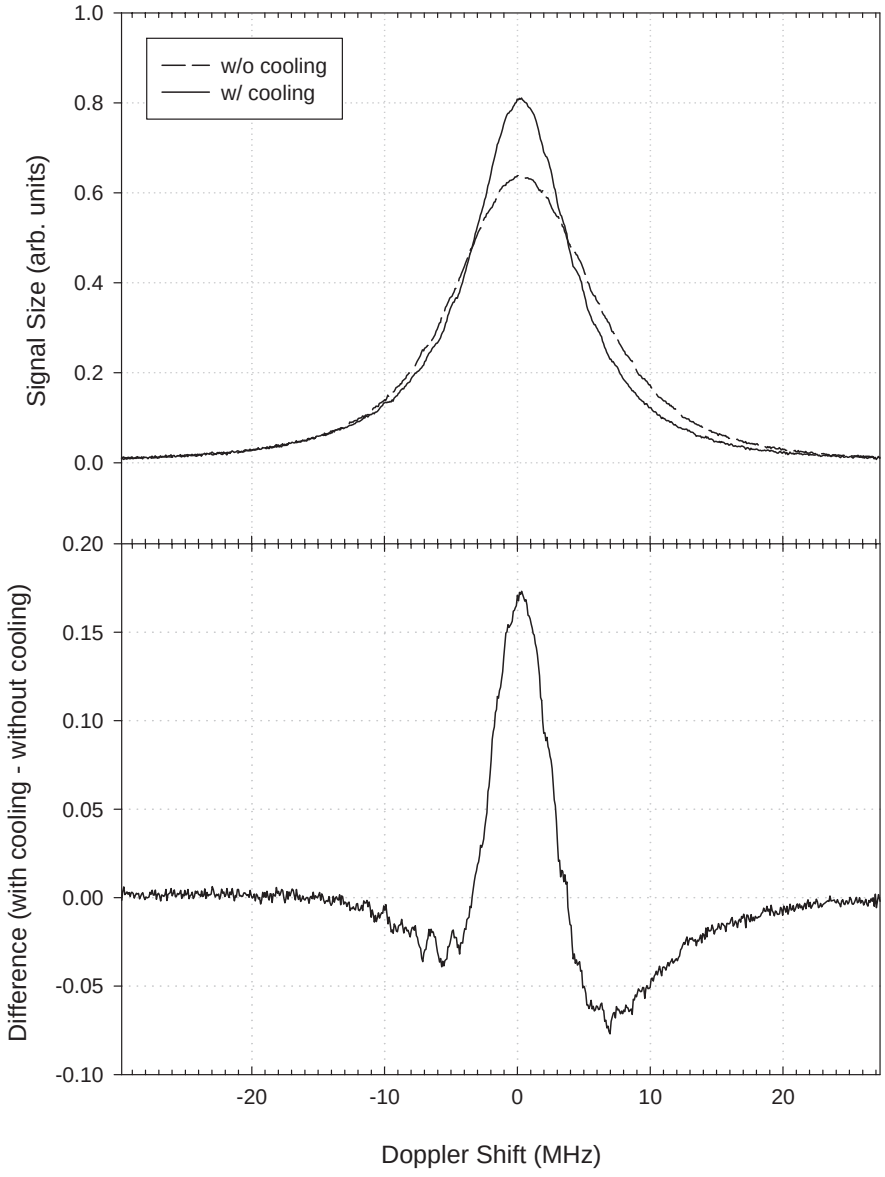

Figure 7.10: Data showing the atomic beam without cooling with transverse velocity centered at 0.6 MHz. Also shown is the cooled beam and the difference between the scans with without cooling.

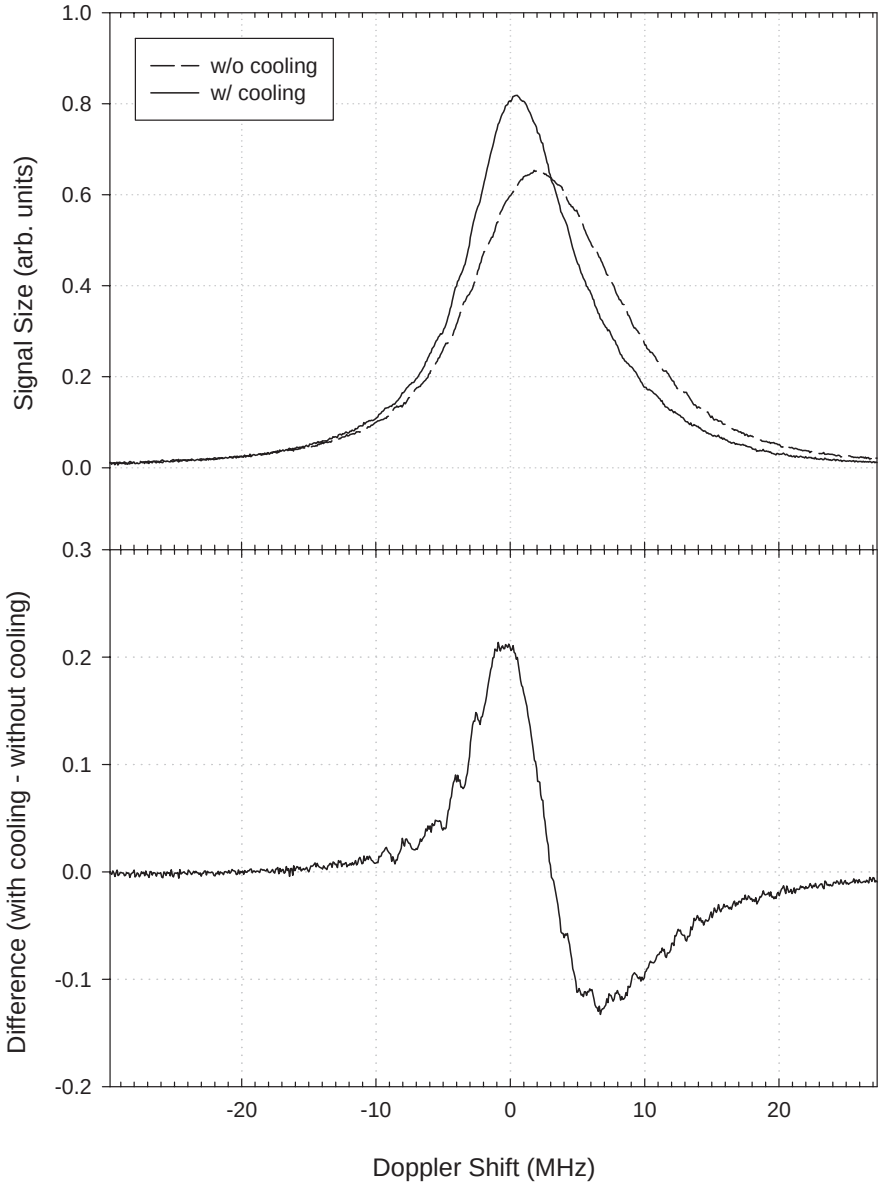

Figure 7.11: Data showing the atomic beam without cooling with transverse velocity centered at 3.1 MHz. Also shown is the cooled beam and the difference between the scans with and without cooling.

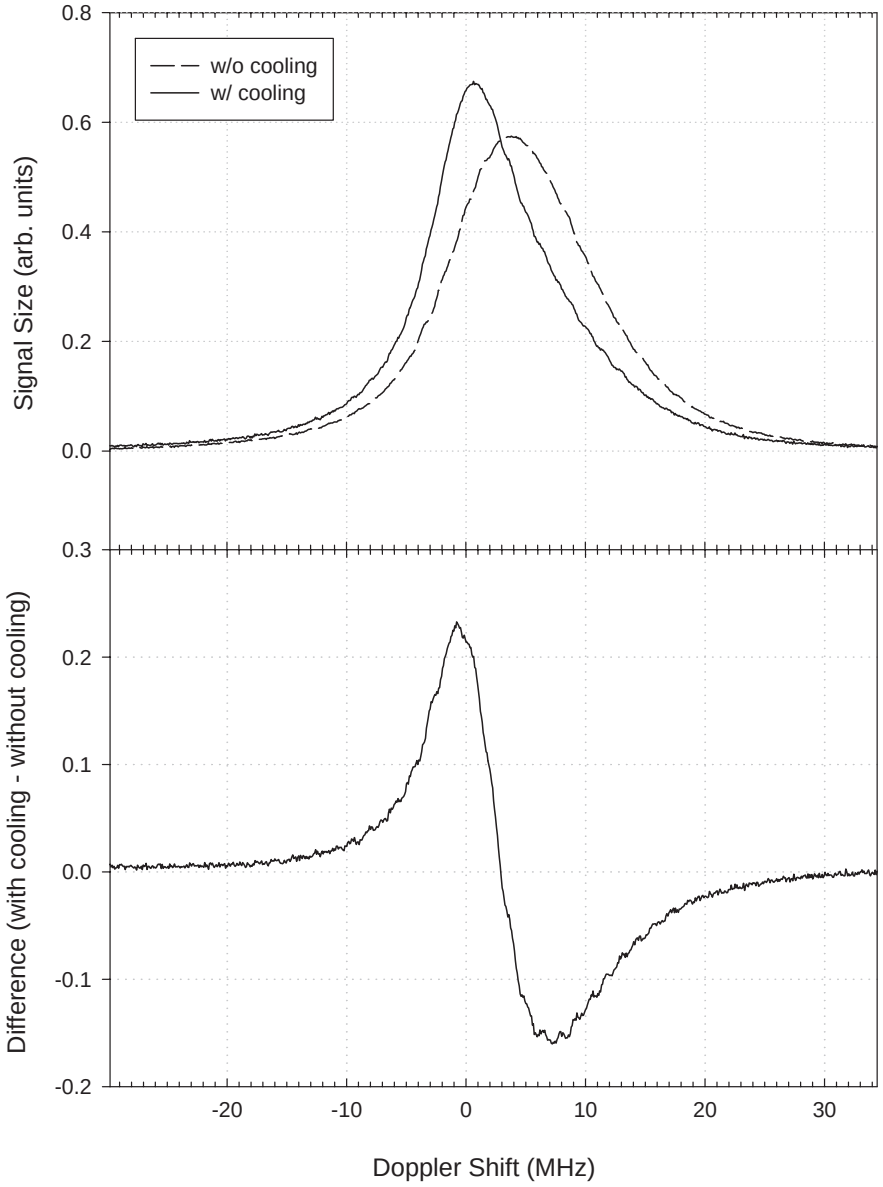

Figure 7.12: Data showing the atomic beam without cooling with transverse velocity centered at 5.5 MHz. Also shown is the cooled beam and the difference between the scans with and without cooling.

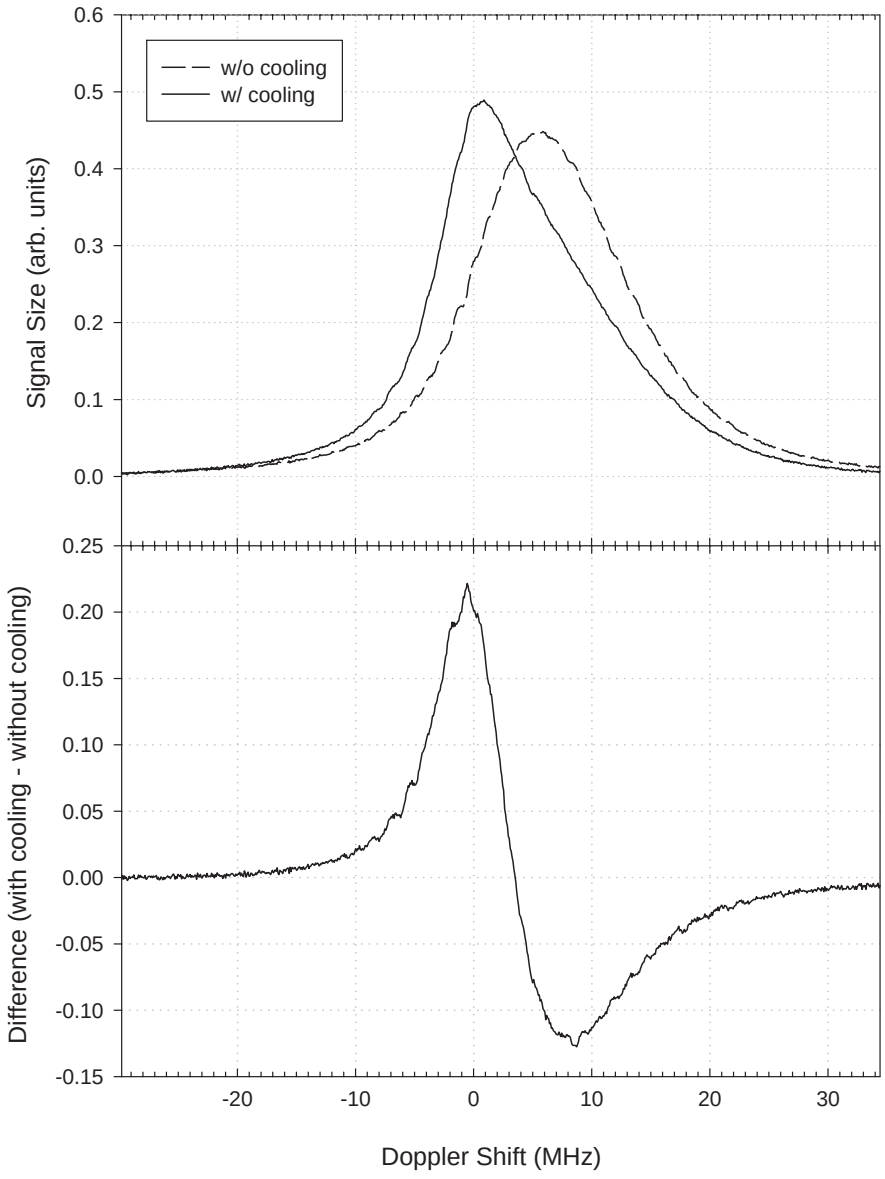

Figure 7.13: Data showing the atomic beam without cooling with transverse velocity centered at 7.9 MHz. Also shown is the cooled beam and the difference between the scans with and without cooling.

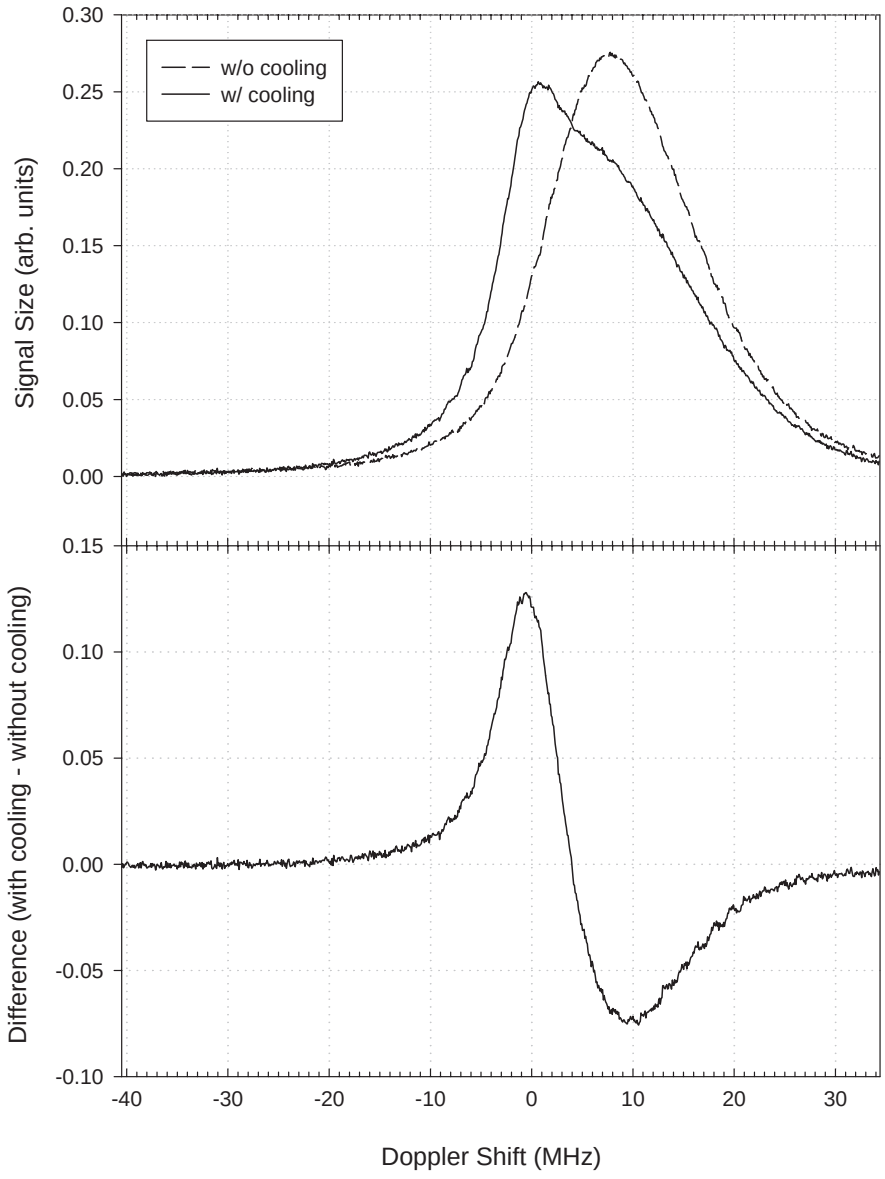

Figure 7.14: Data showing the atomic beam without cooling with transverse velocity centered at 10.3 MHz. Also shown is the cooled beam and the difference between the scans with and without cooling.

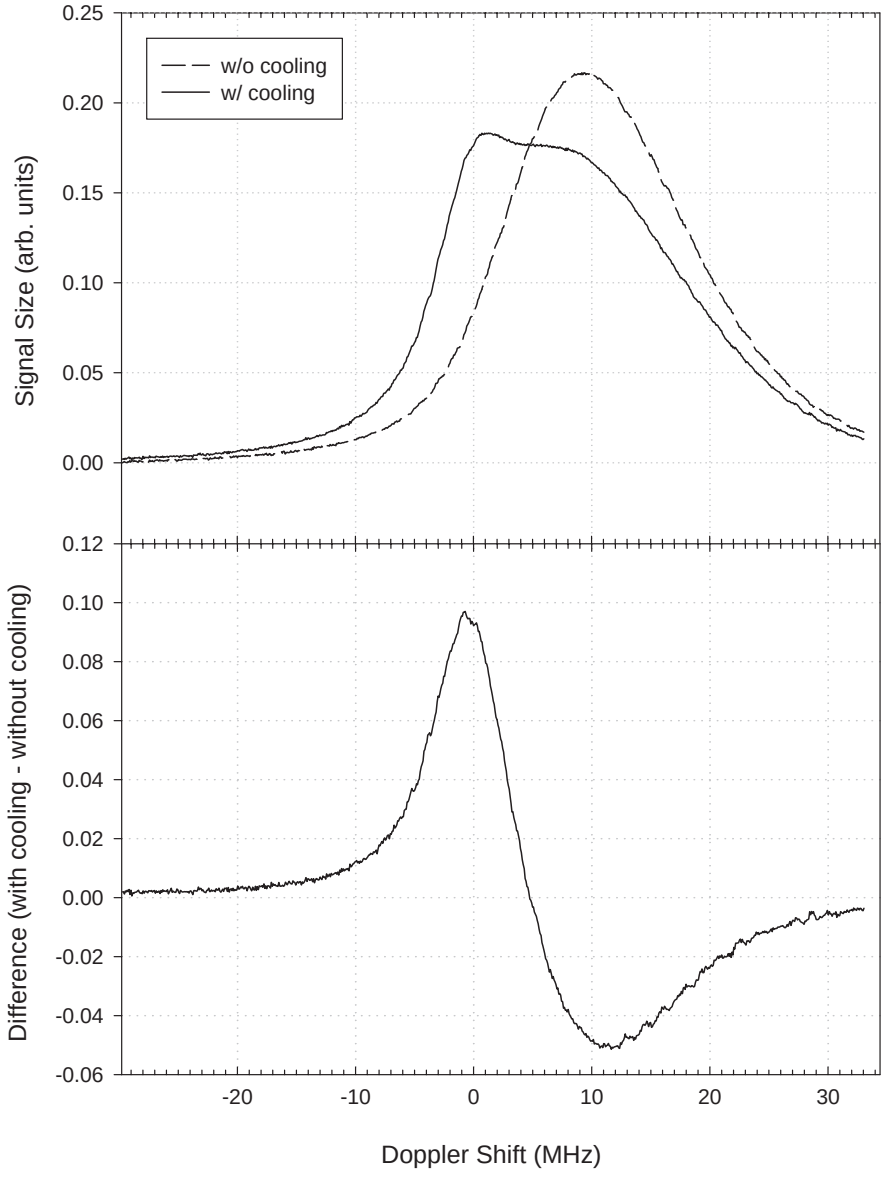

Figure 7.15: Data showing the atomic beam without cooling with transverse velocity centered at 12.3 MHz. Also shown is the cooled beam and the difference between the scans with and without cooling.

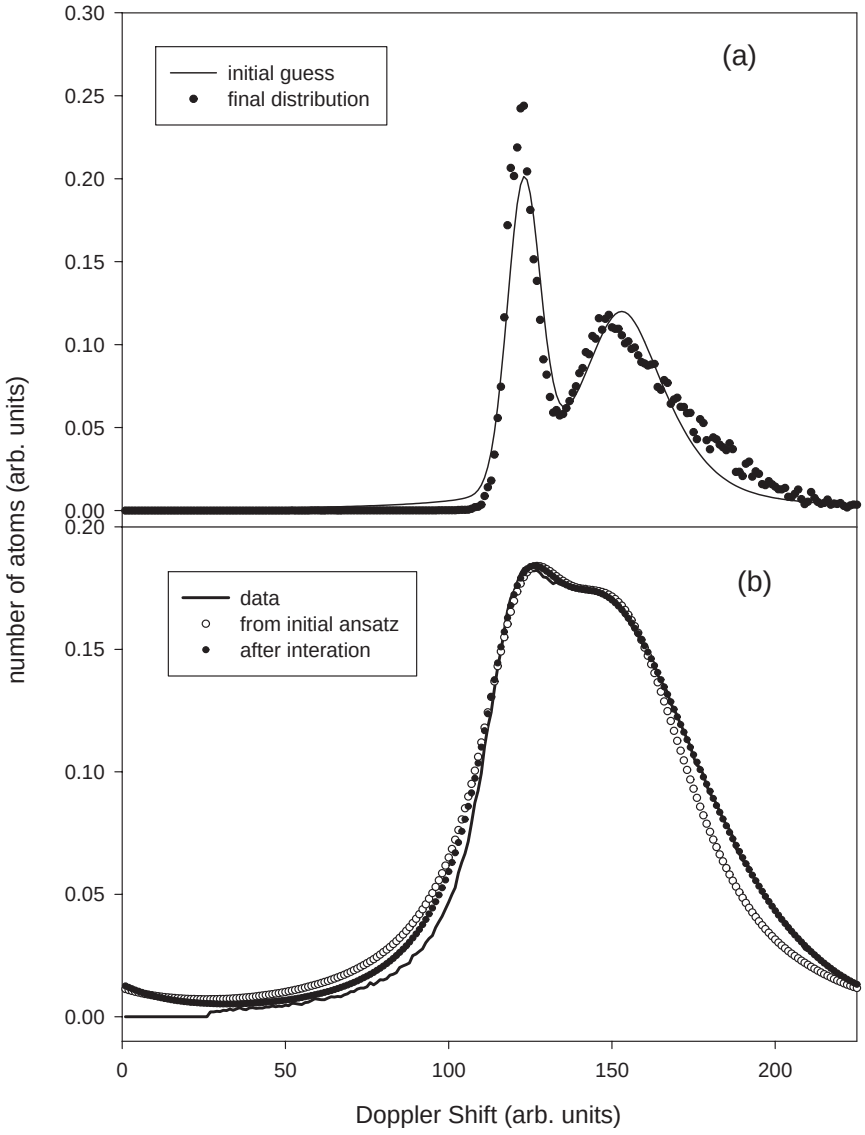

Figure 7.16: Determination of the velocity distribution within the atomic beam using the convolution of an ansatz with a natural line width. Plot (a) shows the initial and final estimates of the velocity distribution, while plot (b) compares the predicted line shape of these two estimates with the measured line shape. The data shown used a total of 14 iterations to arrive at the final ansatz. This number of iterations was used in all the analyses.

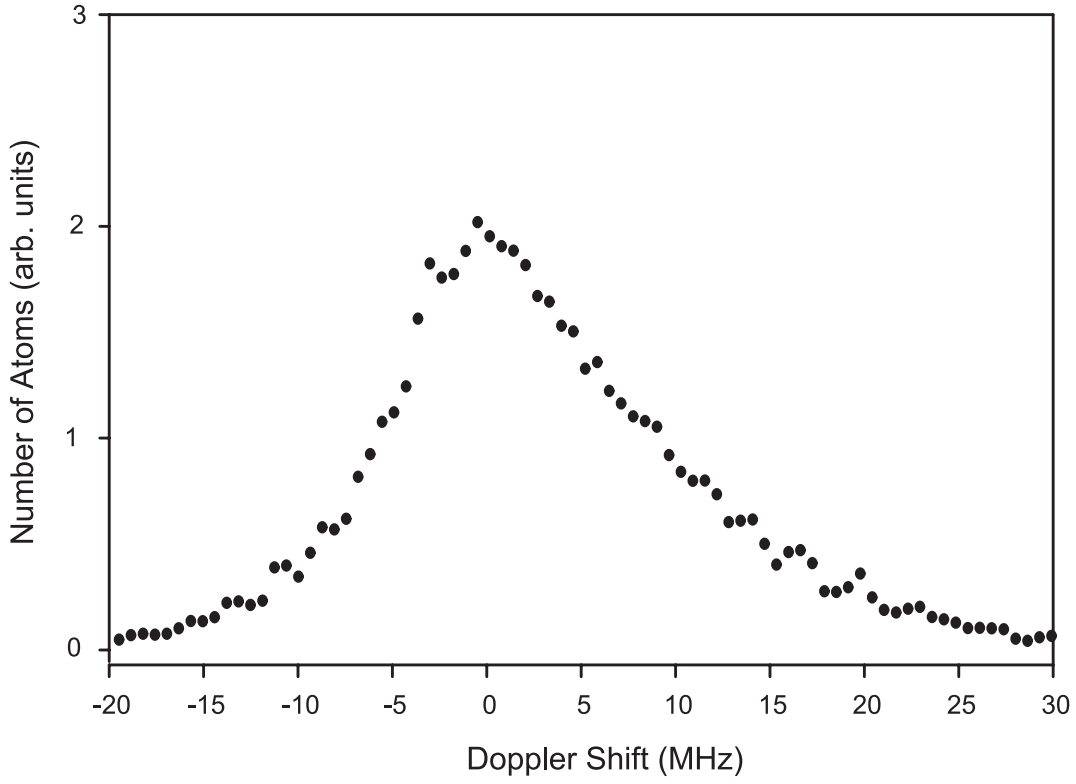

Figure 7.17: The velocity distribution of the atomic beam determined using the iterative procedure discussed above.

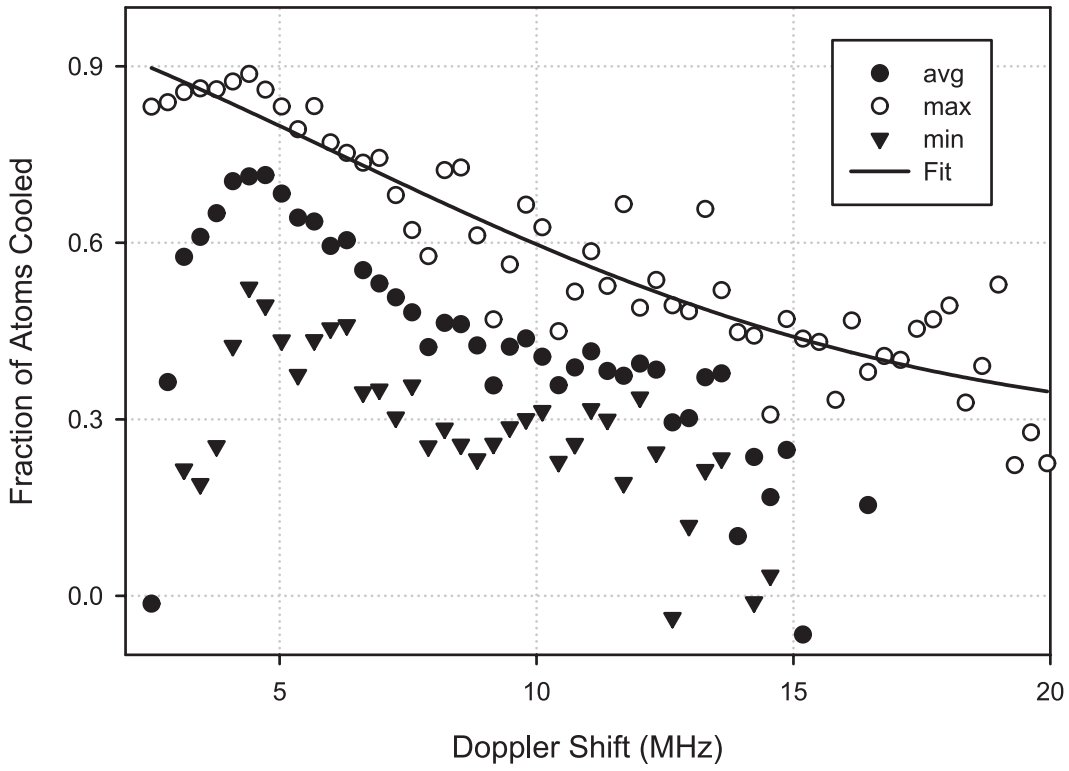

Figure 7.18: The minimum, average, and maximum fractional cooling effect as a function of Doppler shift. We fit to the maximum effect because that is the most likely effect we can achieve with optimization of detuning, laser power, etc.

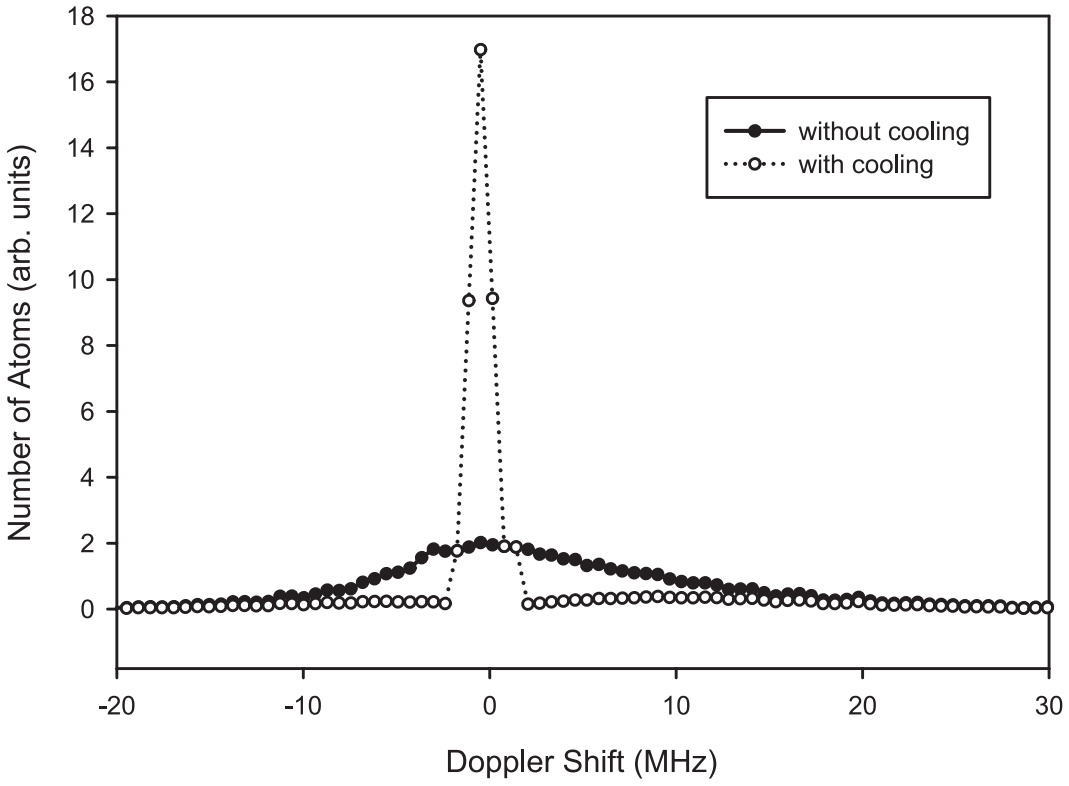

Figure 7.19: Population distribution of the atomic beam with and without cooling. The distribution without cooling was obtained using the iterative convolution technique discussed above. The distribution with cooling was obtained by using the distribution without cooling and the fractional effect of cooling derived from the data in Figs 7.10 through 7.15

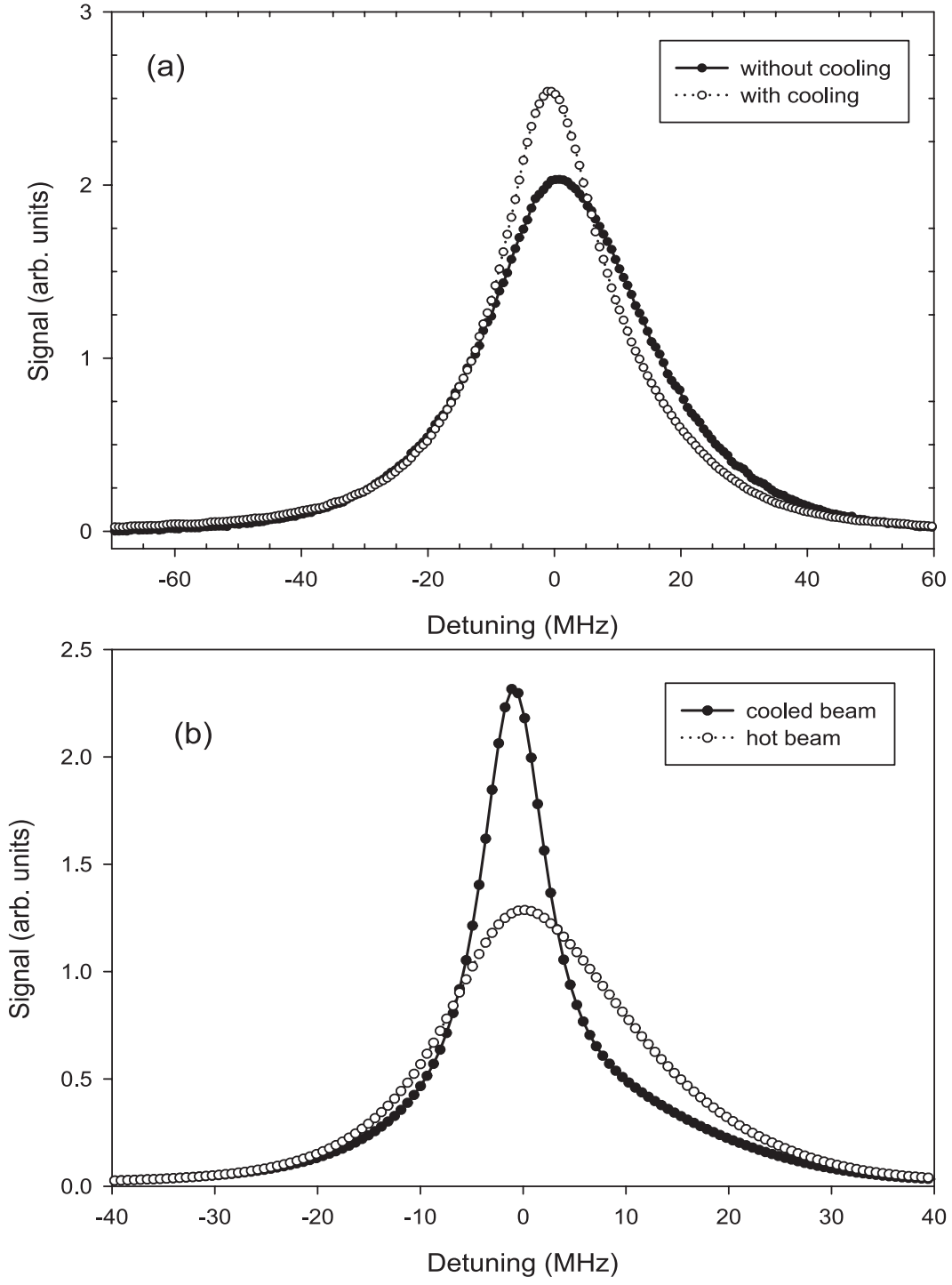

Figure 7.20: The line shapes for the (a) atomic beam and (b) the $6S \rightarrow 7S$ transition. The improvement from transverse cooling in signal size is not as dramatic as for these line shapes as it was for the velocity distribution. This is because the limitations of the natural line widths plays an important role.

BIBLIOGRAPHY

[1] E. Noether, Nachrichten Gesell. Wissenschaft. Gottingen **2,** 235 (1918).

[2] C. S. Wu *et al.*, Phys. Rev. **105,** 1413 (1957).

[3] S. L. Glashow, Nucl. Phys. **22,** 579 (1961).

[4] A. Salam, in **Elementary Particle Theory: Relativistic Groups and Analyticity (8th Nobel Symp.)**, N. Svartholm, ed., (Almquist and Wicksell, Stockholm, 1968).

[5] S. Weinberg, Phys. Rev. Lett. **19,** 1264 (1967).

[6] M. E. Peskin, "Electroweak reconciliation," Science **281,** 1153 (1998).

[7] M. A. Bouchiat and C. Bouchiat, "Parity violation induced by weak neutral currents in atomic physics. Part I," J. Phys. (Paris) **35,** 899 (1974).

[8] M. A. Bouchiat and C. Bouchiat, "Parity violation induced by weak neutral currents in atomic physics. Part II," J. Phys. (Paris) **36,** 493 (1975).

[9] D. M. Meekhof, P. Vetter, P. K. Majumder, S. K. Lamoureaux, and E. N. Fortson, "High-precision measurement of parity nonconserving optical rotation in atomic lead," Phys. Rev. Lett. **71,** 3442 (1993).

[10] R. B. Warrington, C. D. Thompson, and D. N. Stacey, "A new measurement of parity nonconserving optical rotation at 648 nm in atomic bismuth," Europhys. Lett. **24,** 641 (1993).

[11] N. H. Edwards, S. J. Phipp, P. E. G. Baird, and S. Nakayama, "Precise measurement of parity nonconserving optical rotation in atomic thallium," Phys. Rev. Lett. **74,** 2654 (1995).

[12] P. A. Vetter, D. M. Meekhof, P. K. Majumder, S. K. Lamoreaux, and E. N. Fortson, "Precise test of electroweak theory from a new measurement of parity nonconservation in atomic thallium," Phys. Rev. Lett. **74,** 2658 (1995).

[13] C. S. Wood, S. C. Bennett, D. Cho, B. P. Masterson, J. L. Roberts, C. E. Tanner, and C. E. Wieman, "Measurement of parity nonconservation and an anapole Moment in Cesium," Science **275,** 1759 (1997).

[14] S. A. Blundell, J. Sapirstein, and W. R. Johnson, "High-accuracy calculation of parity nonconservation in cesium and implications for particle physics," Phys. Rev. D **45,** 1602 (1992).

[15] V. A. Dzuba, V. V. Flambaum, and O. P. Sushkov, "Summation of the high orders of perturbation theory for the parity nonconserving E1-amplitude of the 6S-7S Transition in the Caesium Atom," Phys. Lett. A **141,** 147 (1989).

[16] G. Kane, **Modern Elementary Particle Physics** (Addison Wesley, New York, 1993).

[17] C. Caso *et al.*, "1998 Review of particle physics," Euro. Phys. J. **C3,** 1 (1998).

[18] G. K. Woodgate, **Elementary Atomic Structure** (Oxford University Press, New York, 1980).

[19] C. Cohen-Tannoudji, B. Diu, and F. Laloë, **Quantum Mechanics** (John Wiley and Sons, New York, 1977).

[20] S. L. Gilbert, **Parity Violation in Atomic Cesium and Associated Experiments**, Ph.D. thesis, University of Michigan, 1984.

[21] M. C. Noecker, **Precision Measurement of Parity Nonconservation in Atomic Cesium**, Ph.D. thesis, University of Michigan, 1988.

[22] B. P. Masterson, **Prospects for Measuring Parity Nonconservation in an Optically-Pumped Cesium Beam**, Ph.D. thesis, University of Colorado, 1991.

[23] C. S. Wood, **High Precision Atomic Parity Nonconservation Measurement Using a Spin-Polarized Cesium Beam and the Nuclear Anapole Moment of ^{133}Cs**, Ph.D. thesis, University of Colorado, 1996.

[24] V. A. Dzuba, V. V. Flambaum, and O. P. Sushkov, "polarizabilities and parity nonconservation in the Cs atom and limits on the deviation from the standard electroweak model," Phys. Rev. A **56,** 4357 (1997).

[25] D. Cho, C. S. Wood, S. C. Bennett, J. L. Roberts, and C. E. Wieman, "Precision measurement of the ratio of scalar to tensor transition polarizabilities for the cesium 6S-7S transition," Phys. Rev. A **55,** 1007 (1997).

[26] V. V. Flambaum, I. B. Khriplovich, and O. P. Sushkov, "g-Factor anomalies and strongly forbidden M1 transitions in heavy atoms," Phys. Lett. **67A,** 177 (1978).

[27] M. A. Bouchiat and J. Guéna, "The E2 6S-7S amplitude in cesium and its importance in a precise calibration of $E1_{PV}$," J. Phys. (Paris) **49,** 2037 (1988).

[28] S. L. Gilbert, B. P. Masterson, M. C. Noecker, and C. E. Wieman, "Precision measuement of the off-diagonal hyperfine interaction," Phys. Rev. A **34,** 3509 (1986).

[29] C. Bouchiat and C. A. Piketty, "Magnetic dipole and electric quadrupole amplitudes induced by the hyperfine interaction in the cesium 6S-7S transition and the parity violation calibration," J. Phys. (Paris) **49,** 1851 (1988).

[30] C. E. Wieman, M. C. Noecker, B. P. Masterson, and J. Cooper, "Asymmetric line shapes for weak transitions in strong standing-wave fields," Phys. Rev. Lett. **58,** 1738 (1987).

[31] M. C. Noecker, B. P. Masterson, and C. E. Wieman, "Precision measurement of parity nonconservation in atomic cesium: A low-energy test of the electroweak theory," Phys. Rev. Lett. **61,** 310 (1988).

[32] R. W. P. Drever, J. L. Hall, F. V. Kowalski, J. Hough, G. M. Ford, A. J. Munley, and H. Ward, "Laser phase and frequency stabilization using an optical resonator," Appl. Phys. B **31,** 97 (1983).

[33] N. M. Sampas, **A Ring Laser Gyroscope with Optical Subtraction**, Ph.D. thesis, University of Colorado, 1990.

[34] S. L. Gilbert and C. E. Wieman, "Easily constructed high-vacuum valve," Rev. Sci. Instrum. **53,** 1627 (1982).

[35] K. B. MacAdam, A. Steinbach, and C. Wieman, "A narrow-band tunable diode laser system with grating feedback, and a saturated absorption spectrometer for Cs and Rb," Am. J. Phys. **60,** 1098 (1992).

[36] R. G. Brewer and E. L. Hahn, "Coherent two-photon processes: Transient and steady-state cases," Phys. Rev. A **11,** 1641 (1975).

[37] P. M. Radmore and P. L. Knight, "Population trapping and dispersion in a three-level system," J. Phys. B 15 (1982).

[38] A. Aspect, E. Arimondo, R. Kaiser, N. Vansteenkiste, and C. Cohen-Tannoudji, "Laser cooling below the one-photon recoil energy by velocity selective coherent population trapping: theoretical analysis," J. Opt. Soc. Am. B **6,** 2112 (1989).

[39] J. Dalibard and C. Cohen-Tannoudji, "Laser cooling below the Doppler limit by polarization gradients: simple theoretical models," J. Opt. Soc. Am. B **6,** 2023 (1989).

[40] R. J. Rafac, C. E. Tanner, A. E. Livingston, and H. G. Berry, "Fast-beam laser liftime measurements of the cesium $6p^2P_{\frac{1}{2},\frac{3}{2}}$ states," to be published (1998).

[41] S. L. Gilbert, R. N. Watts, and C. E. Wieman, "Hyperfine structure measurement of the 7S state of cesium," Phys. Rev. A **27,** 581 (1983).

[42] E. Arimondo, M. Inguscio, and P. Violino, "Experimental determinations fo the hyperfine structure in the alkali atoms.," Rev Mod. Phys. **49,** 31 (1977).

[43] S. A. Blundell, W. R. Johnson, and J. Sapirstein, "High-accuracy calculation of the $6S_{1/2}$-$7S_{1/2}$ parity-nonconserving transition in atomic cesium and implications for the standard model," Phys. Rev. Lett. **65,** 1411 (1990).

[44] S. A. Blundell, W. R. Johnson, and J. Sapirstein, "Third-order many-body perturbation theory calculations of the ground-state energies of cesium and thallium," Phys. Rev. A **42,** 3751 (1990).

[45] S. A. Blundell, W. R. Johnson, and J. Sapirstein, "Relativistic all-order calculations of energies and matrix elements in cesium," Phys. Rev. A **43,** 3407 (1991).

[46] V. A. Dzuba, V. V. Flambaum, P. G. Silvestrov, and O. P. Sushkov, "Relativistic many-body calculations in atoms and parity Violation in Caesium," J. Phys. B **18,** 597 (1984).

[47] V. A. Dzuba, V. V. Flambaum, and O. P. Sushkov, "Summation of the high orders of perturbation theory in the correlation correction to the hyperfine structure and to the amplitudes of E1-transitions in the caesium atom," Phys. Lett. A **142,** 373 (1989).

[48] V. A. Dzuba, V. V. Flambaum, and O. P. Sushkov, "Summation of the perturbation theory high order contributions to the correlation correction for the energy levels of the caesium atom," Phys. Lett. A **140,** 493 (1989).

[49] R. N. Watts, S. L. Gilbert, and C. E. Wieman, "Precision measurement of the Stark shift of the 6S-7S transition in atomic cesium," Phys. Rev. A **27,** 2769 (1983).

[50] J. R. P. Angel and P. G. H. Sandars, "The hyperfine structure Stark effect: I. Theory," Proc. Roy. Soc. London A **305,** 125 (1968).

[51] L. R. Hunter, D. K. Jr., S. Murthy, and T. W. Sung, "Precision measurement of the Stark shift of the cesium D lines," Phys. Rev. A **37,** 3283 (1988).

[52] H. Gould, E. Lipworth, and M. C. Weisskopf, "Quadratic Stark shift between Zeeman substates in Cs^{133}, Rb^{87}, Rb^{85}, K^{39}, and Na^{23}," Phys. Rev. **188,** 24 (1969).

[53] A. Khadjavi and A. Lurio, "Stark effect in the excited states of Rb, Cs, Cd, and Hg*," Phys. Rev. **167,** 128 (1968).

[54] W. H. Press, B. P. Flannery, S. A. Teukolsky, and W. T. Vetterling, **Numerical Recipies FORTRAN Version** (Cambridge Unviersity Press, New York, 1989).

[55] V. A. Dzuba, private communication.

[56] P. Marte (unpublished).

[57] S. L. Gilbert and C. E. Wieman, "Atomic-beam measurement of parity nonconservation in cesium," Phys. Rev. A **34,** 792 (1986).

[58] C. Bouchiat and C. A. Piketty, "A new method for the evaluation of the parity-violating electric dipole 6S to 7S amplitude in atomic cesium," Europhys. Lett. **2,** 511 (1986).

[59] M. A. Bouchiat and J. Guéna, "The $E_2$6S$\rightarrow$ 7s amplitude in cesium and its importance in a precise calibration of E_1^{pv}," J. Phys. (Paris) **49,** 2037 (1988).

[60] C. W. Oates, K. R. Vogel, and J. L. Hall, "High-precision linewidth measurement of laser-cooled atoms: resolution of the Na $3p^2P_{3/2}$ lifetime discrepancy," Phys. Rev. Lett. **76,** 2866 (1996).

[61] U. Volz, M. Majerus, H. Liebel, A. Schmitt, and H. Schmoranzer, "Precision lifetime measurements on Na I $3p^2P_{1/2}$ and $3p^2P_{3/2}$ by beam-gas-laser spectroscopy," Phys. Rev. Lett. **76,** 2862 (1996).

[62] W. I. McAlexander, E. R. I. Abraham, and R. G. Hulet, "Radiative lifetime of the 2P state of lithium," Phys. Rev. A **54,** R5 (1996).

[63] V. A. Dzuba, V. V. Flambaum, and O. P. Sushkov, "Calculation of energy levels, E1 transition amplitudes and parity violation in francium," Phys. Rev. A **51,** 3454 (1995).

[64] J. E. Simsarian, W. Shi, L. A. Orozco, G. D. Sprouse, and W. Z. Zhao, "$7S_{1/2}$ to $9S_{1/2}$ two-photon spectroscopy of trapped francium," Opt. Lett. **21,** 1939 (1996).

[65] R. J. Rafac and C. E. Tanner, "Measurement of the ^{133}Cs $6p^2P_{3/2}$ state hyperfine structure," Phys. Rev. A **56,** 1027 (1997).

[66] P. Langacker, M. Luo, and K. Mann, "High-precision electroweak experiments: A global search for new physics beyond the standard model," Rev. Mod. Phys. **64,** 87 (1992).

[67] W. J. Marciano and J. L. Rosner, "Atomic parity violation as a probe of new physics," Phys. Rev. Lett. **65,** 2963 (1990).

[68] W. J. Marciano and J. L. Rosner, "Atomic parity violation as a probe of new physics, *eratta*," Phys. Rev. Lett. **68,** 898 (1992).

[69] D. London and J. L. Rosner, "Extra gauge bosons in E_6," Phys. Rev. D **34,** 1530 (1986).

[70] B. W. Lynn and P. G. H. Sandars, "Electroweak radiative corrections to atomic parity nonconservation," J. Phys. B **27,** 1469 (1994).

[71] J. L. Rosner, "Radiative corrections and electroweak observables," Phys. Rev. D **42,** 3107 (1990).

[72] K. T. Mahanthappa and P. K. Mohapatra, "Limits on mixing angle and mass of Z' using $\Delta\rho$ and atomic parity violation," Phys. Rev. D **43,** 3093 (1991).

[73] P. Langacker and M. Luo, "Constraints on additional Z bosons," Phys. Rev. D **45,** 278 (1992).

[74] A. Yariv, **Quantum Electronics** (John Wiley and Sons, New York, 1989).

[75] N. F. Ramsey, **Molecular Beams** (Oxford University Press, Oxford, 1956).

[76] J. Dalibard and C. Cohen-Tannoudji, "Dressed-atom approach to atomic motion in laser light: the dipole force revisited," J. Opt. Soc. Am. B **2,** 1707 (1985).

[77] A. Aspect, J. Dalibard, A. Heidmann, C. Salomon, and C.Cohen-Tannoudji, "Cooling atoms with stimulated emission," Phys. Rev. Lett. **57,** 1688 (1986).

[78] C. E. Tanner, B. P. Masterson, and C. E. Wieman, "Atomic beam collimation using a laser diode with a self-**13,** 357 (1988).

[79] R. N. Zare, **Angular Momentum** (John Wiley and Sons, New York, 1988).

APPENDIX A

$C_{FM}^{F'M'}$ COEFFICIENTS

The coefficients $C_{Fm}^{F'm'}$ are defined by the relation

$$C_{Fm}^{F'm+q} \equiv \left(\frac{1}{\sqrt{2}}\right)^{|q|} \langle F'm+q \mid \sigma_{1q} \mid Fm\rangle \tag{A.1}$$

where $q = 0, \pm 1$, and σ_{1q} are the components of the Pauli spin operator:

$$\sigma_{11} = -\frac{1}{\sqrt{2}}(\sigma_x + i\sigma_y) \qquad \sigma_{1\ -1} = \frac{1}{\sqrt{2}}(\sigma_x - i\sigma_y) \qquad \sigma_{10} = \sigma_z \tag{A.2}$$

and

$$\sigma_x = -\frac{1}{\sqrt{2}}(\sigma_{11} - \sigma_{1\ -1}) \qquad \sigma_y = \frac{i}{\sqrt{2}}(\sigma_{11} + \sigma_{1\ -1}). \tag{A.3}$$

With the rotations given in Section 2.6, we have

$$\sigma_{1\ \pm 1} = \sigma'_{1\ \pm 1} \mp \frac{1}{\sqrt{2}}\left(\frac{B_x}{B} \pm i\frac{B_y}{B}\right)\sigma_{10}. \tag{A.4}$$

The values of the $C_{Fm_F}^{F'm'_F}$ are given by

$$C_{3m}^{4m} = C_{4m}^{3m} = \frac{\sqrt{16-m^2}}{4}, \tag{A.5}$$

$$C_{4m\pm 1}^{4m} = \pm\frac{1}{8}\sqrt{(5 \pm m)(4 \mp m)}, \tag{A.6}$$

$$C^{3m}_{3m\pm1} = \mp\frac{1}{8}\sqrt{(4 \pm m)\,(3 \mp m)}, \tag{A.7}$$

$$C^{3m}_{4m\pm1} = -\frac{1}{8}\sqrt{(4 \pm m)\,(5 \pm m)}, \tag{A.8}$$

$$C^{4m}_{3m\pm1} = \frac{1}{8}\sqrt{(3 \mp m)\,(4 \mp m)} \tag{A.9}$$

$$C^{3m}_{3m} = -\frac{m}{4}, \text{ and} \tag{A.10}$$

$$C^{4m}_{4m} = \frac{m}{4}. \tag{A.11}$$

APPENDIX B

EFFECT OF THE ELECTRIC QUADRUPOLE AMPLITUDE

This appendix gives a detailed treatment of the effects of the electric dipole operator ($E2$) discussed by Bouchiat and Gúena in Ref. [27]. The angular momentum text by Zare [79] is referred to extensively in the discussion, and the notation "Zare (2.45)" means "equation 45 in Chapter 2 from Ref. [79]."

In Ref. [27] Bouchiat and Guéna introduce the phenomenological transition operator

$$\begin{aligned} T(nS{-}n'S) &= -\alpha\vec{E}\cdot\vec{\epsilon} - 2i\beta\vec{S}\times\vec{E}\cdot\vec{\epsilon} + a_1\vec{S}\cdot\vec{\epsilon}\times\vec{k} \\ &+ ia_2(\vec{S}\times\vec{I})\cdot(\vec{\epsilon}\times\vec{k}) + ia_3[(\vec{S}\cdot\vec{\epsilon})(\vec{I}\cdot\vec{k}) + (\vec{S}\cdot\vec{k})(\vec{I}\cdot\vec{\epsilon})], \end{aligned} \tag{B.1}$$

where $a_1 = -2M$, $a_2 = -M_{\rm hf}/2$, and $a_3 = -E2/2$. The first two terms are the Stark-induced amplitudes from Eq. (2.13), the terms proportional to a_1 and a_2 are the magnetic dipole amplitudes from Eq. (2.21), and the term proportional to a_3 is a new amplitude—the electric quadrupole amplitude—caused by the off-diagonal hyperfine mixing of $|nD\rangle$ states into the $|nP\rangle$ states.

In Ref [27] Bouchiat and Guéna re-analyze several different experiments that determine the value of $M_{\rm hf}/M$ and show that the contribution from the $E2$ amplitude is non-negligible in some cases. Specifically, they examine the result of Ref. [28]. In the geometry of that experiment the relevant transition rates $R(F'm_F, Fm_F)$

are given by

$$R(4 \pm 4, 3 \pm 3) = \beta E(a_1 + 4a_2)\left(1 - 3\frac{a_3}{a_1 + 4a_2}\right) \tag{B.2}$$

and

$$R(3 \pm 3, 4 \pm 4) = \beta E(a_1 - 4a_2)\left(1 + 3\frac{a_3}{a_1 - 4a_2}\right) \tag{B.3}$$

Taking the ratio of these two transition rates and inserting the values of the a_i's gives

$$R = \frac{M + M_{\rm hf} - 3E2/4}{M - M_{\rm hf} + 3E2/4}. \tag{B.4}$$

Then

$$\frac{R-1}{R+1} = \frac{M_{\rm hf}}{M}\left(1 - \frac{3}{4}\frac{E2}{M_{\rm hf}}\right). \tag{B.5}$$

Clearly, if $E2/M_{\rm hf}$ is large enough the result is not $M_{\rm hf}/M$. If the contribution from $E2$ to the present measurement of $M_{\rm hf}/\beta$ is similarly non-negligible, then we must make a similar correction.

We now consider $E2$ with the geometry in the present experiment, which is the same as in Ref. [28]: $\vec{E} = E\hat{x}$, $\vec{B} = B\hat{z}$, and $\vec{\epsilon} = \hat{z}$.

The transition operator of concern is

$$\begin{aligned} T_{E2} &= ia_3[(\vec{S}\cdot\vec{\epsilon})(\vec{I}\cdot\vec{k}) + (\vec{S}\cdot\vec{k})(\vec{I}\cdot\vec{\epsilon})] \\ &= ia_3(S_z I_y + S_y I_z). \end{aligned} \tag{B.6}$$

An angular momentum spherical tensor operator of rank one is defined as

$$J_{1,\pm 1} = \mp\frac{1}{\sqrt{2}}(J_x \pm iJ_y) \quad \text{and} \quad J_{1,0} = J_z. \tag{B.7}$$

Equation B.6 can then be written as

$$T_{E2} = -\frac{a_3}{\sqrt{2}}[S_0(I_{+1} + I_{-1}) + (S_{+1} + S_{-1})I_0]. \tag{B.8}$$

The product of two spherical tensor operators is another spherical tensor operator as defined in Zare (5.36):

$$X(k,q) = \sum_{q_1 q_2} \langle k_1 q_1 k_2 q_2 \mid kq \rangle A(k_1, q_1) B(k_2, q_2). \tag{B.9}$$

We can then write down the following components of $X(k,q)$.

$$X(1,\pm 1) = \frac{1}{\sqrt{2}}(\pm S_{\pm 1} I_0 \mp S_0 I_{\pm 1}). \tag{B.10}$$

$$X(2,\pm 1) = \frac{1}{\sqrt{2}}(S_{\pm 1} I_0 + S_0 I_{\pm 1}). \tag{B.11}$$

Then, the products of two spherical tensor operators may be written as

$$S_0 I_{\pm 1} = \frac{\mp 1}{\sqrt{2}}[X(1,\pm 1) \mp X(2,\pm 1)], \text{ and} \tag{B.12}$$

$$S_{\pm 1} I_0 = \frac{\pm 1}{\sqrt{2}}[X(1,\pm 1) \pm X(2,\pm 1)]. \tag{B.13}$$

Thus, we need to find the matrix elements of $S_0 I_{\pm 1} + S_{\pm 1} I_0$:

$$\begin{aligned} &\langle \psi' \mid S_0 I_{\pm 1} + S_{\pm 1} I_0 \mid \psi \rangle \qquad (B.14) \\ &\quad = \frac{1}{\sqrt{2}} \langle \psi' \mid \mp[X(1,\pm 1) \mp X(2,\pm 1)] \pm [X(1,\pm 1) \pm X(2,\pm 1)] \mid \psi \rangle \\ &\quad = \frac{1}{\sqrt{2}} \langle \psi' \mid \mp X(1,\pm 1) \pm X(1,\pm 1) + X(2,\pm 1) + X(2,\pm 1) \mid \psi \rangle \\ &\quad = \sqrt{2}\, \langle \psi' \mid X(2,\pm 1) \mid \psi \rangle. \end{aligned}$$

Thus, we have

$$\langle \psi' \mid T_{E2} \mid \psi \rangle = -a_3 \langle \psi' \mid X(2,1) + X(2,-1) \mid \psi \rangle. \tag{B.15}$$

This matrix element can be evaluated using the formulas Zare(5.64):

$$\langle \gamma j_1 j_2 j m \mid X(k,q) \mid \gamma' j_1' j_2' j' m' \rangle \tag{B.16}$$
$$= (-1)^{j-m} \begin{pmatrix} j & k & j' \\ -m & q & m' \end{pmatrix} \langle \gamma j_1 j_2 j \mid\mid X^k \mid\mid \gamma' j_1' j_2' j' \rangle,$$

and Zare (5.68):

$$\langle \gamma j_1 j_2 j \mid\mid X^k \mid\mid \gamma' j_1' j_2' j' \rangle = [(2j+1)(2j'+1)(2k+1)]^{1/2} \tag{B.17}$$
$$\times \begin{Bmatrix} j_1 & j_1' & k_1 \\ j_2 & j_2' & k_2 \\ j & j' & k \end{Bmatrix} \sum_{\gamma''} \langle \gamma j_1 \mid\mid A^{k_1} \mid\mid \gamma'' j_1' \rangle \langle \gamma'' j_2 \mid\mid B^{k_2} \mid\mid \gamma' j_2' \rangle.$$

For our situation these give

$$\langle 7SIF' m_F' \mid X(k,q) \mid 6SIF m_F \rangle = (-1)^{F'-m_F'} \tag{B.18}$$
$$\times [(2F'+1)(2F+1)(2k+1)]^{1/2} \begin{pmatrix} F' & k & F \\ -m_F' & q & m_F' \end{pmatrix}$$
$$\times \begin{Bmatrix} S & S & 1 \\ I & I & 1 \\ F' & F & k \end{Bmatrix} \sum_{\gamma''} \langle\ 7sS \mid\mid S^1 \mid\mid \gamma'' S \rangle \langle \gamma'' I \mid\mid I^1 \mid\mid 6sI \rangle.$$

Note that in the 3-j symbol we must satisfy the triangle condition with $m_F' - m_F = q$ with $q = \pm 1$. That means we either need the matrix elements of $X(2,+1)$ or of $X(2,-1)$ but never both.

The reduced matrix elements in Eq. (B.18) can be evaluated using the Wigner-Eckart Theorem. The results are

$$\langle 1/2 \mid\mid S^{(1)} \mid\mid 1/2 \rangle = \sqrt{3/2} \quad \text{and} \quad \langle 7/2 \mid\mid I^{(1)} \mid\mid 7/2 \rangle = 3\sqrt{14}. \tag{B.19}$$

We can now use Eq. (B.18) to calculate the relative size of the $E2$ amplitude compared with the M and $M_{\rm hf}$ amplitudes as well as calculate the size of the $E2$-M and $E2$-$M_{\rm hf}$ interference terms. Tables B.1 and B.2 show the relevant calculations if we assume the population in the $|6SF\rangle$ state is uniform across the m_F sublevels. In that case, the interference terms between the $M1$ amplitudes and the $E2$ amplitude cancel and the pure $E2$ rate is tiny. Therefore, with uniform populations, the contributions from the $E2$ amplitude can be ignored.

The population across the hyperfine sublevels is not uniform, however, as we discussed in Chapter 5. Tables B.3 and B.4 show the effect of the nonuniform population distribution calculated by Peter Marte. (See Chapter 5.) In this case, the R^+ we measure is 0.084% too large, and R^- is 0.068% too small. If we are conservative and assume a 50% uncertainty in the $E2$ correction because of uncertainties in the size of $E2$ and the exact distribution of the population, then the correction makes our result for $|\,M_{\rm hf}/\beta\,|$ smaller by 0.2% and increases our uncertainty from 0.15% to 0.16%.

These results can also be confirmed by rewriting the basis states $|\,Fm_F\rangle$ in terms of the electron and nucleus spin quantum numbers and Clebsch-Gordan coefficients using

$$|\,Fm_F\rangle = \sum_{m_S m_I} |\,Sm_S Im_I\rangle\langle Sm_S Im_I\,|\,Fm_F\rangle. \tag{B.20}$$

Using that formalism gives identical results.

Table B.1: Table showing coefficients for $F = 3$ to $F' = 4$ magnetic dipole and electric quadrupole amplitudes for various transitions. The transition rates in the table are the contributions to the total transition rate relative to the M amplitude assuming uniform populations in the hyperfine levels, $E2/M_{\rm hf} = 0.053$, and $M_{\rm hf}/M = -0.1906$. The sum of all the hyperfine transitions is shown at the bottom and the fractional correction needed to account for the presence of $E2$ is shown in the "Correction" row.

$F = 3$ to $F' = 4$ Uniform Population							
		Coefficients			Transition Rates ($\times 100/M^2$)		
m_F	m'_F	$C^{F'm'_F}_{Fm_F}$	$E2$	Pop	$2ME2$	$2M_{\rm hf}E2$	$(E2)^2$
3	4	0.93541	−0.70151	0.1429	−0.1486	0.0280	0.0004
3	2	0.17678	−0.39772	0.1429	0.0159	−0.0030	0.0001
2	3	0.81009	−0.20251	0.1429	−0.0371	0.0070	0.0000
2	1	0.30619	−0.53578	0.1429	0.0371	−0.0070	0.0003
1	2	0.68465	0.17115	0.1429	0.0265	−0.0050	0.0000
1	0	0.43301	−0.54122	0.1429	0.0531	−0.0100	0.0003
0	1	0.55902	0.41923	0.1429	0.0531	−0.0100	0.0002
0	−1	0.55902	−0.41923	0.1429	0.0531	−0.0100	0.0002
−1	0	0.43301	0.54122	0.1429	0.0531	−0.0100	0.0003
−1	−2	0.68465	−0.17115	0.1429	0.0265	−0.0050	0.0000
−2	−1	0.30619	0.53578	0.1429	0.0371	−0.0070	0.0003
−2	−3	0.81009	0.20251	0.1429	−0.0371	0.0070	0.0000
−3	−2	0.17678	0.39772	0.1429	0.0159	−0.0030	0.0001
−3	−4	0.93541	0.70151	0.1429	−0.1486	0.0280	0.0004
Sum($\times 100$)					0	0	0.0027
Correction to R^+					−0.002%		

Table B.2: Table showing coefficients for $F = 4$ to $F' = 3$ magnetic dipole and electric quadrupole amplitudes for various hyperfine transitions. The transition rates in the table are the contributions to the total transition rate relative to the M amplitude assuming uniform populations in the hyperfine levels, $E2/M_{\rm hf} = 0.053$, and $M_{\rm hf}/M = -0.1906$. The sum of all the hyperfine transitions is shown at the bottom and the fractional correction needed to account for the presence of $E2$ is shown in the "Correction" row.

$F = 4$ to $F' = 3$ Uniform Population							
		Coefficients			Transition Rates ($\times 100/M^2$)		
m_F	m'_F	$C_{Fm_F}^{F'm'_F}$	$E2$	Pop	$2ME2$	$2M_{\rm hf}E2$	$(E2)^2$
4	3	0.93541	0.70151	0.1111	−0.1155	−0.0218	0.0003
3	2	0.81009	0.20251	0.1111	−0.0289	−0.0054	0.0000
2	3	0.17678	0.39772	0.1111	0.0124	0.0023	0.0001
2	1	0.68465	−0.17115	0.1111	0.0206	0.0039	0.0000
1	2	0.30619	0.53578	0.1111	0.0289	0.0054	0.0002
1	0	0.55902	−0.41923	0.1111	0.0412	0.0078	0.0001
0	1	0.43301	0.54122	0.1111	0.0412	0.0078	0.0002
0	−1	0.43301	−0.54122	0.1111	0.0412	0.0078	0.0002
−1	0	0.55902	0.41923	0.1111	0.0412	0.0078	0.0001
−1	−2	0.30619	−0.53578	0.1111	0.0289	0.0054	0.0002
−2	−1	0.68465	0.17115	0.1111	0.0206	0.0039	0.0000
−2	−3	0.17678	−0.39772	0.1111	0.0124	0.0023	0.0001
−3	−2	0.81009	−0.20251	0.1111	−0.0289	−0.0054	0.0000
−4	−3	0.93541	−0.70151	0.1111	−0.1155	−0.0218	0.0003
Sum($\times 100$)					0	0	0.0021
Correction to R^-					0.002%		

Table B.3: Table showing coefficients for $F = 3$ to $F' = 4$ magnetic dipole and electric quadrupole amplitudes for various transitions. The transition rates in the table are the contributions to the total transition rate relative to the M amplitude assuming nonuniform populations in the hyperfine levels, $E2/M_{\rm hf} = 0.053$, and $M_{\rm hf}/M = -0.1906$. The sum of all the hyperfine transitions is shown at the bottom and the fractional correction needed to account for the presence of $E2$ is shown in the "Correction" row.

$F = 3$ to $F' = 4$ Nonuniform Population							
		Coefficients			Transition Rates ($\times 100/M^2$)		
m_F	m'_F	$C_{Fm_F}^{F'm'_F}$	$E2$	Pop	$2ME2$	$2M_{\rm hf}E2$	$(E2)^2$
3	4	0.93541	−0.70151	0.1163	−0.1548	0.0295	0.0006
3	2	0.17678	−0.39772	0.1163	0.0166	−0.0032	0.0002
2	3	0.81009	−0.20251	0.1442	−0.0480	0.0091	0.0001
2	1	0.30619	−0.53578	0.1442	0.0480	−0.0091	0.0004
1	2	0.68465	0.17115	0.1632	0.0388	−0.0074	0.0000
1	0	0.43301	−0.54122	0.1632	0.0776	−0.0148	0.0005
0	1	0.55902	0.41923	0.1666	0.0792	−0.0151	0.0003
0	−1	0.55902	−0.41923	0.1666	0.0792	−0.0151	0.0003
−1	0	0.43301	0.54122	0.1593	0.0757	−0.0144	0.0005
−1	−2	0.68465	−0.17115	0.1593	0.0379	−0.0072	0.0000
−2	−1	0.30619	0.53578	0.1369	0.0455	−0.0087	0.0004
−2	−3	0.81009	0.20251	0.1369	−0.0455	0.0087	0.0001
−3	−2	0.17678	0.39772	0.1134	0.0162	−0.0031	0.0002
−3	−4	0.93541	0.70151	0.1134	−0.1509	0.0288	0.0006
Sum($\times 100$)					0.1150	−0.0220	0.0042
Correction to R^+					−0.094%		

Table B.4: Table showing coefficients for $F = 4$ to $F' = 3$ magnetic dipole and electric quadrupole amplitudes for various hyperfine transitions. The transition rates in the table are the contributions to the total transition rate relative to the M amplitude assuming uniform populations in the hyperfine levels, $E2/M_{\rm hf} = 0.053$, and $M_{\rm hf}/M = -0.1906$. The sum of all the hyperfine transitions is shown at the bottom and the fractional correction needed to account for the presence of $E2$ is shown in the "Correction" row.

$F = 3$ to $F' = 4$ Nonuniform Population							
		Coefficients			Transition Rates ($\times 100/M^2$)		
m_F	m'_F	$C_{Fm_F}^{F'm'_F}$	$E2$	Pop	$2ME2$	$2M_{\rm hf}E2$	$(E2)^2$
4	3	0.93541	0.70151	0.123	−0.1637	−0.0312	0.0006
3	2	0.81009	0.20251	0.1061	−0.0353	−0.0067	0.0000
2	3	0.17678	0.39772	0.1038	0.0148	0.0028	0.0002
2	1	0.68465	−0.17115	0.1038	0.0247	0.0047	0.0000
1	2	0.30619	0.53578	0.104	0.0346	0.0066	0.0003
1	0	0.55902	−0.41923	0.104	0.0494	0.0094	0.0002
0	1	0.43301	0.54122	0.1109	0.0527	0.0100	0.0003
0	−1	0.43301	−0.54122	0.1109	0.0527	0.0100	0.0003
−1	0	0.55902	0.41923	0.1028	0.0489	0.0093	0.0002
−1	−2	0.30619	−0.53578	0.1028	0.0342	0.0065	0.0003
−2	−1	0.68465	0.17115	0.1068	0.0254	0.0048	0.0000
−2	−3	0.17678	−0.39772	0.1068	0.0152	0.0029	0.0002
−3	−2	0.81009	−0.20251	0.1104	−0.0367	−0.0070	0.0000
−4	−3	0.93541	−0.70151	0.1321	−0.1758	−0.0335	0.0007
Sum($\times 100$)					−0.0589	−0.0112	0.0034
Correction to R^-					0.079%		

APPENDIX C

DERIVATION OF INTRACAVITY INTENSITY WITH SIDEBANDS

This appendix derives the intensity inside a Fabry-Perot etalon when the incident light is phase modulated at the free spectral range of the etalon. This intensity is given in Eq. (7.2).

An electric field of the form

$$\epsilon = A\cos(\omega t - \delta \sin \omega_m t) \tag{C.1}$$

can be written in terms of Bessel functions as [74]

$$\begin{aligned} \epsilon = A[J_0(\delta)\cos\omega t &+ 2J_1(\delta)\sin\omega t \sin\omega_m t \\ &+ 2J_2(\delta)\cos\omega t \cos 2\omega_m t + \ldots] \end{aligned} \tag{C.2}$$

where the series extends including higher order Bessel functions and higher multiples of ω_m, and δ is the phase modulation index. If the field is part of an electromagnetic wave, it must have spatial dependence as well. If we replace ωt with $\omega t - ky$ and replace $\omega_m t$ with $\omega_m t - k_m y$, and use the identities

$$\cos\theta\cos\phi = \frac{1}{2}[\cos(\theta-\phi) + \cos(\theta+\phi)] \tag{C.3}$$

$$\sin\theta\sin\phi = \frac{1}{2}[\cos(\theta-\phi) - \cos(\theta+\phi)] \tag{C.4}$$

we get a wave traveling in the $\hat{y}$ direction with the form

$$\begin{aligned}\epsilon = A\{J_0(\delta)\cos(\omega t - ky) &+ J_1(\delta)\left[\cos(\omega_- t - k_- y) - \cos(\omega_+ t - k_+ y)\right] \\ &+ J_2(\delta)\left[\cos(\omega_{--} t - k_{--} y) + \cos(\omega_{++} t - k_{++} y)\right]\}\end{aligned} \tag{C.5}$$

where $k_\pm = k \pm k_m$ and $\omega_\pm = \omega \pm \omega_m$. If this wave is injected into a stable Fabry-Perot etalon with a free spectral range of $\nu_{\mathrm{FSR}} = 2\pi\omega_m$, then the standing wave formed inside the etalon is given by

$$\begin{aligned}\epsilon = 2A[J_0 \sin\omega t \sin ky &+ J_1\left(\sin\omega_- t \sin k_- y - \sin\omega_+ t \sin k_+ y\right) \\ &+ J_2\left(\sin\omega_{++} \sin k_{++} y + \sin\omega_{--} \sin k_{--} y\right)],\end{aligned} \tag{C.6}$$

where the label δ for the phase modulation index has been dropped. Using the identities $\sin(\theta \pm \phi) = \sin\theta\cos\phi \pm \cos\theta\sin\phi$, the electric field can be written as

$$\begin{aligned}\epsilon &= 2A[J_0 \sin\omega t \sin ky \\ &- 2J_1\left(\cos\omega t \sin\omega_m t \sin ky \cos k_m y + \sin\omega t \cos\omega_m t \cos ky \sin k_m y\right) \\ &+ 2J_2\left(\cos\omega t \sin 2\omega_m t \cos ky \sin 2k_m y + \sin\omega t \cos 2\omega_m t \sin ky \cos 2k_m y\right)].\end{aligned} \tag{C.7}$$

We square the field to find the intensity, and since the atoms do not react to changes in the intensity on time scales near $2\pi/\omega$, or even $2\pi/\omega_m$, we will take the time average of the intensity. Therefore we will drop terms containing odd trigonometric functions or products of orthogonal trigonometric functions. The time averaged intensity inside the cavity is given by

$$\begin{aligned}\langle\epsilon^2\rangle_t = 2A^2\,[\,J_0^2 \sin^2 ky &+ 2J_1^2\left(\sin^2 ky \cos^2 k_m y + \cos^2 ky \sin^2 k_m y\right) \\ &+ 2J_2^2\left(\sin^2 ky \cos^2 2k_m y + \cos^2 ky \sin^2 2k_m y\right)\,].\end{aligned} \tag{C.8}$$

Using the identities $\cos^2\theta = 1 - \sin^2\theta$ and $\cos^2\theta - \sin^2\theta = \cos 2\theta$, and setting

$A = 1/\sqrt{2}$, the time averaged intensity inside the cavity can finally be written as

$$\begin{aligned} \langle \epsilon^2 \rangle_t = \sin^2 ky[J_0^2(\delta) &+ 2J_1^2(\delta)\cos 2k_m y + 2J_2^2(\delta)\cos 4k_m y] \\ &+ 2[J_1^2(\delta)\sin^2 k_m y + J_2^2(\delta)\sin^2 2k_m y]. \end{aligned} \tag{C.9}$$